Nonlinear Dynamics of Transition Waves in Multi-Stable Discrete and Continuous Media

Thesis by
Neel Nadkarni

In Partial Fulfillment of the Requirements for the
degree of
Doctor of Philosophy in Aeronautics

CALIFORNIA INSTITUTE OF TECHNOLOGY
Pasadena, California

2017
Defended December 2, 2016

Neel Nadkarni
ORCID: 0000-0002-4311-2817

Dedicated to my loving parents, Prashant and Devika Nadkarni.

ACKNOWLEDGEMENTS

First, I would like to sincerely thank my advisors and mentors, Prof. Chiara Daraio and Prof. Dennis Kochmann. I had the wonderful opportunity of working in theoretical and computational research in Dennis' group at Caltech, during the academic year, and spending my time performing experiments in Chiara's group at ETH in Switzerland, over the summers. I have been very lucky to have both of them as advisers as they gave me immense intellectual freedom while pursuing my research while providing necessary guidance. Dennis' exceptional teaching and theoretical expertise, as well as Chiara's prowess in experimental research and vibrant enthusiasm will always serve as an inspiration to me. They have both been great role models to me, and have provided constant encouragement throughout the course of my graduate studies. I am very grateful to them for shaping me into a better researcher.

I would also like to convey my gratitude to Prof. Rohan Abeyaratne. He has been a wonderful mentor and collaborating with him has helped me develop my theoretical abilities. His deep knowledge in the physics of phase transitions and continuum mechanics has influenced me immensely in my work. I would also like to thank him for inviting me to the workshop that he was co-organizing, at OIST, in Japan, where I had an opportunity to interact with him over an extended period of time, and learn from him.

I would also like to thank Professors Guruswami Ravichandran and Michael Cross for being on my thesis committee. Professor Ravichandran, thank you for all your guidance. I also wish to express my gratitude to all the professors whose courses I took, during my time at Caltech. I am very grateful for support from the NSF grant No. CMMI-1200319 and the Foster and Coco Stanback Space Innovation Fund that made my graduate life at Caltech possible.

I thank the members of both research groups: Jeff Amelang, Yingrui Chang, Jean-Briac le Graverend, Greg Phlipot, Carlos Portela, Wei-Lin Tan, Ishan Tembhekar, Abbas Tutcuoglo, Vidyasagar, Stan Wojnar, and Alex Zelhofer from the Kochmann group and Paul Anzel, Clara Beck, Patricia Benzoni, Luca Bonanomi, Hayden Burgoyne, Maria Chiara Cavalli, Jinwoong Cha, Vincenzo Constanza, Raffaele Di Giacomo, Andre Foehr, Marc Serra Garcia, Francesca Grilli, Sebastian Kroedel, Wei-Hsun Lin, Katie Matlack, Miguel Moleron, Antonio Palermo, Tom Reuter,

Ramathasan Thevamaran, Mythili Thevamaran, Matthieu Ulrici and Chenzhang Zhou from the Daraio group. Thanks a lot Alex, for all the engaging discussions about life that we had during our Tuesday dinners. Vidya, I had an awesome time sharing an office with you in the last year. Thank you Tom, for accommodating me during my first visit to ETH – I had a great time discussing about European and Indian culture and traditions. Andre, dinners at Jimmy's complemented with your dry humor will be missed. Thank you for the wonderful trip to Venice, Deva and Mythili – the experience was made a lot richer by your company. Thank you Katie, Miguel, and Marc for organizing hikes in the beautiful terrains of Switzerland. Thank you Maria Chiara, Paul, Jinwoong, Antonio, and Luca for being awesome office-mates during my time at ETH. I would also like to thank my GALCIT friends from first year, Remi Carmigniani, Melanie Delapierre, Heather Duckworth, Altemurcan Kursunlu, Carlos Laguna, Simon Lapointe, Chris Roh, Kevin Rosenberg, Greg Smetana, Sean Symon, and Stevan van Heerden. The first year experience was a lot more enjoyable because of your presence. Chris, I will cherish all our interesting conversations over dinner – your passion for research in entomology is inspiring. Kevin, Sean, and Simon, I thoroughly enjoyed our Euro-trip! Stevan, our deep discussions over Skype, that lasted for hours, have been an absolute pleasure. Thank you Denise Ruiz, Dominique Lorandt, and Jamie Meghan-Sei for all the administrative assistance during conferences and travel.

I want extend a special thanks to Kishore Jaganathan, Pushkar Kopparla, and Sisir Yalamanchili who made my time at Caltech very memorable. Kishore, I will always remember our hard-fought tennis games and I also blame you for encouraging my terrible sense of humor. Pushkar, thanks for introducing us to Mil who has been responsible for getting us tables at every restaurant we go to. Sisir, it has been an amazing two years being your house-mate and your dosa batter-making skills shall be missed. Anupama Lakshamanan, Siddharth Jain, Srikanth Tenneti, Prachi Parihar, and Sumanth Dathathri, thank you for all the fun times we had. I would like to thank my undergrad mates, Aditi Dighe, Ajinkya Kulkarni, Yogesh Goyal, and NC Puneeth who have been amazing friends throughout.

Badminton and cricket have been an integral part of my life during my time at Caltech. I wish to thank the Caltech Badminton Club players, Phong Nguyen, Remi Mevel, Yi Cao, Chen Chang, Shi-En Kim, Di Wu, Sophia Dai, Chujun Lin, Manish V., Vipul Singhal, and all other group members. I also thank the Caltech Cricket Club members, Charles Steinhardt, David Hall, Siddharth Jain, Sumanth Dathathri,

Kishore Jaganathan, Anantha Ravi Kiran, Sisir Yalamanchili, Vibhor Kumar, Rahul Soni and all the others who have been a part of the club.

I would also like to express my sincere gratitude to Parul Gupta. Thank you for serendipitously coming into my life. You have been a pillar of support – thank you for being there.

Finally, I would like to thank my wonderful parents, Devika and Prashant Nadkarni. I owe everything I have achieved to you. Nothing would have been possible without your support and love. I dedicate this thesis to you.

ABSTRACT

The concept of phase transitions, i.e., switching between two or more different equilibrium states of a system, is commonly encountered in many physical, chemical and biological phenomena. The exact mechanism of this switching is a highly nonlinear dynamical process that is accommodated by the propagation of a localized wave. The characteristics of the nonlinear wave such as its profile, velocity, energy, and width of transition are governed by the type and specifics of the system that it is propagating through which may be conservative, dissipative, or diffusive in nature. The goal of this thesis is to develop a fundamental understanding of the dynamics of such processes in general nonlinear systems capable of undergoing phase transitions and the application of new theories to elucidate the kinetic and energetic properties of transition waves in different scenarios. In conservative systems, we show that there are three different modes of stable wave propagation that we analytically solve for and validate computationally. In contrast, dissipative and diffusive systems allow the stable propagation of only the strongly nonlinear kink mode whose kinetic energy and propagation velocity are linked through a linear relation. We further validate our results in dissipative systems experimentally by fabricating and testing a strongly nonlinear lattice and show that transition waves are unidirectional in nature, as predicted by theory. Finally, as an application, we devise a strategy of using the physics of dissipative phase transitions to propagate stable mechanical signals in highly dissipative media such as soft polymers which effectively damp out small-amplitude linear waves.

PUBLISHED CONTENT AND CONTRIBUTIONS

[1] Neel Nadkarni, Andres F. Arrieta, Christopher Chong, Dennis M. Kochmann, and Chiara Daraio. "Unidirectional Transition Waves in Bistable Lattices". In: *Physical Review Letters* 116.24 (June 2016), p. 244501. DOI: 10.1103/PhysRevLett.116.244501. URL: http://link.aps.org/doi/10.1103/PhysRevLett.116.244501.
N.N. built the experimental setup, performed the theoretical analysis and numerical simulations.

[2] Neel Nadkarni, Chiara Daraio, Rohan Abeyaratne, and Dennis M. Kochmann. "Universal energy transport law for dissipative and diffusive phase transitions". In: *Physical Review B* 93.10 (Mar. 2016), p. 104109. DOI: 10.1103/PhysRevB.93.104109. URL: http://link.aps.org/doi/10.1103/PhysRevB.93.104109.
N.N. performed the theoretical analysis and the numerical simulations.

[3] Neel Nadkarni, Chiara Daraio, and Dennis M. Kochmann. "Dynamics of periodic mechanical structures containing bistable elastic elements: From elastic to solitary wave propagation". In: *Physical Review E* 90.2 (Aug. 2014), p. 023204. DOI: 10.1103/PhysRevE.90.023204. URL: http://link.aps.org/doi/10.1103/PhysRevE.90.023204.
N.N. performed the theoretical analysis and numerical simulations.

[4] Jordan R. Raney, Neel Nadkarni, Chiara Daraio, Dennis M. Kochmann, Jennifer A. Lewis, and Katia Bertoldi. "Stable propagation of mechanical signals in soft media using stored elastic energy". en. In: *Proceedings of the National Academy of Sciences* 113.35 (Aug. 2016), pp. 9722–9727. ISSN: 0027-8424, 1091-6490. DOI: 10.1073/pnas.1604838113. URL: http://www.pnas.org/content/113/35/9722.
N.N. performed the theoretical analysis and numerical simulations.

TABLE OF CONTENTS

LIST OF ILLUSTRATIONS

LIST OF TABLES

Chapter 1

INTRODUCTION

The goal of this thesis is to understand the physics of nonlinear wave propagation in systems that exhibit multiple states or 'phases' of equilibrium. The switching between two stable equilibria gives rise to a nonlinear wave called a transition wave and the phenomenon is called a phase transition. This thesis explores the theory behind these phase transitions in conservative, dissipative and diffusive systems. Further, we investigate how the theory can be used to design and experimentally realize nonlinear mechanical systems having structural phase transitions. We also discuss the application of the theory to current models of microstructure evolution in ferroelectric ceramics and suggest further steps to improve the model. This chapter introduces the concept of phase transitions and their mechanism in various systems.

1.1 Motivation

A phase transition can be illustrated by a simple example in mechanics. Consider a pendulum with a mass, hanging from a rigid support. Assuming the bar of the pendulum is mass-less, the potential energy of the hanging mass as a function of the angle of rotation is shown in Fig. 1.1. The energy has a multi-stable landscape having an equilibrium for every 2π rotation. An infinite lattice of such pendulums can be built by connecting them through a linear torsional springs. A schematic of

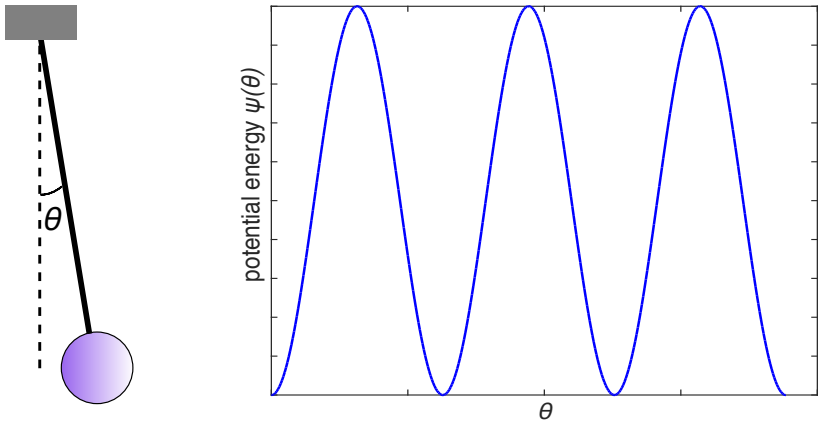

Figure 1.1: Pendulum hung from a support with its potential energy as a function of angular rotation.

this lattice is shown in Fig. 1.2. The governing equation for the motion of the n^{th} pendulum is given by

$$I\ddot{\theta_n} - C(\theta_{n+1} - 2\theta_n + \theta_{n-1}) + mgl\sin\theta_n = 0, \tag{1.1}$$

where I is the moment of inertia, C is the stiffness of the torsional springs, m is the mass, g is the acceleration due to gravity and l is the length of the pendulum. The rotation of one of the pendulums from one stable state to another (i.e. $\theta = 0 \rightarrow 2\pi$) causes a traveling wave to propagate through the system that switches each consecutive pendulum from $\theta = 0$ phase to the $\theta = 2\pi$ phase in a sequential manner. This mechanical system was designed by Scott [130], as a simple model of the nonlinear Klein-Gordon equation, where he analyzed the nature and stability of the transition wave. Further numerical and experimental investigations were performed to characterize transitions in this system [32, 38, 102]. The presence of the multi-stable potential creates topological wavefronts or kinks that can travel through the medium. Phase transformations due to the propagation of such a kink or transition front are ubiquitous, occurring in varied systems. Following are a few examples where phase transitions are commonly encountered due to the presence of bi/multi-stable potentials in lattices or continua.

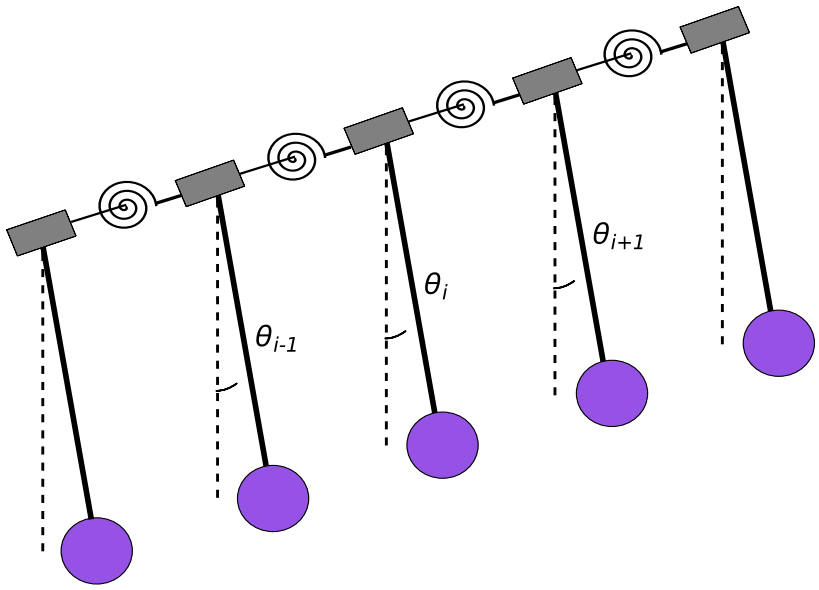

Figure 1.2: Nonlinear lattice of rotating pendulums connected by torsional springs. The pendulums rotate out of the plane creating the transition wave.

1.2 Lattice dynamics in mechanics

Equation (1.1) is the celebrated Frenkel-Kontorova (FK) equation that was first employed to explain dislocation motion in metals [51]. The dynamics of the kink in the model describes the propagation of the dislocation core. In contrary to a continuum, the inherent discreteness of the lattice gives rise to the Peierls-Nabarro (PN) potential that the kink needs to overcome in order to move in the lattice [96, 112]. Such effects of discreteness of the lattice along with acoustic radiation [7], preferential velocity of propagation [114], and kink dressing or shape modification [59] have been studied in great detail. For a review of FK lattice models, see [26, 27]. FK-type lattice models have been used to explain other mechanical processes as well. For instance, in structural mechanics, chains of bistable linkages with gaps of zero resistance or a "waiting link structure" have been shown to have increased stability due to the delocalization of damage and conversion of mechanical energy to heat through high-frequency background oscillations [31, 139]. Such periodic chains with bistable linkages or non-monotonic stress-strain relationships have been successfully employed as models to explain structural transitions, fracture, and damage [9, 10, 69, 138, 150, 154]. The mechanical response of carbon nanotubes [20, 48] have also been explained on the basis of buckling or snapping instabilities arising from systems with multiple stable configurations described by lattice models. Stochastics coupled with multi-stable on-site potentials in the Langevin framework have been used to develop models for surface friction [158, 159]. Therefore, FK lattice models have been utilized to explain mechanical processes from the small scale like surface friction to large-scale structural mechanics.

1.3 Thermoelastic materials

A thermoelastic material changes its structural phase due to the presence of thermal or elastic stresses in the material. An example of a thermoelastic phase transformation is between austenite and martensite. The austenite phase has a body-centered cubic structure whereas the martensite phase has a tetragonal structure. Due to the non-centrosymmetry of the martensitic crystal structure, the martensitic phase can have different variants. It has been shown that the martensitic phase, due to geometric compatibility, must generate a combination of variants in its microstructure, in order to minimize its energy [11], whereas the austenite phase is homogeneous, as seen in Fig. 1.3. The phase transformation between austenite to martensite can be modeled as a switch between two stable points of the multi-stable Gibbs free energy well, giving rise to a non-monotonic stress-strain curve. This problem of a

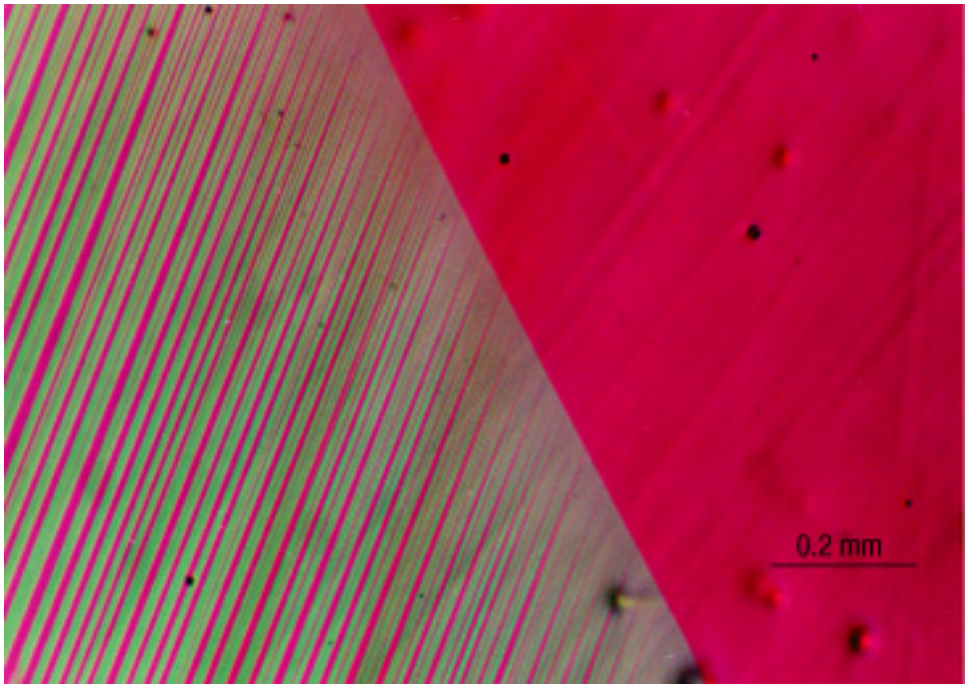

Figure 1.3: Microstructure of the twinned martensite phase next to a homogeneous austenite phase in a Cu-Ni-Al alloy (adapted from [34])

thermoelastic solid undergoing a phase transition in a one-dimensional setting has been extensively studied [2, 3, 5]. A key result from these papers is the entropy inequality for phase transformations,

$$f(t)\dot{s}(t) \geq 0, \tag{1.2}$$

where $f(t)$ is the driving traction which is an Eshelby-like traction acting on the surface of the discontinuity separating the two phases [41], and $\dot{s}$ is the velocity of the phase boundary. The driving traction $f = 0$ signifies phase equilibrium within the solid. The kinetic relation that relates the driving traction to the motion of the phase boundary is an essential component in uniquely determining the quasi-static and dynamic response of the material [4]. The concept of driving traction has been extended further to higher dimensions where it is the force acting in the direction normal to the surface of phase discontinuity [1]. Controlling the driving traction and thereby the phase boundary motion plays an important role in phase transition, a process that has been put to practice in many applications. A commonly encountered thermoelastic solid is a shape memory alloy. Shape memory alloys “remember" their high-temperature-phase shape as they switch from the low-temperature phase to the high-temperature phase through a diffusionless transition. This effect has been used

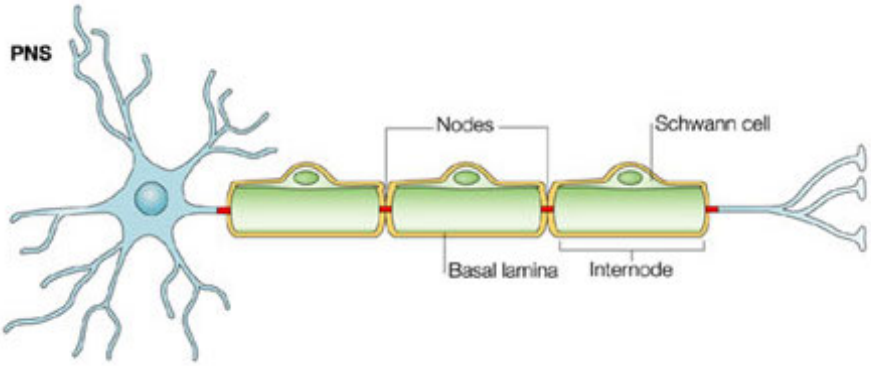

Figure 1.4: Axon in the peripheral nervous system covered with a myelin sheath made up of Schwann cells. There are periodic gaps in the sheaths called the Nodes of Ranvier. The electrical signal passes through due to the potential difference between the Nodes of Ranvier (courtesy [115])

.

for many applications such as vibration damping in aircrafts [54], control of civil structures [141] and dental braces in medicine [86].

1.4 Action potential propagation through myelinated axons

Transition waves in the form of propagation of electrical signals also occur in biological systems. One such example is the propagation of action potentials along the axon of a nerve cell. An axon is a transmission line that communicates between two neurons. A diagram of an axon in the peripheral nervous system is shown in Fig. 1.4. For efficient communication, the axon is covered by myelin sheaths composed of glial cells called Schwann cells in the peripheral nervous system and oligodendrocytes in the central nervous system [115]. The presence of the myelin sheaths increases the effective resistance of the membrane from $10^3\Omega$ cm^2 to $10^5\Omega$ cm^2 and reduces the capacitance from 10^{-6} μF/cm^2 to 10^{-8} μF/cm^2, causing fast signal propagation [65]. The sheaths are separated by periodic gaps called Nodes of Ranvier. The electrical signal jumps from one node to another in the form of a transition wave that is given by the equation,

$$\frac{dV_n}{dt} = D(V_{n+1} - 2V_n + V_n) + f(V_n), \tag{1.3}$$

where V_n is the nodal potential, D is the coupling constant, and $f(V)$ derives from an asymmetric bistable potential. Equation (1.3) is a reaction-diffusion equation that shows propagation failure below a critical coupling constant due to discreteness effects [64]. The first experiment on the propagation of action potentials along these

nerve fibers was performed by Hodgkin and Huxley on the nerve [55]. Another model to simulate the motion of the transition wave was proposed by Fitzhugh, which was later realized experimentally through an electrical circuit by Nagumo et. al. [45, 100]. For a general discussion of electrophysics of nerve fibers, see [65, 115, 131].

1.5 Josephson junctions

The Josephson junction that shows current tunneling through an electric insulator was proposed by Brian Josephson as part of his PhD work for which he was awarded the Nobel Prize in Physics in 1973 [62]. A schematic of a Josephson junction is shown in Fig. 1.5.

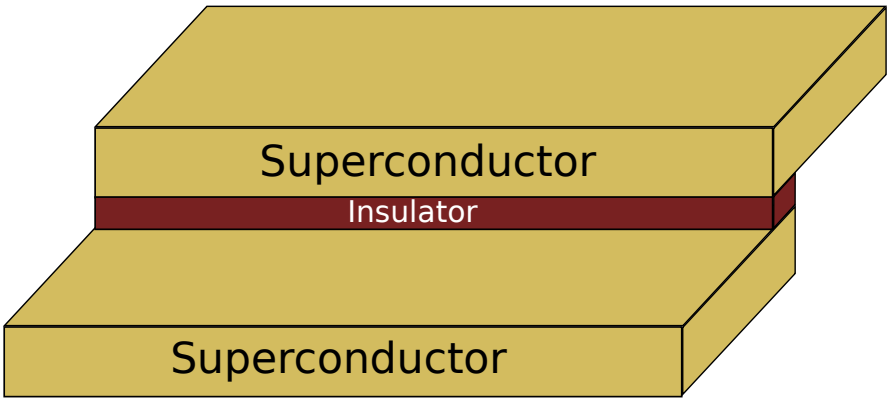

Figure 1.5: A Josephson junction

The Josephson junction consists of an insulator sandwiched by two superconducting electrodes. The superconductor has pairs of bound electrons with two spins of $\pm 1/2$ called Cooper pairs which have an electromagnetic quantum phase associated with them. For a short Josephson junction, if the phase difference between the Cooper pair phases of the two superconductors is ϕ, then the equation governing the phase difference is of that of a damped oscillatory pendulum, written as

$$\frac{d^2\phi}{dt^2} + \frac{1}{RC}\frac{d\phi}{dt} + \omega_0^2 \sin\phi = J_B, \tag{1.4}$$

where R is the resistance, C is the capacitance, ω_0 is a characteristic frequency proportional to the critical current density and thickness of the insulating layer, and J_B is a constant proportional to the bias current provided by a generator [148]. If an array of such Josephson junctions is connected together in a lattice with spacing

a, then the governing equation is that of a damped oscillatory pendulum chain presented in section 1.1, given by

$$\frac{d^2\phi_n}{dt^2} + \alpha\frac{d\phi_n}{dt} - \frac{1}{a^2}(\phi_{n+1} + \phi_{n-1} - 2\phi_n) + \sin\phi_n - \gamma = 0, \tag{1.5}$$

where ϕ_n is the phase difference between the n^{th} superconducting pair [152, 153]. The phase difference transitions in the form of a discrete traveling wave propagating through the lattice. This wave is called discrete fluxon. In long or extended Josephson junctions, the discrete wave equation is converted to a continuous equation of the form,

$$\frac{\partial^2\phi}{\partial t^2} + \alpha\frac{\partial\phi}{\partial t} - c_0^2\frac{\partial^2\phi}{\partial x^2} + \sin\phi - \gamma = 0. \tag{1.6}$$

Multiple fluxons can be created in this system that behave as independent quasi-particles [35]. The physics of Josephson junctions has been used to create many devices such as superconducting quantum interference devices (SQUIDs) [60, 87].

1.6 Bistable chemical reactions

Nonlinear localized transition waves in the form of solitons also occur in reaction-diffusion equations. The oxidation of carbon monoxide on a platinum catalyst is a prime example of such a reaction mechanism. The 2007 Nobel Prize in Chemistry was awarded to Gerhard Ertl for discovering this surface science phenomenon. A photoemission electron microscope image shown in Fig. 1.6 describes the presence of solitary wavefronts during the oxidation reaction. The localized waves of oxygen concentration move at a constant velocity of around 3μm/s. The merging of two waves leads to an annihilation or they move past each other while preserving their shape, which is a typical characteristic of solitary waves [13]. The reaction mechanism for such a system can be explained by the equation

$$\frac{\partial \boldsymbol{u}}{\partial t} = D\frac{\partial^2 \boldsymbol{u}}{\partial x^2} + \boldsymbol{f}(\boldsymbol{u}), \tag{1.7}$$

where $\boldsymbol{u}$ are the chemical variables associated with concentrations, and D is a matrix of all transport coefficients with $\boldsymbol{f}$ containing driving forces from bistable potentials [13, 124, 145]. Another example of transition fronts in chemical mechanisms is a chain of coupled bistable chemical reactors. In this system, each stirred tank reactor undergoes a bistable chlorite-iodide reaction and the reaction propagates from one chemical reactor to another through mass exchange. The equation of chemical concentration evolution is equivalent to a neural pulse propagation in axons as described in Sec. 1.4. An experimental system was realized with 16 coupled bistable

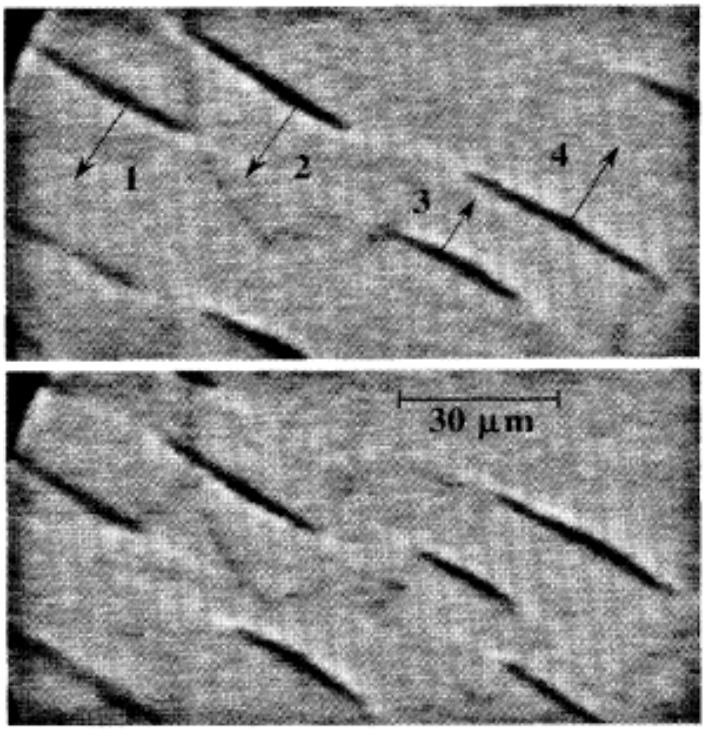

Figure 1.6: A photoemission electron microscope image showing the oxidation of CO on a Pt substrate. The dark regions is where the oxygen adsorbate is concentrated that move as localized waves with a constant velocity (adapted from [13]).

reactors arranged in a ring [22]. The system shows propagation failure below a certain critical coupling constant very similar to the propagation failure in a nerve fiber [73].

Therefore, phase transitions due to the propagation of strongly nonlinear transition waves occur in many physical, chemical, and biological bistable systems as a result of inter-well switching. This thesis explores this phenomenon to characterize this wave propagation that occurs in these different systems.

1.7 Outline

Chapter 2 examines the intra-well dynamics and inter-well phase transitions of a conservative mechanical lattice with on-site bistable wells, in the long-wavelength limit. Previous research on such systems focused on the linear regime or the strongly nonlinear switching regime. Our analysis indicates the presence of an intermediate envelope solitary wave mode due to weakly nonlinear intra-well motion. We also present closed-form solutions for the family of linear, weakly nonlinear and strongly nonlinear wave modes. In the case of asymmetric potentials caused due to local pre-

compression applied to each node of the lattice, we show that the wave propagation is a combination of the strongly nonlinear kink shaped wave mode and the weakly nonlinear envelope solitary wave mode. This chapter provides a direction towards the creation of nonlinear metamaterials.

Chapter 3 analyzes inter-well phase transitions in a lattice and continuum when the mechanism is diffusive or dissipative in nature in general bi/multi-stable lattices and continua. Unlike the conservative case where there is a family of kink solutions, we observe that there is at most one steady-state waveform and velocity. The average energy of the wave is linearly related to its velocity through a universal principle. The ratio of the average energy to velocity is independent of the bistable topology, number of neighborhood interactions, and form of the interaction potential. We also show that this energy scaling applies to a multi-stable switching as well. We confirm our theory with multiple numerical examples.

Chapter 4 delineates a design of a fully nonlinear discrete dissipative system with on-site bistable nonlinearities and interaction nonlinearities. The system allows the propagation of strongly nonlinear transition waves. We show that, in such a system, in spite of discreteness effects and highly nonlinear interactions, the average energy per momentum density transported by the transition wave remains a constant and can be determined by the energy law derived in the previous chapter. Due to the asymmetry in the energy wells, the wave propagation is unidirectional in nature, so that the transition occurs only from the high-energy state to the low-energy state.

Chapter 5 describes a structural application of the theory to build soft mechanical metamaterials that counteract dissipation with structural instabilities. We present a lattice made of a polymeric material that propagates transition waves while linear waves are damped out by the intrinsic dissipation. The structural properties can be readily tuned by applying pre-compression to the lattice to propagate the waves faster or slower. The properties of the lattice can be spatially altered to give rise to accelerating and decelerating waves. A design to realize soft mechanical logic such as diodes, AND, and OR gates is also described. This chapter presents a blueprint for novel metamaterial applications in the nonlinear regime of wave propagation.

Chapter 6 concludes the thesis and provides an outlook toward future research directions. A special section is devoted to the dynamics of domain wall motion in ferroelectric ceramics. We show how the energy transport law derived in Chapter 3 can be used to relate the velocity of the domain wall to the applied electric field through the Eshelby driving traction acting on the domain wall. The current models

do not provide the correct scaling of the domain wall velocity with the applied electric field. We further outline techniques to improve the current models to capture the correct domain wall kinetics.

Chapter 2

NONLINEAR DYNAMICS OF A CONSERVATIVE LATTICE WITH ON-SITE BISTABLE POTENTIALS

Research presented in this chapter has been adapted from the following publication:

Neel Nadkarni, Chiara Daraio, and Dennis M. Kochmann. "Dynamics of periodic mechanical structures containing bistable elastic elements: From elastic to solitary wave propagation". In: *Physical Review E* 90.2 (Aug. 2014), p. 023204. DOI: 10.1103/PhysRevE.90.023204. URL: http://link.aps.org/doi/10.1103/PhysRevE.90.023204.

In this chapter, we analyze the problem of phase transitions and intra-well dynamics in a conservative system that permits two stable states at each node through a bistable on-site potential. In particular, we investigate the nonlinear dynamics of a periodic chain of bistable elements consisting of masses connected by elastic springs whose constrained arrangement gives rise to a large-deformation snap-through instability. We show that the resulting negative-stiffness effect produces three different regimes of (linear and nonlinear) wave propagation in the periodic medium, depending on the wave amplitude. At small amplitudes, linear elastic waves experience dispersion that is controllable by the geometry and by the level of precompression. At moderate to large amplitudes, solitary waves arise in the weakly and strongly nonlinear regime. For each case, we present closed-form analytical solutions and we confirm our theoretical findings by specific numerical examples. The precompression reveals a class of wave propagation for a partially positive and negative potential. The presented results highlight opportunities in the design of mechanical metamaterials based on negative-stiffness elements, which go beyond current concepts primarily based on linear elastic wave propagation. Our findings shed light on the rich effective dynamics achievable by nonlinear small-scale instabilities in solids and structures.

2.1 Introduction

The periodic arrangement of small-scale building blocks results in acoustic or mechanical metamaterials [12] which have attracted great attention because of their extremely rich field of applications including acoustic wave guides and filters [108,

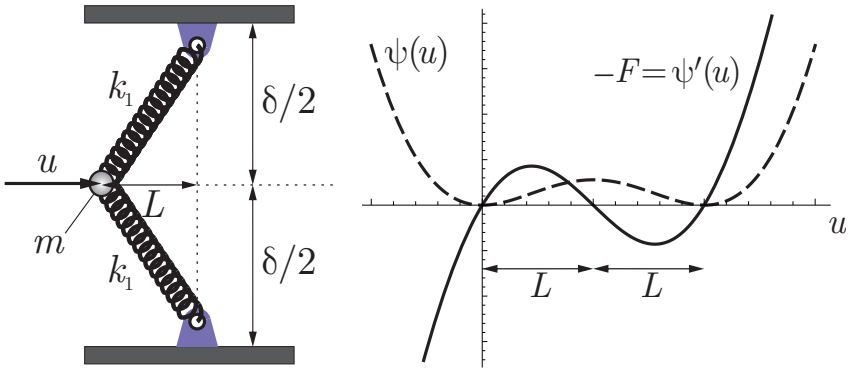

Figure 2.1: Bistable element consisting of two elastic springs and a point mass, energy $\psi(u)$, and force $F(u)$.

162], acoustic lenses and diodes [17, 142], sound isolators and sensors [118, 172], and acoustic cloaks and sonar stealth technologies [92, 94]. Design strategies commonly exploit the scattering of elastic waves in periodic media at characteristic frequencies in all or specific directions [72, 125, 137] as well as resonant phenomena capable of absorbing energy on lower scales by local resonators [83, 134]. In all these examples, the careful microscale periodic architecture of multiscale engineered material systems leads to an interesting or beneficial effective dynamic behavior on the macroscale. Besides pronounced acoustic band gaps [128, 167], this design paradigm has resulted in negative effective dynamic stiffness [42] and mass density [84, 166], and combinations of both [37]. Here, negative stiffness and negative mass density refer to the effective dynamic properties: An elastic system containing only positive-stiffness elements can demonstrate negative effective dynamic quantities near resonance.

Static negative (incremental) stiffness arises from instabilities in solids and structures when the energy landscape loses (some notion of) convexity. Bistable elements such as the spring configuration schematically shown in Fig. 2.1 make an excellent example: The potential energy's nonconvexity provides the system with an unstable regime of negative energy curvature (i.e. negative incremental stiffness) whose nonlinear force-displacement relation leads to a spontaneous snapping from one stable equilibrium to the next energy minimum if pure tractions are applied. The same phenomenon can be observed in pre-stressed buckled structural members [28]. Although the beneficial effects of negative-stiffness elements on the effective dynamic performance of acoustic or mechanical metamaterials and composites is well known [160], previous research has focused on the linear elastic regime. However, as discussed in Sec. 1.1, bistable or multistable building blocks in periodic

solids and structures also promise interesting nonlinear dynamic effects, including solitary-wave propagation, which provides opportunities to focus acoustic signals in mechanical metamaterials [50, 142]. Homogeneous solids undergoing finite elastic deformation [111] as well as periodic media experiencing nonlinear elastic instabilities [16] have been shown to exhibit acoustic band gaps that are controllable by the amount of nonlinear pre-deformation, yet the investigated waves again operate in the linear elastic regime. To date, only one example of periodic elastic mechanical system (as illustrated in Sec. 1.1) has been reported that produces sine-Gordon solitons by allowing a kink propagation in the form of elastically connected rotating pendulums [32, 38, 102, 127, 130]. The weakly or strongly nonlinear response of elastic media containing negative-stiffness elements such as the bistable spring configuration shown in Fig. 2.1 has remained widely unexplored, in part because such instabilities in solids and the resulting nonlinear effective dynamics are mathematically complex and make analytical solutions a rare find.

Here we study a mechanical system capable of propagating impact pressure waves in three different regimes, serving as a model for the creation of *nonlinear acoustic metamaterials* with static negative-stiffness elements. We present closed-form analytical results for the nonlinear response of a chain of bistable elements consisting of elastic springs and point masses. The specific configuration of the periodically repeated elementary unit cell displays a continuous nonmonotonic force-displacement relation with two stable equilibria and one unstable equilibrium configuration giving rise to temporary negative (static) stiffness. We have deliberately chosen a simple albeit instructive mechanical system that enables us to study the rich dynamics of periodic chains of bistable elements in the full range of its linear to strongly-nonlinear behavior. The chosen spring configuration shows the same features as prebuckled structures (while allowing for a clean analytical investigation) and the conclusions drawn here can qualitatively be transferred to numerous structural instabilities. In fact, the interesting wave propagation characteristics reported here hint at the design of novel mechanical metamaterials with controllable wave propagation in the linear and nonlinear regimes, with applications ranging from wave guides and amplifiers to vibration attenuators. The chosen system admits a clean identification of all model parameters and allows for experimental implementation. We note that in our analysis we assume conservative systems and thereby neglect energy dissipation through internal friction or other damping mechanisms that are usually found in mechanical systems. Of course, the presence of damping will alter the response of the system (our numerical examples contain small amounts of damping to remove

transient effects, whereas all analytical solutions assume energy conservation).

2.2 Bistable chain configuration

Consider the bistable structure consisting of two identical and symmetrically-arranged linear elastic springs with stiffness k_1 as shown schematically in Fig. 2.1 in its unstressed equilibrium configuration. Both springs are connected by a joint allowing for rotation and carrying point mass m. Their free ends are attached to joints which allow for rotation but prevent translation. Due to symmetry, a horizontal force on mass m will result in a horizontal displacement u, so we may treat the system as one-dimensional in the following. The total potential energy stored by the structure is given by

$$\psi(u) = k_1 \left[l(u) - l_0\right]^2, \tag{2.1}$$

where

$$l(u) = \sqrt{(L-u)^2 + \left(\frac{\delta}{2}\right)^2} \tag{2.2}$$

is the deformed length of each spring with geometric details δ and L introduced in Fig 2.1. Consequently, the initial spring length is given by $l_0 = l(0)$. Energy (2.1) is illustrated in Fig 2.1 as a function of the displacement u, which demonstrates two stable equilibria (i.e., local energy minima) and one unstable equilibrium configuration (corresponding to the local energy maximum). The structure experiences negative stiffness as it passes through this unstable regime.

To arrive at a periodic one-dimensional chain, we consider an array of N such bistable elements connected by horizontal linear springs of stiffness k_2 that act as force transfer elements. Identical masses m are placed at each node of the chain, as shown schematically in Fig 2.2. The total Hamiltonian of the spring system can be written as

$$H(\boldsymbol{u}, \boldsymbol{u}_{,t}) = \sum_{i=1}^{N} \left[\frac{m}{2} u_{i,t}^2 + \psi_i(u_i)\right] + \sum_{i=1}^{N-1} \frac{k_2}{2}(u_{i+1} - u_i)^2, \tag{2.3}$$

where $\psi(u_i)$ is the potential energy stored by the ith bistable pair of springs, $\boldsymbol{u} = \{u_1, \ldots, u_N\}$ denotes the vector of all nodal displacements depending on time t, and a comma in indices denotes differentiation with respect to the ensuing variable(s). Therefore, the rate of change of momentum of mass i follows from Hamilton's equation, i.e.

$$p_{i,t} = m\, u_{i,tt} = -\frac{\partial H}{\partial u_i}. \tag{2.4}$$

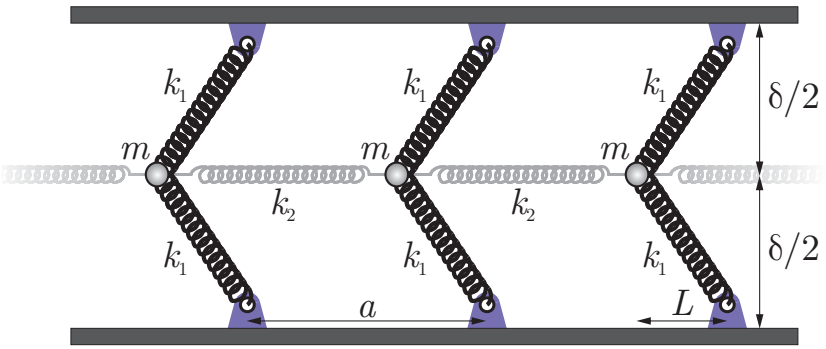

Figure 2.2: Periodic chain of bistable elements.

Application of (2.3) yields

$$m\,u_{i,tt} + k_2(-u_{i+1} + 2u_i - u_{i-1}) - F(u_i) = 0, \tag{2.5}$$

where the internal force applied to mass i by the bistable spring element was introduced as

$$F(u) = -\psi'(u) = -2k_1(L-u)\,\frac{l(u) - l_0}{l(u)}. \tag{2.6}$$

2.3 Scaling and continuum limit

Dimensionless equations will enable us to investigate the mechanics of the system without having to specify geometry and material parameters explicitly. In order to reduce the problem to a self-similar type, we scale the displacements and the nodal spacing with respect to their respective length scales. For a lattice parameter a (initial spacing between two masses), we define

$$\bar{x} = \frac{x}{a} \quad \text{and} \quad \bar{u} = \frac{u}{L}, \tag{2.7}$$

where $\bar{x}$ and $\bar{u}$ are the dimensionless x-coordinate and displacement, respectively. Therefore, the force $F(u)$ can be expressed in dimensionless form as

$$\bar{F}(\bar{u}) = \frac{F(u)}{k_1 L} = 2(1-\bar{u})\left(1 - \frac{\bar{l}_0}{\bar{l}(u)}\right) \tag{2.8}$$

with

$$\bar{l}(\bar{u}) = \sqrt{(1-\bar{u})^2 + d^2}, \quad d = \frac{\delta}{2L}, \quad \bar{l}_0 = \bar{l}(0). \tag{2.9}$$

This suggests that the dimensionless force of the bistable spring element only depends on ratio $d = \delta/2L$ and not on actual lengths. The governing equation (2.5) can be non-dimensionalized by using the same force scale and defining two new dimensionless parameters, viz. the stiffness ratio K_r and the characteristic time scale T

(the period associated with the eigenfrequency of mass m attached to a single spring of stiffness k_1):

$$K_r = \frac{k_2}{k_1} \quad \text{and} \quad T = \sqrt{\frac{m}{k_1}}. \tag{2.10}$$

This gives

$$\bar{u}_{i,\bar{t}\bar{t}} + K_r(-\bar{u}_{i+1} + 2\bar{u}_i - \bar{u}_{i-1}) - \bar{F}(\bar{u}_i) = 0. \tag{2.11}$$

We choose the origin such that mass i is initially located at $x_i = i\,a$, and positions are normalized by defining

$$\bar{x}_i = \frac{x_i}{a} = i \quad \text{so that} \quad \Delta\bar{x} = \bar{x}_i - \bar{x}_{i-1} = 1. \tag{2.12}$$

In the continuum limit ($a \to 0$), $\bar{u}_{i+1}$ and $\bar{u}_{i-1}$ can be written, using a Taylor expansion, as

$$\bar{u}_{i\pm1} = \bar{u}_i \pm \frac{\partial\bar{u}_i}{\partial\bar{x}} + \frac{1}{2}\frac{\partial^2\bar{u}_i}{\partial\bar{x}^2} \pm \frac{1}{6}\frac{\partial^3\bar{u}_i}{\partial\bar{x}^3} + \frac{1}{24}\frac{\partial^4\bar{u}_i}{\partial\bar{x}^4} + h.o.t. \tag{2.13}$$

By substituting (2.13) into (2.11), we obtain the dimensionless continuum limit of the equation of motion,

$$\bar{u}_{,\bar{t}\bar{t}} - K_r\left(\frac{\partial^2\bar{u}}{\partial\bar{x}^2} + \frac{1}{12}\frac{\partial^4\bar{u}}{\partial\bar{x}^4} + h.o.t.\right) - \bar{F}(\bar{u}) = 0. \tag{2.14}$$

2.4 Dispersion relation and long-wavelength approximation

In order to determine the dispersion relation of the periodic chain in the continuum limit, let us first consider the linear regime. Here, the equation of motion can be approximated by linearizing (2.8) about $\bar{u} = 0$, which gives

$$\bar{u}_{,\bar{t}\bar{t}} - K_r\left(\frac{\partial^2\bar{u}}{\partial\bar{x}^2} + \frac{1}{12}\frac{\partial^4\bar{u}}{\partial\bar{x}^4} + h.o.t.\right) + \omega_0^2\bar{u} = 0 \tag{2.15}$$

where

$$\omega_0^2 = \frac{2}{1+d^2}. \tag{2.16}$$

We assume a traveling wave solution of the form

$$\bar{u} = \hat{u}\,e^{i(\bar{q}\bar{x} - \bar{\omega}\bar{t})} \tag{2.17}$$

with $\bar{q} = qa$ and $\bar{\omega} = \omega T$. Substitution of (2.17) into (2.15) yields the continuum dispersion relation

$$\bar{\omega}(\bar{q}) = \sqrt{\omega_0^2 + K_r\left(\bar{q}^2 - \tfrac{1}{12}\,\bar{q}^4 + h.o.t.\right)} \tag{2.18}$$

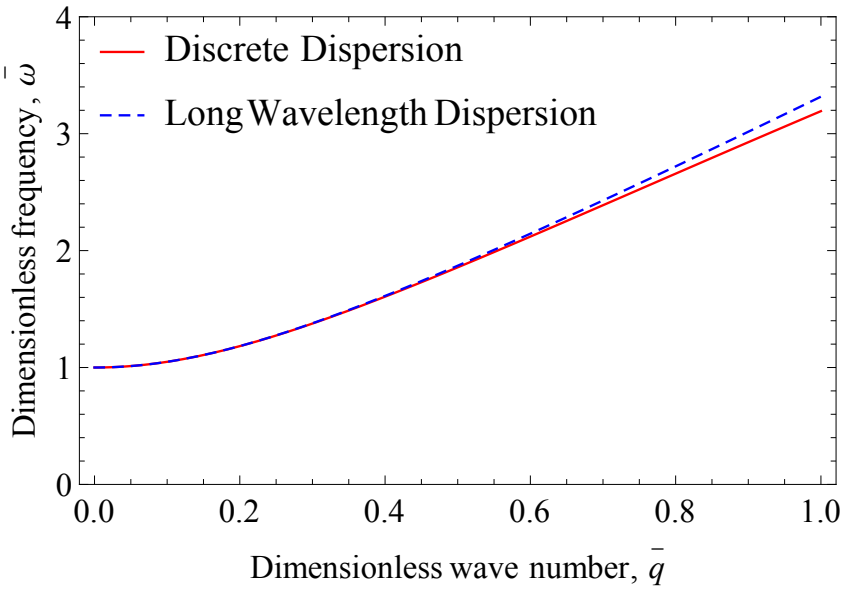

Figure 2.3: Dispersion relation comparison

In the long-wavelength limit $\bar{q} = qa \ll 1$ the dispersion relation can be approximated by only retaining the leading-order quadratic term and dropping all higher-order terms such that (2.18) becomes

$$\bar{\omega}(\bar{q}) \approx \bar{\omega}_c(\bar{q}) = \sqrt{\omega_0^2 + K_r \bar{q}^2}. \tag{2.19}$$

The exact dispersion relation for the discrete system is obtained by substituting the traveling wave form (2.17) into the linearized form of the discrete equation of motion (2.11), which gives

$$\bar{\omega}_d(\bar{q}) = \sqrt{\omega_0^2 + 2K_r\,(1 - \cos\bar{q})}. \tag{2.20}$$

Obviously, in the long-wavelength limit $\bar{q} \ll 1$ (keeping only quadratic terms in (2.20)), the two dispersion relations (2.19) and (2.20) agree. Fig. 2.3 compares the exact discrete and the approximate continuum dispersion relations (for $K_r = 10$) and demonstrates excellent agreement with deviations of less than 3 % up to $\bar{q} = 0.86$. Therefore, in the following we only consider long wavelengths, for which the governing equation assumes wave equation character (with dimensionless wave speed $\bar{c}_0^2 = K_r$):

$$\bar{u}_{,\bar{t}\bar{t}} - \bar{c}_0^2\, \bar{u}_{\bar{x}\bar{x}} - \bar{F}(\bar{u}) = 0. \tag{2.21}$$

2.5 Regimes of Wave Propagation

Owing to the nonlinearity of force $\bar{F}(\bar{u})$, we can identify three distinct regimes of wave propagation which depend on the magnitude of the amplitude of $\bar{u}$, and for

each case we seek solutions for the propagating wave by approximating the nonlinear force in (2.21). We discriminate the following three regimes of propagating waves:

(i) for **small amplitudes** $\bar{u} \ll 1$ we expand the nonlinear spring force to linear leading order as

$$\bar{F}(\bar{u}) \approx -\frac{2}{1+d^2}\bar{u} = -\omega_0^2\bar{u},$$

(ii) for **moderate amplitudes** $\bar{u} < 1$ we approximate the nonlinear force by a third-order Taylor expansion, i.e.

$$\bar{F}(\bar{u}) \approx -\frac{2}{1+d^2}\bar{u} + \frac{3d^2}{\left(1+d^2\right)^2}\bar{u}^2 - \frac{d^2\left(d^2-4\right)}{\left(1+d^2\right)^3}\bar{u}^3,$$

(iii) for **large amplitudes** $\bar{u} > 1$ we use the exact spring force,

$$\bar{F}(\bar{u}) = 2(1-\bar{u})\left(1-\frac{\bar{l}_0}{\bar{l}(u)}\right). \tag{2.22}$$

Fig. 2.4 illustrates the three approximations of the nonlinear spring force in comparison with the exact force for the specific choice of $d = 1$. We note that the nodal spacing a is independent of the characteristic spring length L and of ratio d, so that in the long-wavelength limit the governing equation for all three regimes is given by (2.21). The special case of amplitude $\bar{u} = 1$ is excluded because $\bar{u} = 1$

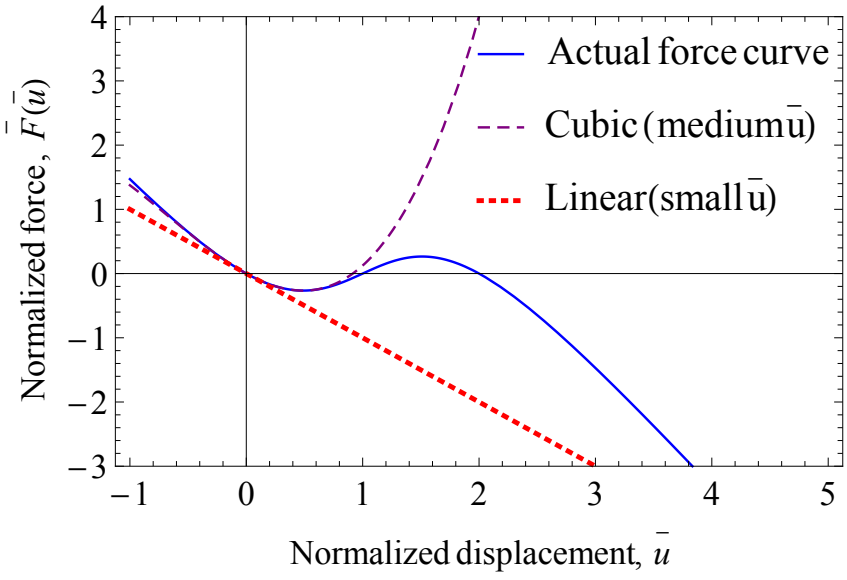

Figure 2.4: Nonlinear spring force and approximations introduced for the three regimes for $d = 1$.

corresponds to an unstable equilibrium configuration of the system. The smallest perturbation is sufficient to cause the system to snap into either energy well and thus to transform the scenario into either the $\bar{u} > 1$ or the $\bar{u} < 1$ case.

In the following sections, we will investigate the wave propagation behavior in all three regimes. To confirm our theoretical solutions, we will compare to numerical results obtained for the example parameters $d = 1$, $T = 1$ and $K_r = 10$, from which the three regimes are chosen as (i) $|\bar{u}| \leq 0.05$, (ii) $|\bar{u}| \leq 0.3$, and (iii) $|\bar{u}| \leq 2$. Convincing agreement has been verified for various combinations of these parameters, for brevity we here present only this specific case.

Numerical solutions are obtained from a chain of 100 elementary unit cells modeled in the time domain by an implicit finite difference scheme of Newmark-β type with parameters chosen to minimize numerical damping ($\beta = 0.25$, $\gamma = 0.5$). Displacement and/or velocity boundary conditions are directly imposed on the first node of the chain, while the remaining nodes may vibrate freely. All nodes are constrained to only move horizontally.

2.6 Small amplitude: linear solution

2.6.1 Analytical solution

The equation governing the wave propagation in this regime is given by

$$\bar{u}_{,\bar{t}\bar{t}} - \bar{c}_0^2\, \bar{u}_{\bar{x}\bar{x}} + \omega_0^2 \bar{u} = 0, \tag{2.23}$$

with ω_0^2 from (2.16). This is the dimensionless Linear Klein-Gordon equation [35] for the unknown displacement field $\bar{u}(\bar{x}, \bar{t})$. The theoretical solution for this problem is of the form

$$\bar{u}(\bar{x}, \bar{t}) = A\, \cos(\bar{q}\bar{x} - \bar{\omega}\bar{t}) + B\, \sin(\bar{q}\bar{x} - \bar{\omega}\bar{t}), \tag{2.24}$$

where the dimensionless wave number $\bar{q}$ and the dimensionless angular frequency $\bar{\omega}$ are related by the dispersion relation (2.19). Therefore, this regime admits the propagation of linear elastic waves at frequencies outside the stop bands characterized by the dispersion relations.

2.6.2 Numerical results

For the numerical benchmark test, the first node of the chain of bistable elements is excited by time-harmonic displacements (we enforce displacement and corresponding velocity boundary conditions at the first node) according to

$$\bar{u}_1(t) = \hat{u}\cos(\bar{\omega}\bar{t}) \quad \text{and} \quad \bar{u}_{1,t}(t) = -\hat{u}\,\bar{\omega}\sin(\bar{\omega}\bar{t}). \tag{2.25}$$

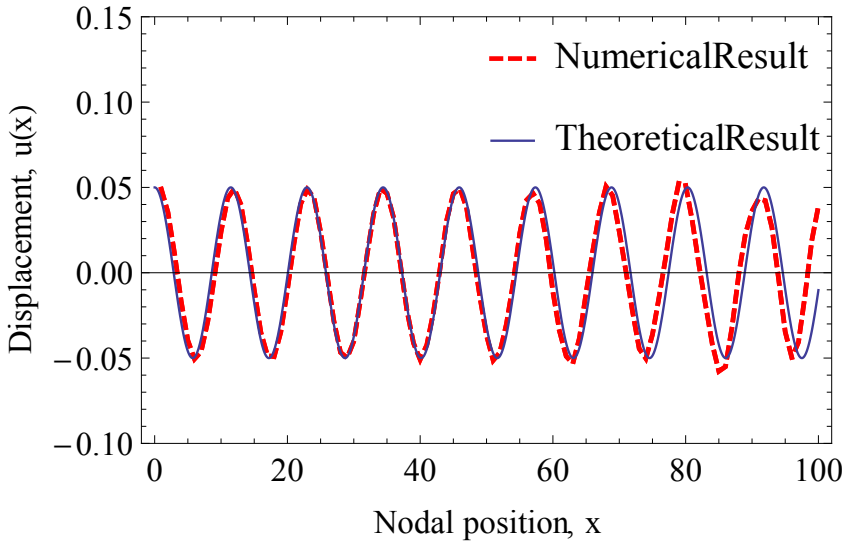

Figure 2.5: Small-amplitude regime: numerical results compared to the linear Klein-Gordon solution.

As only small amplitudes are permitted in this regime, we choose $\hat{u} = 0.05$ along with a value of $\bar{\omega} = 2$, such that the long wavelength limit holds, which becomes apparent from the dispersion relations in Fig 2.3. Transient effects are removed by artificial initial damping.

Fig 2.5 shows a comparison of the numerical solution with the theoretical solution in space, at a specific instant of time. The two solutions match with minor deviations due to numerical noise arising from the discrete solution (as the wave passes through the long chain towards its rightmost node, a weakly nonlinear effect causes the curve to slightly deviate from the theoretical solution). The wave speed can be inferred from the x-t-contour diagram of the numerical solution shown in Fig 2.6. The observed velocity of propagation agrees with the phase speed computed from the dispersion relation (also included as a solid red line). Nonlinear effects therefore only play a negligible role in this regime of small amplitudes, so that the linear Klein-Gordon solution is a legitimate approximation to describe and explain the wave propagation behavior in this regime.

2.7 Medium amplitude: weak nonlinearity

2.7.1 Analytical solution

For moderate displacements, the dimensionless governing equation in the continuum long-wavelength limit is approximated by

$$\bar{u}_{\bar{t}\bar{t}} - \bar{c}_0^2\,\bar{u}_{\bar{x}\bar{x}} + \frac{2}{1+d^2}\bar{u} - \frac{3d^2}{(1+d^2)^2}\bar{u}^2 + \frac{d^2(d^2-4)}{(1+d^2)^3}\bar{u}^3 = 0, \tag{2.26}$$

an equation of Cubic Nonlinear Klein-Gordon-type [67, 116] for the unknown displacement field $\bar{u}(\bar{x},\bar{t})$. The solution can be found by a perturbation multiple-scales expansion [103]. Therefore, we use the ansatz

$$\bar{u}(\bar{x},\bar{t}) = \epsilon\,\phi_0(\bar{x},\bar{t}) + \epsilon^2\phi_1(\bar{x},\bar{t}) + \epsilon^3\phi_2(\bar{x},\bar{t}) + O(\epsilon^4), \tag{2.27}$$

where $|\epsilon| \ll 1$ is a small characteristic length scale. For the current problem, the expansion is restricted to third order, since this approximation demonstrates sufficient accuracy for the medium amplitude regime, cf. Section 2.5. Suppose that in addition to variables $\bar{x}$ and $\bar{t}$, the solution depends on multiple scales of position and time. Then, new scaled variables can be defined by

$$X_i = \epsilon^i \bar{x} \quad \text{and} \quad T_i = \epsilon^i \bar{t}. \tag{2.28}$$

Again, we limit scales to order three. Consequently, we now seek solutions

$$\phi_i(\bar{x},\bar{t}) = \phi_i(X_0, X_1, X_2, T_0, T_1, T_2). \tag{2.29}$$

Derivatives with respect to the primary variables become

$$\frac{\partial}{\partial \bar{t}} = \sum_{i=0}^{2} \epsilon^i D_i, \qquad \frac{\partial}{\partial \bar{x}} = \sum_{i=0}^{2} \epsilon^i D_{Xi}, \qquad . \tag{2.30}$$

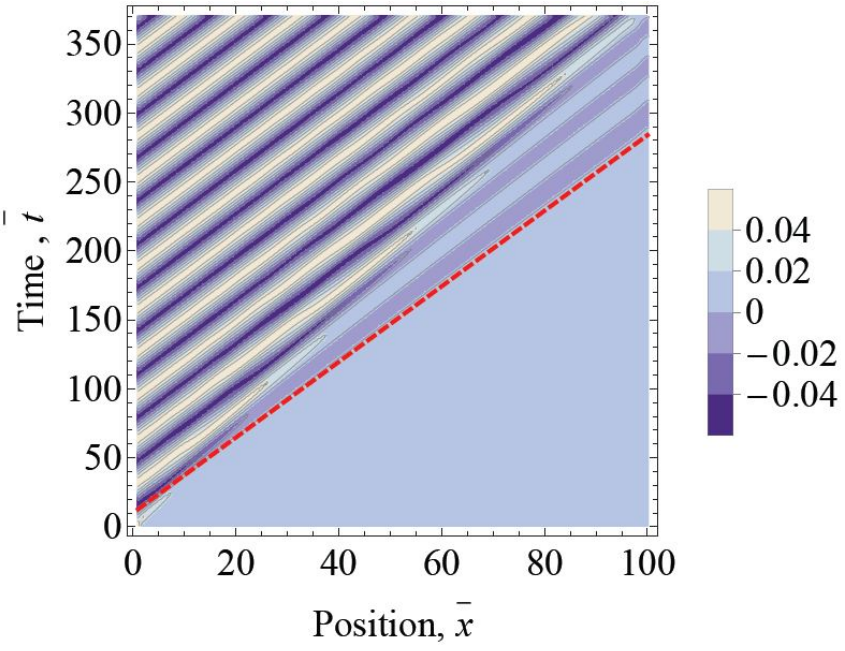

Figure 2.6: Small-amplitude regime: x-t-contour diagram of the numerical solution; for comparison, the solid red line represents a positive characteristic of the theoretical solution.

where we introduced operators

$$D_i = \frac{\partial}{\partial T_i}, \qquad D_{Xi} = \frac{\partial}{\partial X_i}. \tag{2.31}$$

Substitution of the chosen representation of the displacement field (4.9) into governing equation (2.23) and inspecting the equation at order $O(\epsilon)$ leads to

$$\mathcal{L}\,\phi_0 = 0 \qquad \text{with} \qquad \mathcal{L} = D_0^2 - \bar{c}_0^2 D_{X0}^2 + \omega_0^2. \tag{2.32}$$

Hence, the solution for the first-order expansion is of the form

$$\phi_0 = A(X_1, X_2, T_1, T_2) e^{i(\bar{q}X_0 - \bar{\omega}T_0)} + c.c. \tag{2.33}$$

Here and in the following $c.c.$ stands for the complex conjugate (for conciseness we do not write out both terms; the complex conjugate terms follow analogously). Frequency $\bar{\omega}$ and wave number $\bar{q}$ are related by the first-order dispersion relation for small amplitudes discussed above. At order $O(\epsilon^2)$, the governing equation reads

$$\begin{aligned}(D_0 + \epsilon D_1)^2(\epsilon\phi_0 + \epsilon^2\phi_1) - \bar{c}_0^2(D_{X0} + \epsilon D_{X1})^2(\epsilon\phi_0 + \epsilon^2\phi_1) \\ + \frac{2}{1+d^2}(\epsilon\phi_0 + \epsilon^2\phi_1) - \frac{3d^2}{(1+d^2)^2}(\epsilon\phi_0 + \epsilon^2\phi_1)^2 = 0,\end{aligned}$$

which can be algebraically reduced to the simpler form

$$\mathcal{L}\phi_1 = -(2D_0D_1 - 2c_0^2 D_{X0}D_{X1})\phi_0 + \frac{3d^2}{(1+d^2)^2}\phi_0^2. \tag{2.34}$$

Substitution of (2.33) into (2.34) and defining $\sigma = \bar{q}X_0 - \bar{\omega}T_0$ results in

$$\begin{aligned}\mathcal{L}\phi_1 = &\left(2i\bar{\omega}\frac{\partial A}{\partial T_1} + 2i\bar{q}\bar{c_0}^2\frac{\partial A}{\partial X_1}\right)e^{i\sigma} \\ &+ \frac{3d^2}{(1+d^2)^2}A^2e^{i2\sigma} + \frac{3d^2}{(1+d^2)^2}|A|^2 + c.c..\end{aligned} \tag{2.35}$$

For simplicity the overbars on c_0^2, q and ω will be dropped henceforth. Because σ is the eigenfrequency of the operator $\mathcal{L}$, the coefficient of the resonant term cancels, implying

$$\omega\frac{\partial A}{\partial T_1} + qc_0^2\frac{\partial A}{\partial X_1} = 0. \tag{2.36}$$

By introducing the group velocity $v_g = qc_0^2/\omega$ (which can be verified from the dispersion relation), we know that function A must be of the form

$$A(X_1, X_2, T_1, T_2) = A(X_1 - v_gT_1, X_2, T_2). \tag{2.37}$$

Therefore, (2.35) reduces to,

$$\mathcal{L}\phi_1 = \frac{3d^2}{(1+d^2)^2}A^2e^{i2\sigma} + \frac{3d^2}{(1+d^2)^2}|A|^2 + c.c. \tag{2.38}$$

The inhomogeneous solution is determined from the ansatz

$$\begin{aligned}\phi_1 =& B(X_1, X_2, T_1, T_2)e^{2i\sigma} + C(X_1, X_2, T_1, T_2)\\ &+ c.c.,\end{aligned} \tag{2.39}$$

which is substituted into (2.38). As A does not depend on X_0 and T_0, the non-oscillating terms corresponding to the absolute value cancel on both sides. Hence, only the resonant terms remain:

$$\begin{aligned}&(-4\omega^2 + 4\bar{c_0}^2q^2 + \omega_0^2)Be^{2i\sigma} + \omega_0^2C\\ &\quad= \frac{3d^2}{(1+d^2)^2}A^2e^{i2\sigma} + \frac{3d^2}{(1+d^2)^2}|A|^2 + c.c.\end{aligned} \tag{2.40}$$

Solving for B and C (ignoring complex conjugates) results in

$$B = -\frac{d^2}{2(1+d^2)} \quad \text{and} \quad C = \frac{3d^2}{2(1+d^2)}|A|^2, \tag{2.41}$$

which implies that

$$\phi_1 = -\frac{d^2}{2(1+d^2)}A^2e^{i2\sigma} + \frac{3d^2}{2(1+d^2)}|A|^2 + c.c. \tag{2.42}$$

Similarly at order $O(\epsilon^3)$, we have

$$\begin{aligned}&(D_0 + \epsilon D_1 + \epsilon^2 D_2)^2(\epsilon\phi_0 + \epsilon^2\phi_1 + \epsilon^3\phi_2)\\ &- c_0^2(D_{X0} + \epsilon D_{X1} + \epsilon^2 D_1 + \epsilon^3\phi_2)^2(\epsilon\phi_0 + \epsilon^2\phi_1 + \epsilon^3\phi_2)\\ &+ \omega_0^2(\epsilon\phi_0 + \epsilon^2\phi_1 + \epsilon^3\phi_2) + \tfrac{d^2(d^2-4)}{(1+d^2)^3}(\epsilon\phi_0 + \epsilon^2\phi_1 + \epsilon^3\phi_2)^2\\ &- \tfrac{6d^2}{(1+d^2)^2}(\epsilon\phi_0 + \epsilon^2\phi_1 + \epsilon^3\phi_2)^3 = 0,\end{aligned} \tag{2.43}$$

which, after canceling appropriate terms, reduces to

$$\begin{aligned}\mathcal{L}\phi_2 =& -\frac{d^2}{1+d^2}\left(2A\frac{\partial A}{\partial T_1}(-i\omega) - c_0^2 2A\frac{\partial A}{\partial X_1}(iq)\right)e^{i2\sigma}\\ &-\left(2\frac{\partial A}{\partial T_2}(-i\omega) - 2c_0^2\frac{\partial A}{\partial X_2}(iq) + \frac{\partial^2 A}{\partial T_1^2} - c_0^2\frac{\partial^2 A}{\partial X_1^2}\right)e^{i\sigma}\\ &+ \frac{12d^2}{(1+d^2)^2}|A|^2Ae^{i\sigma} - \frac{4d^2(d^2-1)}{(1+d^2)^3}A^3e^{i3\sigma}.\end{aligned} \tag{2.44}$$

Due to (2.36), the coefficient of the $e^{i2\sigma}$-term vanishes. To ensure finite amplitudes, the resonant term proportional to $e^{i\sigma}$ must not contribute to the solution. Consequently, the only remaining term gives

$$\mathcal{L}\phi_2 = -\frac{4d^2(d^2-1)}{(1+d^2)^3}A^3 e^{i3\sigma}. \tag{2.45}$$

with solution

$$\phi_2 = -\frac{d^2(d^2-1)}{4(1+d^2)^2}A^3 e^{i3\sigma}. \tag{2.46}$$

Since the coefficient of the resonant term in (2.44) must vanish, we also have

$$\begin{aligned} 2\frac{\partial A}{\partial T_2}(-i\omega) - 2c_0^2\frac{\partial A}{\partial X_2}(iq) + \frac{\partial^2 A}{\partial T_1^2} - c_0^2\frac{\partial^2 A}{\partial X_1^2} \\ - \frac{12d^2}{(1+d^2)^2}|A|^2 A = 0. \end{aligned} \tag{2.47}$$

Let us introduce the following new variables:

$$\begin{aligned} \xi_1 &= X_1 - v_g T_1 \quad \text{and} \quad \eta_1 = T_1, \\ \xi_2 &= X_2 - v_g T_2 \quad \text{and} \quad \eta_2 = T_2. \end{aligned} \tag{2.48}$$

Substitution into (2.47) and simplification finally yields (with overbars for the final solution)

$$i\frac{\partial A}{\partial \eta_2} + \frac{\bar{c}_0^2 - \bar{v}_g^2}{2\bar{\omega}}\frac{\partial^2 A}{\partial \xi_1^2} + \frac{6d^2}{\bar{\omega}(1+d^2)^2}|A|^2 A = 0. \tag{2.49}$$

(2.49) is a Nonlinear Schrödinger (NLS) equation for the unknown function A. Therefore, A scales with ϵ^2 in time and with ϵ in space. In general, a NLS equation of the form

$$i\frac{\partial A}{\partial \eta_2} + P\frac{\partial^2 A}{\partial \xi_1^2} + Q|A|^2 A = 0. \tag{2.50}$$

with coefficients $P, Q \in \mathbb{R}$ has two types of solutions [35, 168]:

$$\begin{aligned} PQ > 0 \quad &\Rightarrow \quad \text{envelope solitons} \\ PQ < 0 \quad &\Rightarrow \quad \text{dark solitons.} \end{aligned} \tag{2.51}$$

In the current case, one can verify that

$$PQ = \left(\frac{\bar{c}_0^2 - \bar{v}_g^2}{2\bar{\omega}}\right)\left(\frac{6d^2}{\bar{\omega}(1+d^2)^2}\right) = \frac{3c_0^2\omega_0^2 d^2}{\bar{\omega}^4(1+d^2)^2} > 0. \tag{2.52}$$

for all admissible values of $\bar{\omega}$. Therefore, the solution of the displacement field in this regime can be characterized as an envelope soliton [169] which is caused

by a Benjamin-Feir modulational instability [15, 168] of the wave as it propagates through the system for $PQ > 0$. A similar kind of modulational instability was observed in sine-Gordon and ϕ^4 problems [120]. The NLS equation can be solved exactly for function A [122], giving

$$A = V_m \,\mathrm{sech}\left(\sqrt{\frac{Q}{2P}}\,\epsilon\, V_m\,(\bar{x} - v_g\bar{t})\right)\exp\left[i(\epsilon V_m)^2\frac{Q}{2}\bar{t}\right], \tag{2.53}$$

where V_m is the characteristic amplitude of the wave and

$$\frac{Q}{2P} = \frac{6d^2\bar{\omega}^2}{\bar{c}_0^2\omega_0^2(1+d^2)^2} \quad \text{and} \quad \frac{Q}{2} = \frac{3d^2}{\bar{\omega}(1+d^2)^2}. \tag{2.54}$$

Therefore, at order $O(\epsilon)$ the displacement field can be expressed as

$$\bar{u}(\bar{x},\bar{t}) = \epsilon\, A(\bar{x},\bar{t})\,\exp(i\,\sigma) + c.c. \tag{2.55}$$

2.7.2 Numerical results

We use the same numerical setup as before to simulate the wave propagation behavior in this regime but we expand the number of nodes to 200 (to ensure sufficient level of detail to compare with the continuous solution). In order to see the formation of an envelope soliton due to modulational instability, a sinusoidal plane wave is imposed by the boundary conditions at the first node, viz. by enforcing

$$\bar{u}_1(\bar{t}) = \begin{cases} \hat{u}\cos(\bar{\omega}\bar{t}), & \text{for } 0 \le \bar{t} \le \bar{\tau}, \\ 0, & \text{else} \end{cases} \tag{2.56}$$

and

$$\bar{u}_{1,\bar{t}}(\bar{t}) = \begin{cases} -\hat{u}\,\bar{\omega}\sin(\bar{\omega}\bar{t}), & \text{for } 0 \le \bar{t} \le \bar{\tau}, \\ 0, & \text{else} \end{cases} \tag{2.57}$$

Instead of fixing the displacement at the first node for $\bar{t} \notin [0, \bar{\tau}]$, one can leave the first node traction-free without significantly affecting the solution. The boundary node at the other end of the chain is kept traction-free for all times.

Fig. 2.7 illustrates numerical results for the specific choices of $\hat{u} = 0.3$, $\bar{\omega} = 3$ and $\bar{\tau} = 10$. Results clearly confirm the propagation of a soliton, yet they show a variation of the envelope soliton as it moves through the lattice. The envelope of the waveform is seen to oscillate at a different frequency than the applied frequency at the first node. In order to verify the nature of the waveform, we show the Fourier spectrum in Fig. 2.8. In avoidance of spectral leakage due to the limitations of

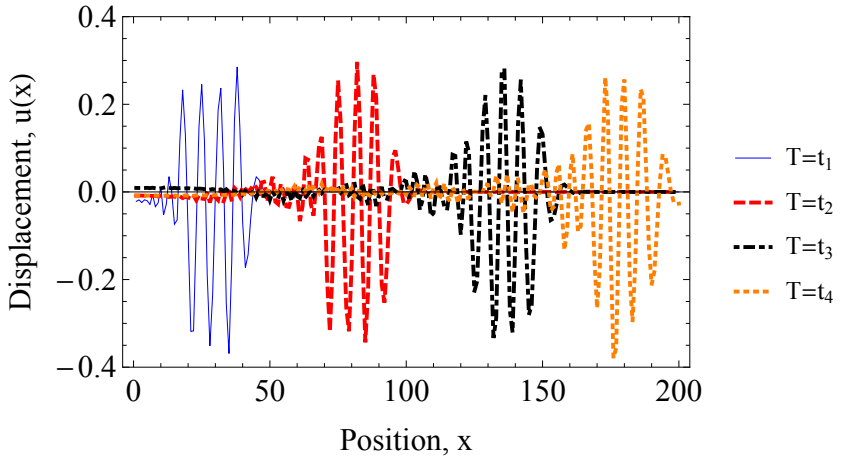

Figure 2.7: Snapshots of the propagating wave (traveling from left to right) at different instances of time show the evolution of the envelope soliton. The sech-type envelope begins to form due to self-modulation, as the wave passes through the lattice.

a discrete Fourier transform, Hann, Blackman and Hamming windows are used to determine the spectral content of the signal. The resulting peak frequency corresponds to the spatial wave number of the applied frequency. However, side lobes form which can be explained by the modulational instability [168] caused by the weakly-nonlinear effects discussed above. Hence, wave propagation in this regime can indeed be explained by the Non-Linear Schrödinger and the Cubic Non-Linear Klein-Gordon equations, and numerical results confirm the theoretical prediction of an envelope soliton. The envelope appears to vary as it moves along the chain; yet, the waveform preserves it localized nature, leaving behind small-amplitude high-frequency oscillations.

2.8 Large amplitude: strong nonlinearity

2.8.1 Analytical solution

For the case of large amplitudes, we use the exact nonlinear form of the potential energy. Therefore, the governing equation in the continuum limit is

$$\bar{u}_{\bar{t}\bar{t}} - \bar{c}_0^2 \bar{u}_{\bar{x}\bar{x}} - \bar{F}(\bar{u}) = 0. \tag{2.58}$$

For convenience, the over-bars are omitted in the following. We seek a traveling wave solution of the form $u(x,t) = u(x - vt) = u(z)$, where v is the propagation velocity and $z = x - vt$ a reduced variable. Substitution into (2.58) gives

$$(v^2 - c_0^2)\, u_{zz} - F(u) = 0. \tag{2.59}$$

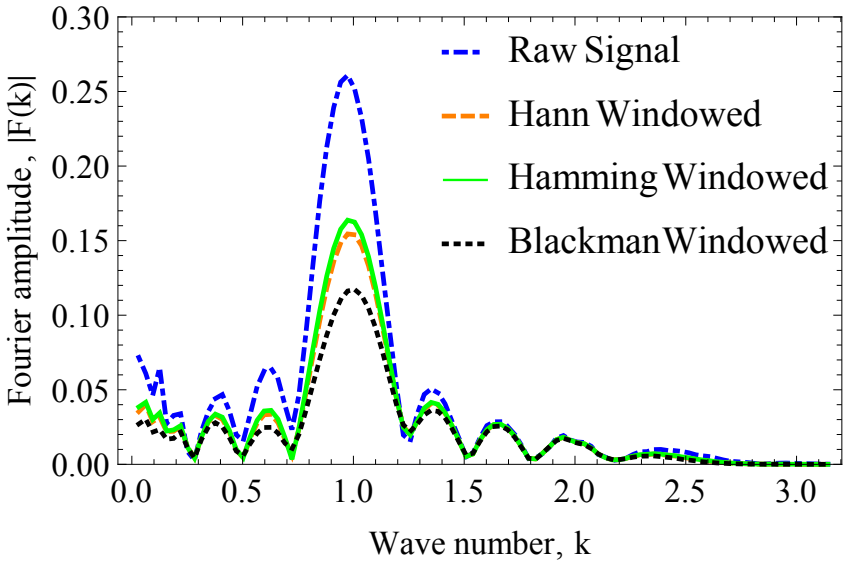

Figure 2.8: Discrete Fourier transform of the spatial variation of the waveform at a chosen instant of time.

Multiplication by $\frac{du}{dz}$ and integration leads to

$$\frac{v^2 - c_0^2}{2}\left(\frac{du}{dz}\right)^2 + \psi(u) = C_1, \tag{2.60}$$

where C_1 is a constant of integration. The value of C_1 can be computed from the initial conditions

$$\lim_{z\to\infty} u(z) = 0, \qquad \lim_{z\to\infty} \frac{du(z)}{dz} = 0 \tag{2.61}$$

which translate into

$$C_1 = 0. \tag{2.62}$$

Therefore, after some rearrangement (2.60) becomes

$$\sqrt{\frac{c_0^2 - v^2}{2}} \int \frac{du}{\sqrt{\psi(u)}} = z - z_0, \tag{2.63}$$

where z_0 is another constant of integration. Performing the integration results in

$$\begin{aligned} &\frac{2}{\sqrt{1+d^2}} \ln\left[a(u) + \frac{a(u)}{b(u)}\sqrt{1+d^2}\right] \\ &+ \ln\left(\frac{1-a(u)}{1+a(u)}\frac{1-b(u)}{1+b(u)}\right) = \sqrt{\frac{2}{c_o^2 - v^2}}\,(z - z_0) \end{aligned} \tag{2.64}$$

with the abbreviations

$$a(u) = u - 1, \qquad b(u) = \frac{\sqrt{1+d^2}(u-1)}{\sqrt{(u-1)^2 + d^2}}. \tag{2.65}$$

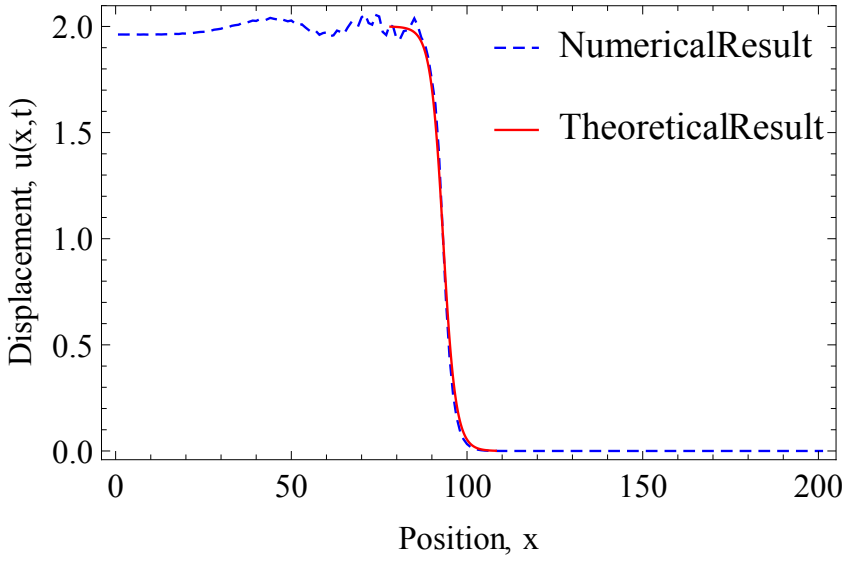

Figure 2.9: Comparison of theoretical large-amplitude solution and numerically-determined wave profile (for parameters $d = 1$, $z_0 = -93.2$ and $v = 2.812$).

In summary, the solution in the large-amplitude case is indeed a propagating wave of type $u(x,t) = u(x - vt)$. From (2.64) we conclude that $c_0 > v$ which implies that the wave speed is subsonic. Although (2.64) cannot be inverted to solve for $u(z)$ explicitly, the relation shows that $u(z) \to 0$ as $z \to \infty$ and that $u(z) \to 2$ as $z \to -\infty$. In addition, the function can be plotted parametrically for $u \in (0, 2)$, which is shown in Fig. 2.9. Obviously, the wave front is localized and of kink soliton type, which can be physically explained by the snap-through effect of each spring from one stable configuration to the other. The shape of the kink depends on the velocity of propagation with higher velocity kinks having steeper slopes.

2.8.2 Numerical results

We use the same numerical setup as before to simulate a chain of 100 bistable spring elements. We apply to the first node an initial velocity sufficiently high to make the first mass snap to its other stable branch. The other end of the chain is kept free at all times, i.e. zero tractions are enforced on that boundary. A comparison of the numerically-determined wave profile and the theoretical exact solution propagating with the same velocity is shown in Fig. 2.9. The perturbations in the numerical solution with respect to the theoretical solution are caused due discreteness effects [114]. To allow for a direct comparison, the velocity of propagation in the numerical example is found by linearly fitting the position of the leading edge in the x-t-contour plot in Fig. 2.10. The linear fit is shown in Fig. 2.11, which shows

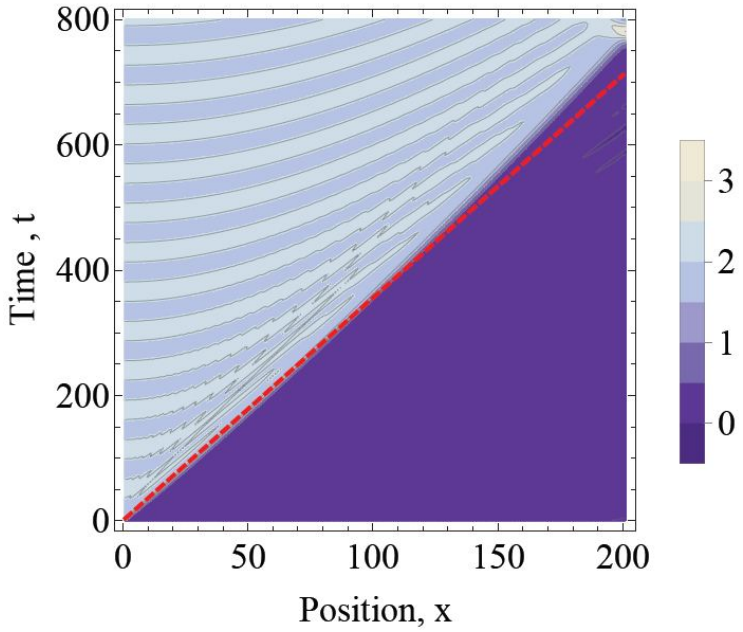

Figure 2.10: x-t-contour diagram of the numerical solution for the large-amplitude regime. The red straight line is the best fit line till $t = 250$ corresponding to the leading edge characteristic.

that the velocity is not constant but variations with time are marginal so that we may assume the wave is traveling at almost constant speed. Inserting the propagation velocity into the theoretical solution shows an excellent match with the numerical wave profile, which confirms the accuracy of the aforementioned analytical solution for the large-amplitude regime. The propagating wave is of anti-soliton nature with a topological charge of -1.

2.8.3 Energy of the kink soliton

Bistable elements have been shown to produce twinkling which results in energy dissipation, see e.g. ref. [44] and references therein. Here, we disregard just oscillations and focus on the propagating kink soliton whose energy can be determined by integrating the Hamiltonian spatial density over the complete lattice at any given time. The Hamiltonian density per unit spacing in the continuum limit is given by

$$h(x,t) = \tfrac{1}{2}u_t^2 + \tfrac{1}{2}c_0^2u_x^2 + \psi(u). \tag{2.66}$$

In the large-amplitude case as derived in Sec. 2.8.1, we have $u(x,t) = u(x - v\,t) = u(z)$. Substitution into (2.66) gives

$$h(z) = \left(\frac{v^2 + c_0^2}{2}\right)u_z^2 + \psi(u). \tag{2.67}$$

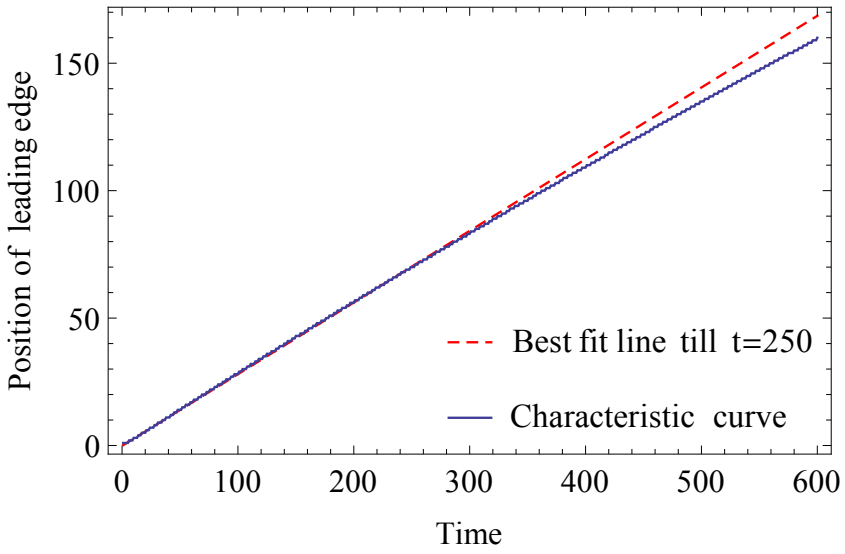

Figure 2.11: The characteristic curve corresponding to the leading edge of the wave is shown in comparison with the best-fit solution at $t = 250$. The slope of the line determines the initial speed of the propagating wave. This speed is used to compute the exact solution in the kink soliton propagation. The kink slows down toward the end due to the energy radiated by the oscillatory tail.

Replacing the value of $\psi(u)$ by using (2.60), we arrive at

$$h(z) = \left(\frac{v^2 + c_0^2}{2}\right) u_z^2 + \left(\frac{c_0^2 - v^2}{2}\right) u_z^2 = c_0^2 u_z^2 \tag{2.68}$$

Therefore, the total energy is computed by integrating $h(z)$ over the complete lattice, which results in

$$\begin{aligned} E &= \int_{-\infty}^{\infty} h(z)\,\mathrm{d}z \\ &= \frac{c_0^2}{\sqrt{2}\sqrt{c_0^2 - v^2}} \left[d^2 \ln\left(\frac{\sqrt{1+d^2}+1}{\sqrt{1+d^2}-1}\right) - 2\sqrt{1+d^2} \right]. \end{aligned} \tag{2.69}$$

Consequently, (3.16) implies that the energy increases with the propagation speed of the soliton. In combination with results from Sec. 2.8.1, we thus conclude that faster moving solitons have a steeper slope and have higher energy.

2.9 Effect of precompression

For the linear, weakly- and strongly-nonlinear regimes, we have shown how the wave characteristics (including the dispersion relations, wave speeds, and wave profiles) can be fine-tuned by changing the geometric parameter d. In addition, the nonlinearity of the bistable spring elements admits tailoring of the dynamic

response of the chain by applying initial pre-loads. Specifically, assume identical constant forces F_0 are applied to all masses in their direction of motion (e.g. by arranging the chain of springs vertically and letting the point masses pre-deform the bistable spring elements under the action of gravity, while the connecting linear springs remain unstretched in equilibrium). Consequently, all masses exhibit an initial equilibrium displacement u_0 that satisfies

$$F_0 = -\psi'(u_0). \tag{2.70}$$

Wave solutions are obtained by approximating the nonlinear force-displacement relation about this new initial equilibrium configuration. Let u denote the displacement from the new equilibrium state so that the total force on a bistable spring element becomes

$$F(u) = -\psi'(u_0 + u). \tag{2.71}$$

By using the dimensionless definitions of Section 2.3, we arrive at the equations of motion in the presence of pre-loads, viz.

$$\bar{u}_{i,\bar{t}\bar{t}} + K_r(-\bar{u}_{i+1} + 2\bar{u}_i - \bar{u}_{i-1}) - \bar{F}(\bar{u}) + \bar{F}_0 = 0 \tag{2.72}$$

or, after substitution of (2.70) and (2.71),

$$\bar{u}_{i,\bar{t}\bar{t}} + K_r(-\bar{u}_{i+1} + 2\bar{u}_i - \bar{u}_{i-1}) + \bar{\psi}'(\bar{u}_0 + \bar{u}_i) - \bar{\psi}'(\bar{u}_0) = 0. \tag{2.73}$$

For *small amplitudes* ($\bar{u} \ll 1$) we take

$$\bar{\psi}'(\bar{u}_0 + \bar{u}_i) \simeq \bar{\psi}'(\bar{u}_0) + \bar{\psi}''(\bar{u}_0)\,\bar{u}_i, \tag{2.74}$$

which again leads to a linearized Klein-Gordon equation, viz.

$$\bar{u}_{i,\bar{t}\bar{t}} + K_r(-\bar{u}_{i+1} + 2\bar{u}_i - \bar{u}_{i-1}) + \bar{\psi}''(\bar{u}_0)\,\bar{u}_i = 0. \tag{2.75}$$

Therefore, the same solution derived above applies when defining

$$\omega_0^2 = \bar{\psi}''(\bar{u}_0) = 2\left[1 - \frac{d^2\sqrt{1+d^2}}{(d^2 + (\bar{u}_0 - 1)^2)^{3/2}}\right], \tag{2.76}$$

which naturally reduces to (2.16) when choosing $\bar{u}_0 = 0$. Therefore, pre-deformation u_0 can be utilized to manipulate the dispersion relation (2.19). We note that the amount of pre-compression is limited before snapping occurs. Specifically, (2.76) only yields real-valued wave speeds if

$$u_0 \leq 1 - d\sqrt{(1+d^{-2})^{1/3}}. \tag{2.77}$$

Next, let us consider *moderate amplitudes*. The applicability of this regime now depends on the pre-defromation. $\psi'(\bar{u}+\bar{u_0})-\psi'(\bar{u_0}) = 0$ generally has two solutions $\{\bar{u}^*, \bar{u}^{**}\}$ with $\bar{u}^* < \bar{u}^{**}$. In the following, we assume moderate amplitudes that satisfy $\bar{u}^* + \bar{u}_0 < \bar{u}^{**}$ to prevent snapping. A third-order Taylor expansion of the nonlinear spring force turns (2.73) into

$$\begin{aligned} \bar{u}_{i,\bar{t}\bar{t}} + K_r(-\bar{u}_{i+1} + 2\bar{u}_i - \bar{u}_{i-1}) + \bar{\psi}''(\bar{u}_0)\,\bar{u}_i \\ + \frac{1}{2}\bar{\psi}'''(\bar{u}_0)\,\bar{u}_i^2 + \frac{1}{6}\bar{\psi}''''(\bar{u}_0)\,\bar{u}_i^3 = 0. \end{aligned} \tag{2.78}$$

A multiple-scales expansion approach again leads to a Nonlinear Schrödinger equation, which in turn gives rise to a wave profile of envelope soliton type as derived in Section 2.7, the details of which are omitted here due to the close analogy to the previous analysis.

Finally in case of *large amplitudes* we use the exact forcing function which gives rise to the governing equation in the continuum limit of the following form:

$$\bar{u}_{\bar{t}\bar{t}} - \bar{c}_0^2 u_{\bar{x}\bar{x}} + \psi'(\bar{u} + \bar{u}_0) - \psi'(\bar{u}_0) = 0. \tag{2.79}$$

The application of a pre-load F_0 results in a change of the total potential energy landscape due to the work performed by F_0. In particular, the two energy wells are no longer symmetric but exhibit different energy levels (depending upon the direction and magnitude of F_0). Fig. 2.12 shows the total potential energy

$$E(u) = \psi(u + u_0) - \psi'(u_0)u \tag{2.80}$$

for positive and negative pre-deformation u_0.

When the force F_0 points away from the direction of snapping, it leads to an unstable kink which disintegrates into ripples about the initial equilibrium point and does not show interesting wave propagation phenomena (yet, it allows for the absorption of impact energy). However, when the pre-load is in the direction of snapping, the energy landscape becomes negative near its second well. To date, all models of the Frenkel-Kontorova type have dealt with potentials that are either fully positive or negative in the transition region. In contrast, the mechanical system studied here produces a potential which is partially positive and partially negative in the transition region. Even for a small amount of pre-compression (cf. Fig. 2.13) the stability of the kink increases and the effect of discreteness (i.e. phonon radiation) to lower the wave speed is reduced [114]. The x-t contour plot for the wave propagation shown

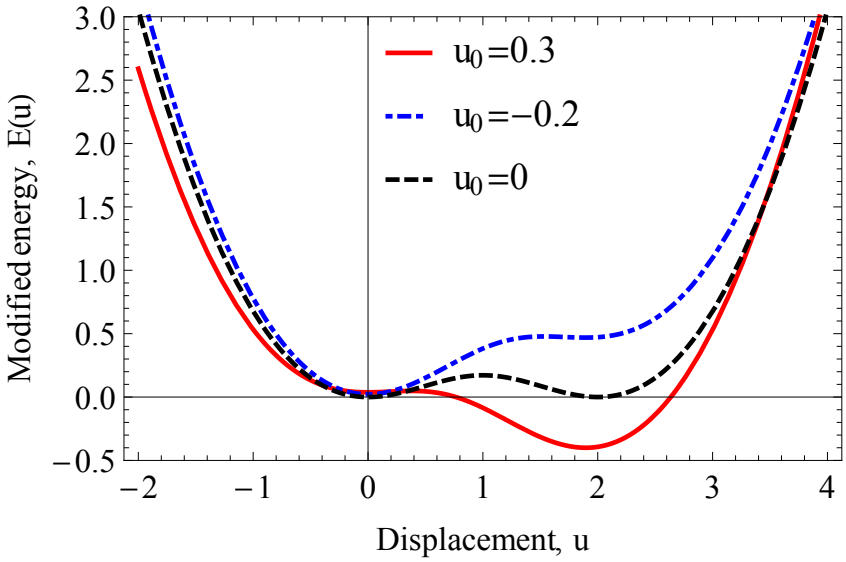

Figure 2.12: Energy landscape $E(u)$ with positive and negative pre-deformation as well as without pre-loads.

in Fig. 2.13 confirms that the kink characteristic is now linear and hence the kink has stabilized as compared to the case without precompression, cf. Fig. 2.10.

Increasing the pre-compression creates a combination of a kink and trailing oscillations which are localized as the wave moves through the chain. After attaining a

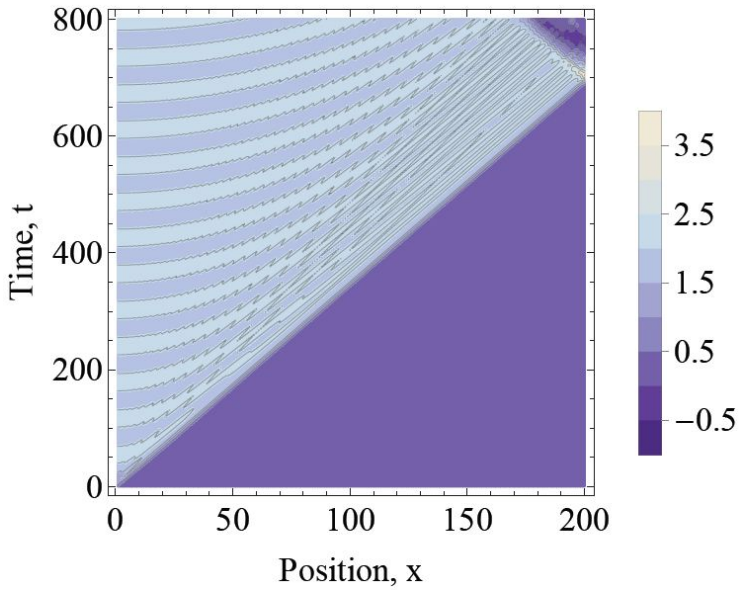

Figure 2.13: x-t-contour diagram of the numerical solution for a precompression $\bar{u}_0 = 0.03$. The kink characteristic is relatively straighter than the characteristic without precompression.

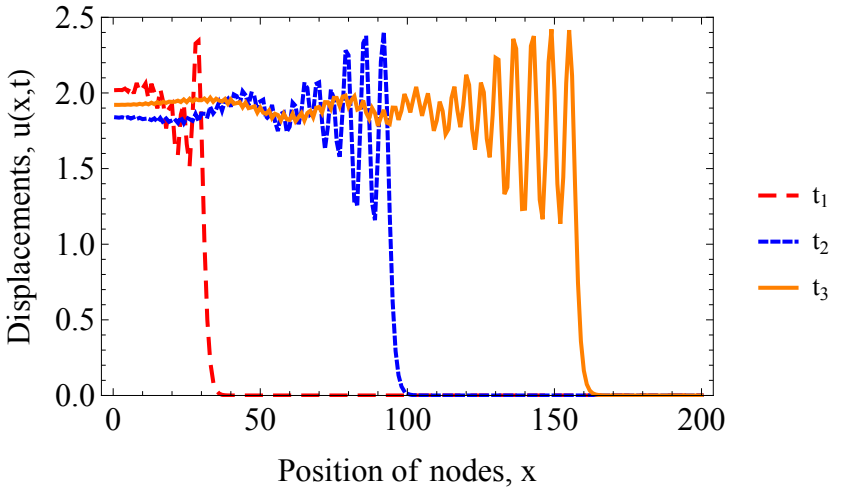

(a)

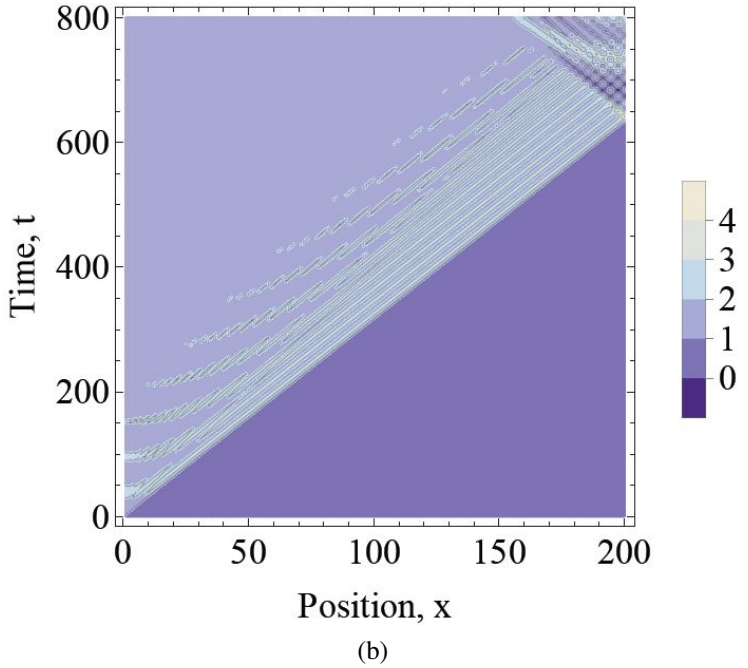

(b)

Figure 2.14: (a) Wave profiles for $\bar{u}_0 = 0.3$ and $t_3 > t_2 > t_1$. (b) x-t-contour diagram of the numerical solution for a precompression of $\bar{u}_0 = 0.3$.

certain width of localization, the oscillations acquire a steady shape and propagate with the kink velocity. Fig. 2.14 illustrates a typical wave profile and an x-t contour diagram for the case of pre-compression (both have been obtained numerically). The oscillations forming in the wake of the kink are bounded by an envelope as in the case of the envelope soliton forming under medium amplitudes, see Section 2.7. This can be explained by the reduction in potential energy as each spring transitions from one energy well to the other. As shown in Fig. 2.12, a pre-load into

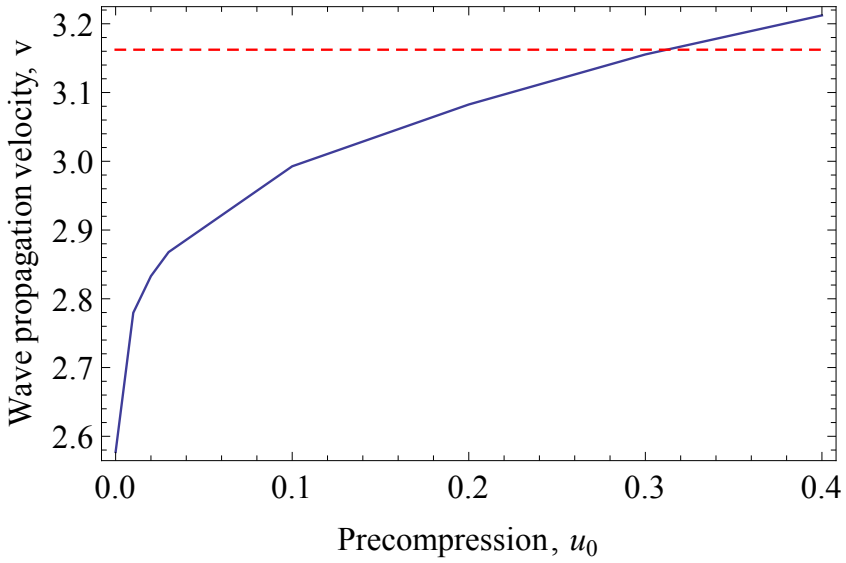

Figure 2.15: Variation of the kink propagation velocity with pre-compression for an initial (normalized) velocity of the first node of $v_0 = 4$. The dotted line shows the characteristic sound speed $\bar{c}_0$ of the medium for comparison.

the direction of snapping results in the snapped potential well having lower energy. Consequently, after snapping every mass has residual kinetic energy. This energy, however, is insufficient for a spring to snap back since part of the energy is carried away by the kink soliton. Hence, the masses oscillate in the snapped well with a medium amplitude giving rise to localization by modulational instability as seen in the envelope soliton case in Section 2.7. For these reasons, the pre-deformation results in a combination of the two modes of kink and envelope soliton propagation with an envelope soliton-like wave created behind the kink. As may be expected, the velocity of the propagating wave front increases with increasing pre-compression for a constant input of energy as shown in Fig. 2.15. There is a sharp rise in the velocity of propagation for small pre-compressions followed by a fairly linear increase for large pre-compressions, ultimately becoming supersonic.

2.10 Conclusions

We have shown that mechanical chains of bistable nonlinear-elastic elements offer a rich dynamic response with distinct regimes of wave propagation depending on the excitation amplitude. For small amplitudes, the chain propagates elastic waves in the linear regime characterized by wave dispersion. For moderate amplitudes, owing to modulational instability an envelope soliton forms and propagates. For large amplitudes, the strongly nonlinear chain shows topological kink solitary waves. In

all three regimes, we have derived analytical solutions of the displacement field in the continuum limit and we have demonstrated excellent agreement with the numerical solution obtained from a discrete chain of bistable elements. Wave propagation characteristics can be controlled by fine-tuning the geometric details of the bistable elements. Moreover, precompression brings the bistable elements closer to their snapping instability and hence can be used to control the wave propagation. We discussed the influence of precompression in all three amplitude regimes.

Our results highlight opportunities to design periodic mechanical structures and metamaterials containing bistable (negative-stiffness) elements that give rise to beneficial dynamic performance. This closes a gap between previous research on composite systems with (static) negative-stiffness phases and the nonlinear dynamics of structures undergoing large elastic deformation. Here, the negative-stiffness effect (i.e. the unstable branch of the force-displacement curve) is utilized to create and propagate solitary wave packages, which presents a novel way to achieve controllable metamaterial performance through negative-stiffness elements, while previous research in negative-stiffness materials mainly focused on their elastic and viscoelastic effective properties well within the realm of linearized kinematics. We deliberately chose a simple (possibly the simplest) elastic system to show the sought effects while allowing for closed-form analytical solutions, a rare find in nonlinear dynamics. The same qualitative response can be expected from various structural systems that allow for practical implementation. For example, the bistable spring elements can be replaced by buckled columns or membranes, and the elastic springs connecting the bistable elements by compliant fillers. Experimental construction of lattices of such elements has been shown in Chapter 5.

Chapter 3

NONLINEAR DYNAMICS OF DISSIPATIVE AND DIFFUSIVE PHASE TRANSITIONS

Research presented in this chapter has been adapted from the following publication:

Neel Nadkarni, Chiara Daraio, Rohan Abeyaratne, and Dennis M. Kochmann. "Universal energy transport law for dissipative and diffusive phase transitions". In: *Physical Review B* 93.10 (Mar. 2016), p. 104109. DOI: 10.1103/PhysRevB.93.104109. URL: http://link.aps.org/doi/10.1103/PhysRevB.93.104109.

In the previous chapter, the lattice of bistable elements was conservative in nature. In this chapter, we analyze the nonlinear mechanics of phase transitions in lattices that are governed by dissipative or diffusive dynamics. We present a scaling law for the kinetic energy and speed of transition waves in such media. By considering uniform discrete lattices and continuous solids, we show that, for arbitrary highly-nonlinear many-body interactions and multi-stable on-site potentials, the kinetic energy per density transported by a planar transition wave front always exhibits linear scaling with wave speed and the ratio of energy difference to interface mobility between the two phases. We confirm that the resulting linear superposition applies to highly-nonlinear examples from particle to continuum mechanics.

3.1 Introduction

Based on the nature of the phase transition process, systems are characterized as non- or weakly-dissipative, dissipative, or diffusive. Non- or weakly-dissipative models have been used to explain phenomena such as dislocation motion [51], ferromagnetic domain wall motion [19], proton mobility in hydrogen-bonded chains [63], rotation of DNA bases [113], chains of rotating pendulums [130], or lattices of bistable buckled, elastic structures [99]. The dynamics of such a non-dissipative lattice was described in Chapter 2. In contrast, diffusive or dissipative kinetics play an essential role in explaining the physics of, e.g., ferroelectric domain switching [53], magnetic flux propagation in Josephson junctions with tunneling losses [143], pulse propagation in cardiophysiology [65] and neurophysiology [131], sliding friction [158], chemical surface adsorption [124], under-damped commen-

surate phase transitions [24], defect conductivity in super-ionic conductors [140], or dynamics of CNT foams [48, 146], few of which were outlined in Chapter 1. Although numerous theoretical studies have been devoted to characterizing the motion of phase boundaries particularly in 1D periodic physical, chemical or biological systems, see e.g. [3, 9, 25, 27, 31, 33, 121, 150] and references therein, the lessons learned almost exclusively apply to special cases only, owing to the variety of nonlinear interaction potentials and non-convex on-site potentials. Here, we present a surprisingly simple universal energy law that applies to diffusive and dissipative systems and uniquely links the speed and profile of transition waves to the energetics and kinetics of the periodic system.

All of the above examples of diffusive and dissipative systems, including continuous and discrete systems, essentially reduce to the same type of governing equation that describes the nonlinear wave motion. For the discrete case, this may be interpreted as the equations of motion of a periodic 1D array of N elements whose displacements $u_n(t)$ at time t satisfy (for $n = 1, \ldots, N$)

$$\begin{aligned} &m\, u_{n,tt} + \alpha\, u_{n,t} + \phi'(u_n) \\ &- \sum_{j=1}^{N_b} \left[V_j'\left(\frac{u_{n+j} - u_n}{ja}\right) - V_j'\left(\frac{u_n - u_{n-j}}{ja}\right)\right] = 0, \end{aligned} \tag{3.1}$$

where m is the mass of each element, V denotes a nonlinear interaction potential (assuming long-range pairwise interactions), N_b represents the number of neighbor interactions, ϕ is the (multi-stable, i.e., non-convex) on-site potential and a introduces the equilibrium spacing between masses with primes and variables in indices denoting partial derivatives.

The analogous continuous governing equation, as we will show, is obtained by taking the continuum limit of (3.1) as $a \to 0$. Replacing discrete variables u_n by the continuous field $u(x,t)$ such that $u_n(t) = u(na,t)$ leads to the continuous governing equation

$$\rho\, u_{,tt} + \gamma\, u_{,t} + \psi'(u) - \sum_{j=1}^{N_b} j\, u_{,xx} V_j''(u_{,x}) = 0, \tag{3.2}$$

with mass density ρ and rescaled damping parameter γ and non-convex potential ψ. The aforementioned physical, chemical, or biological systems reduce to either (3.1) or (3.2).

As in most of the examples, we consider velocity-proportional damping characterized by the dissipation parameter $\alpha > 0$ for the discrete case or $\gamma > 0$ for the

continuum. For a non- or weakly-dissipative system, the damping term is negligible compared to the inertial term ($|mu_{n,tt}| \gg |\alpha u_{n,t}|$ or $|\rho u_{,tt}| \gg |\gamma u_{,t}|$). The energy transport in such systems is described well by its Hamiltonian which remains approximately constant as the wave propagates. However, energy transport in dissipative ($|mu_{n,tt}| \sim |\alpha u_{n,t}|$ or $|\rho u_{,tt}| \sim |\gamma u_{,t}|$) or diffusive lattices ($|mu_{n,tt}| \ll |\alpha u_{n,t}|$ or $|\rho u_{,tt}| \ll |\gamma u_{,t}|$) is not well understood at present. Therefore, in this chapter, we focus on the dynamics of diffusive and dissipative systems and derive an explicit energy transport law for such systems. We show that the law holds for both discrete and continuous systems.

3.2 Theoretical analysis

Transition waves, i.e., the motion of phase boundaries in multi-stable lattices, is commonly characterized by a steady-state wave form that propagates through the medium with kinetic energy concentrated in the moving wave front. That is, away from the moving phase boundary, the system attains an equilibrium in one of the stable energy wells of ϕ. Let us begin by studying the propagation of transition waves in discrete lattice systems with governing equations of the form (3.1). Next, we will derive the continuum limit (3.2) from (3.1) and show that the kinetic energy transport in both types of systems is governed by the same energy scaling law.

3.2.1 Energy transport in discrete lattices

We begin by assuming a traveling wave solution of the form $u_n(t) = u(na - vt) = u(\xi)$ so that (3.1) becomes

$$\begin{aligned} &mv^2 u_{,\xi\xi} - v\alpha u_{,\xi} + \phi'(u) \\ &- \sum_{j=1}^{N_b} \left[V_j' \left(\tfrac{u(\xi+ja)-u(\xi)}{ja} \right) - V_j' \left(\tfrac{u(\xi)-u(\xi-ja)}{ja} \right) \right] = 0. \end{aligned} \tag{3.3}$$

Multiplying by $u_{,\xi}$ and integrating over the real axis gives

$$\begin{aligned} &\int_{-\infty}^{\infty} \left[mv^2 u_{,\xi\xi} - v\alpha u_{,\xi} + \phi'(u) \right] u_{,\xi} \, \mathrm{d}\xi \\ &= \sum_{j=1}^{N_b} \int_{-\infty}^{\infty} \left[V_j' \left(\tfrac{u(\xi+ja)-u(\xi)}{ja} \right) - V_j' \left(\tfrac{u(\xi)-u(\xi-ja)}{ja} \right) \right] u_{,\xi} \, \mathrm{d}\xi. \end{aligned} \tag{3.4}$$

Let us first examine an individual integral on the right-hand side. Define $\eta = \xi - ja$ and redefine the integral with respect to η in the second term, thereby transforming

the right-hand side terms into

$$\begin{aligned} F_j &= \int_{-\infty}^{\infty} \left[V_j'\left(\tfrac{u(\xi+ja)-u(\xi)}{ja}\right) - V_j'\left(\tfrac{u(\xi)-u(\xi-ja)}{ja}\right)\right] u_{,\xi}\,\mathrm{d}\xi \\ &= \int_{-\infty}^{\infty} V_j'\left(\tfrac{u(\xi+ja)-u(\xi)}{ja}\right) u_{,\xi}(\xi)\,\mathrm{d}\xi \\ &\quad - \int_{-\infty}^{\infty} V_j'\left(\tfrac{u(\eta+ja)-u(\eta)}{ja}\right) u_{,\xi}(\eta+ja)\,\mathrm{d}\eta. \end{aligned} \tag{3.5}$$

By changing the dummy variable η back to ξ, and defining $z = \frac{u(\xi+ja)-u(\xi)}{ja}$ with $\mathrm{d}z = \frac{u_{,\xi}(\xi+ja)-u_{,\xi}(\xi)}{ja}\,\mathrm{d}\xi$, (3.5) reduces to

$$F_j = -ja \int_{z(\xi\to-\infty)}^{z(\xi\to\infty)} V_j'(z)\,\mathrm{d}z. \tag{3.6}$$

Now, since the system is dissipative or dispersive, we assume that the wave profile reaches a steady state and, in particular, as $t \to \infty$ (or $\xi \to -\infty$) we have $u(\xi+ja) - u(\xi) \to 0$ and $z(\xi) \to 0$. Analogously, since the system is initially at rest, we know $u(\xi+ja) - u(\xi) \to 0$ and $z(\xi) \to 0$ as $t \to -\infty$ (or $\xi \to \infty$). Thus, the system is in equilibrium and unstretched far from the wave front, in the sense that both particle velocity and relative displacement vanish in the remote fields, ahead of and behind the kink. Therefore, we must have $F_j = 0$. By a similar argument, the integral of the inertial term on the left-hand side of (3.4) goes to zero. If the transition wave switches the state variable from the initial value $u_i = \lim_{\xi\to\infty} u(\xi)$ to the final value $u_f = \lim_{\xi\to-\infty} u(\xi)$, then the on-site potential contribution becomes

$$\int_{-\infty}^{\infty} \phi'(u) u_{,\xi}\,\mathrm{d}\xi = \phi(u_i) - \phi(u_f) = \Delta\phi, \tag{3.7}$$

Therefore, (3.4) becomes

$$v \int_{-\infty}^{\infty} u_{,\xi}^2\,\mathrm{d}\xi = \frac{\Delta\phi}{\alpha} = \frac{\Delta\psi}{\gamma}. \tag{3.8}$$

where we introduced $\psi = \phi/a$ and $\gamma = \alpha/a$ as the on-site potential per length and linear damping per length, respectively. As we will show in the continuous case below, $\gamma, \psi = O(1)$ as $a \to 0$. For large wave widths $w \gg a$, the total transported kinetic energy per mass density $\rho = m/a$ of the discrete lattice is given by

$$E_d = \sum_i \frac{1}{2} u_{i,t}^2\, a = v^2 \sum_i \frac{1}{2} u_{i,\xi}^2\, a \approx \frac{v^2}{2} \int_{-\infty}^{\infty} u_{,\xi}^2\,\mathrm{d}\xi\,. \tag{3.9}$$

Combining (3.8) and (3.9) gives a simple result for the transported energy as

$$\frac{E_d}{v} \simeq \frac{\Delta\psi}{2\gamma}. \tag{3.10}$$

Therefore, for a diffusive or dissipative lattice the ratio of the transported kinetic energy per density to the wave speed depends only and linearly upon the ratio of the change in the on-site potential energy to the dissipation parameter.

3.2.2 Energy transport in continuous systems

Let us first derive the continuum limit (3.2) of the discrete equation (3.1). We consider a lattice made up of N nodes with constant spacing a. Therefore, the macroscopic total length is $L = (N-1)a$. In the continuum limit, we let $N \to \infty$ while keeping the macroscopic length L fixed. Therefore $a \to 0$ and, as $N \gg 1$, $L \simeq Na$. In the continuum limit of $a \to 0$, we first introduce Taylor expansions for u_{n+j} for each interaction potential term, which gives

$$V_j'\left(\frac{u_{n+j}-u_n}{ja}\right) = V_j'(u_{,x}) + \frac{ja}{2}\,u_{,xx}V_j''(u_{,x}) + O(a^2).$$

Insertion into (3.1) and division by a results in

$$\rho v^2 u_{,\xi\xi} - \sum_{j=1}^{N_b} j\,V_j''(u_{,\xi})u_{,\xi\xi\xi} + O(a) - v\frac{\alpha}{a}u_{,\xi} + \frac{1}{a}\phi'(u) = 0,$$

where $\rho = m/a$ is the mass density. When transitioning from a discrete lattice to a continuum, certain macroscopic quantities should remain finite or of $O(1)$ for physical reasons (otherwise, the continuum limit is physically nonsensical). As L is kept fixed and independent of a, we have $L = O(1)$. This results in the following scalings:

(i) The total (macroscopic) mass M must remain finite and constant:

$$M = mN \sim O(1) \;\Rightarrow\; \rho = m/a = M/L \sim O(1). \tag{3.11}$$

Hence, the mass density remains finite and constant.

(ii) The macroscopic energy density of the on-site potential well must remain finite:

$$\sum_{i=1}^{N}\phi(u_i) = \tfrac{1}{a}\int_0^L \phi(u)\,dx \sim O(1) \;\Rightarrow\; \phi(u)/a \sim O(1), \tag{3.12}$$

which directly leads to the conclusion that the forcing function should vary such that $\psi'(u) = \phi'(u)/a \sim O(1)$.

(iii) The macroscopic dissipation potential must remain finite:

$$\sum_{i=1}^{N} \frac{1}{2}\alpha u_{i,t}^2 = \frac{\alpha}{a}\int_0^L \frac{1}{2}u_{,t}^2\, dx \sim O(1) \;\Rightarrow\; \alpha/a \sim O(1). \tag{3.13}$$

Hence, we define $\gamma = \alpha/a \sim O(1)$ which must remain finite in the continuum limit.

Overall, we thus obtain the continuum balance equation (3.2):

$$\rho u_{,tt} - \sum_{j=1}^{N_b} j\, V_j''(u_{,x})u_{,xx} + \gamma u_{,t} + \psi'(u) = 0. \tag{3.14}$$

Now, assuming a traveling wave solution of the form $u(x,t) = u(x - vt) = u(\xi)$ and substituting in (3.14), we obtain

$$\rho v^2 u_{,\xi\xi} - \sum_{j=1}^{N_b} j\, V_j''(u_{,\xi})u_{,\xi\xi} - v\gamma u_{,\xi} + \psi'(u) = 0. \tag{3.15}$$

Multiplying by $u_{,\xi}$ and integrating over the real axis gives

$$\begin{aligned}\int_{-\infty}^{\infty}\left(\rho v^2 - \sum_{j=1}^{N_b} jV_j''(u_{,\xi})\right)u_{,\xi}u_{,\xi\xi}\,\mathrm{d}\xi \\ + \int_{-\infty}^{\infty}\psi'(u)u_{,\xi}\,\mathrm{d}\xi = v\gamma\int_{-\infty}^{\infty}u_{,\xi}^2\,\mathrm{d}\xi.\end{aligned} \tag{3.16}$$

Without loss of generality, we assume that $v > 0$ (the wave travels in the positive direction) and the system is diffusive or dissipative. Like in the discrete case, we assume that the wave profile reaches a steady state, and the particle velocity and strain vanish in the remote fields, ahead of and behind the kink, leading, again, to the conclusion that $u_{,\xi} \to 0$ as $\xi \to \pm\infty$. Consequently, we see that

$$\int_{-\infty}^{\infty}\left(\rho v^2 - \sum_{j=1}^{N_b} jV_j''(u_{,\xi})\right)u_{,\xi}\frac{\mathrm{d}u_{,\xi}}{\mathrm{d}\xi}\,\mathrm{d}\xi = 0. \tag{3.17}$$

If the transition wave switches the state variable from the initial value $u_i = \lim_{\xi\to\infty} u(\xi)$ to the final value $u_f = \lim_{\xi\to-\infty} u(\xi)$, then the on-site potential contribution becomes

$$\int_{-\infty}^{\infty}\psi'(u)u_{,\xi}\,\mathrm{d}\xi = \psi(u_i) - \psi(u_f) = \Delta\psi \tag{3.18}$$

and (3.16) reduces to the simple relation

$$\Delta\psi = v\gamma \int_{-\infty}^{\infty} u_{,\xi}^2 \, d\xi, \tag{3.19}$$

which can be linked to the total kinetic energy per density ρ transported by the transition wave, viz.

$$E = \int_{-\infty}^{\infty} \frac{1}{2} u_{,t}^2 \, \mathrm{d}x = \frac{1}{2} v^2 \int_{-\infty}^{\infty} u_{,\xi}^2 \, \mathrm{d}\xi. \tag{3.20}$$

By combining (3.19) and (3.20), we arrive at the universal scaling law

$$\frac{E}{v} = \frac{\Delta\psi}{2\gamma}, \tag{3.21}$$

which agrees with (3.10) for large wave widths ($E_d \approx E$).

3.2.3 Results

As shown above, the energy transport in diffusive or dissipative continua in discrete lattices and continuous media obey the same scaling law, viz. that the ratio of the transported kinetic energy per density to the wave speed is linearly proportional to the ratio of the change in the on-site potential energy to the dissipation parameter. We note that even in the limit $\rho \to 0$ the kinetic energy per unit density, E (or E_d in the discrete case), remains a finite quantity, so the law (3.21) applies, as long as the system response remains a traveling kink. Quantity E (or E_d) can be obtained experimentally from the particle velocities (or two snapshots from subsequent time steps).

Some of the remarkable features of this scaling law are:

(i) The inter-particle forcing does not affect the ratio, i.e., the above law holds for any nonlinear interaction potential V.

(ii) The law is independent of the number of interacting neighbors, N_b.

(iii) It is independent of the topology of the on-site potential ϕ but depends only on the difference $\Delta\psi$ between the initial and final energy of a bi-stable transition.

(iv) For $E > 0$, we must have $\Delta\psi > 0$; i.e., stable mobile transition waves can only occur when switching from higher to lower potential energy.

(v) The scaling law is linear despite the governing equations being highly nonlinear. This suggests that in the case of multi-well transitions, the transported

energy must follow from linear superposition of the individual two-well transitions.

The law can also be interpreted as follows. The ratio of kinetic energy per unit density to the velocity is also the ratio of energy to momentum density. Therefore, the transition wave can be thought of as a localized quasi-particle with its energy scaling to its momentum density according to (3.21). Finally, note that we assumed linear damping and the existence of a traveling wave solution. Both assumptions may have to be relaxed depending on the specific features of the system of interest (see the discussion in subsequent sections).

3.3 Numerical simulations

For numerical purposes, dimensionless forms are obtained by normalization using the characteristic length $(\phi_0/k_0)^{1/2}$, time α/k_0, and force $(\phi_0 k_0)^{1/2}$, where we defined $\phi_0 = \Delta\phi/2$ and the initial stiffness of particle interactions, $k_0 = \phi''(0)/2$. By dividing (3.1) by the characteristic force and normalizing all variables, we arrive at

$$\begin{aligned} &\bar{m}\,\bar{u}_{n,\bar{t}\bar{t}} + \bar{\alpha}\,\bar{u}_{n,\bar{t}} + \bar{\phi}'(\bar{u}_n) \\ &- \sum_{j=1}^{N_b} \left[\bar{V}_j'\left(\frac{\bar{u}_{n+j} - \bar{u}_n}{j\bar{a}}\right) - \bar{V}_j'\left(\frac{\bar{u}_n - \bar{u}_{n-j}}{j\bar{a}}\right)\right] = 0, \end{aligned} \tag{3.22}$$

where the overbars represent normalized quantities and $\bar{m} = mk_0/\alpha^2$, $\bar{\alpha} = 1$. The choice of the normalization parameters implies that $\Delta\bar{\phi} = \Delta\phi/\phi_0 = 2$ and thus $\Delta\bar{\psi}/\bar{\gamma} = 2$. Therefore, the energy law reduces to

$$\bar{E}/\bar{v} = 1. \tag{3.23}$$

For convenience, we omit the overbars in the subsequent numerical examples.

To verify the theoretical predictions, simulations were performed on a periodic chain of 600 particles which are governed by a variety of interaction potentials V and multi-stable on-site potentials ψ. The lattice is initially unstretched and at rest and loaded by displacing the leftmost particle until it transitions from one stable potential well into another. The right-most particle is held fixed. The lattice response is computed by Newmark-β implicit time integration. After assuming a steady state, the velocity and energy of the wave remain constant over time, as shown in the example of Fig. 3.1.

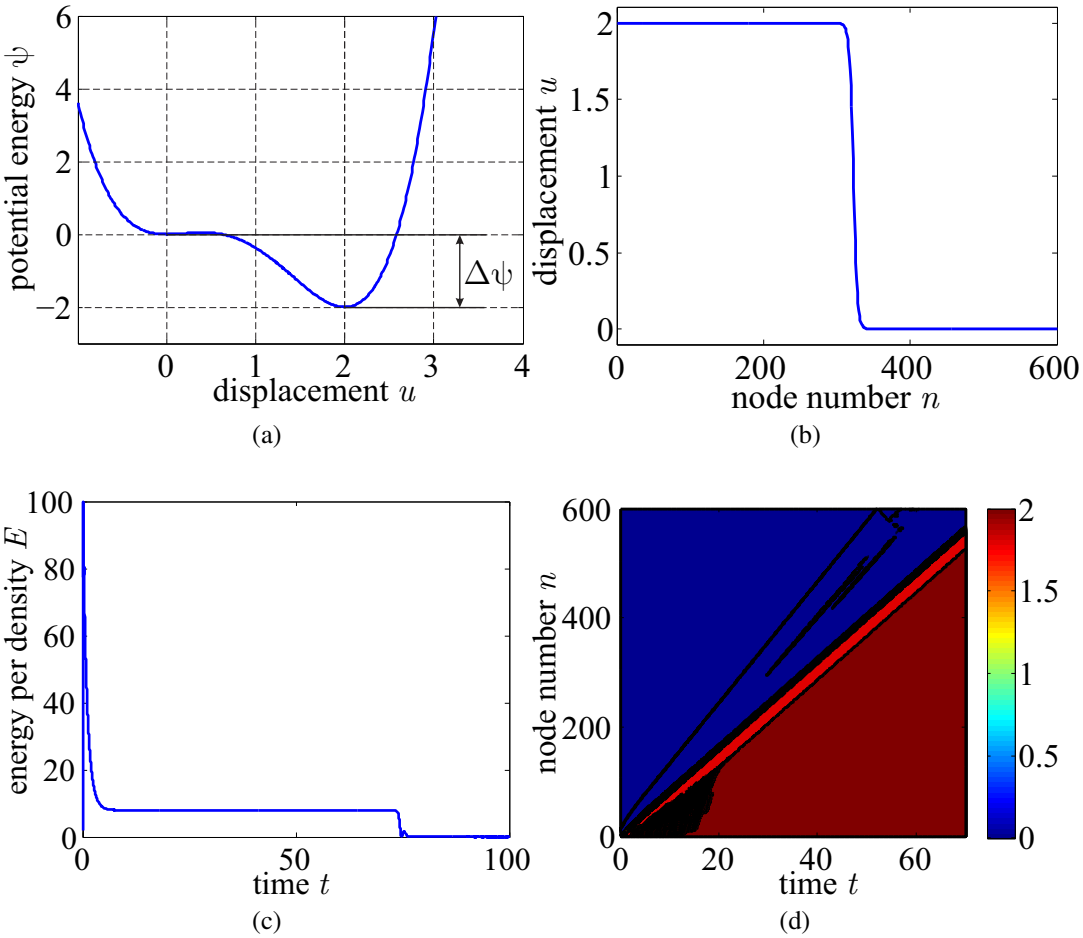

Figure 3.1: Example of a moving transition wave: (a) bistable topology of the on-site potential ψ with minima at $u = 0$ and $u = 2$; (b) resulting transition wave profile (displacement vs. position); (c) evolution of the kinetic energy per density vs. time (the kinetic energy stabilizes at a constant value once the kink assumes a steady waveform); (d) contour plot of the wave propagation in x-t-form. The phase boundary moves at a constant velocity once it assumes a steady kink waveform.

In particular, we simulated diffusive and dissipative chains of particles exposed to the same fourth-order polynomial bistable on-site potential of Fig. 3.1a with the following interaction potentials motivated by the introductory examples:

(i) Linear elastic springs as in the classical Frenkel-Kontorova model of dislocation motion [51]: $V'(u) = F_0 u/a$ (with $F_0 = 100$ and $a = 1$),

(ii) Coulombic interactions between charged particles [25]: $V'(u) = F_0(u/a + 1)^{-2}$ (with $F_0 = 0.0015625$ and $a = 8$),

(iii) Dipole-dipole interactions in a chain of magnets: $V'(u) = F_0(u/a + 1)^{-4}$ with ($F_0 = 0.016$ and $a = 5$),

(iv) Nonlinear Toda interactions describing, among others, charge density waves [56]: $V'(u) = F_0(1 - e^{-\beta u/a})$ (with $F_0 = 100$, $a = 6$ and $\beta = 6$),

(v) Hyperelastic rubber connectors (1D incompressible Neo-Hookean solid [107]): $V'(u) = F_0\left(1 + \frac{u}{a} - (u/a + 1)^{-2}\right)$ (with $F_0 = 1$ and $a = 6$), and

(vi) Lennard-Jones (LJ) atomic interactions with varying cut-off radius: $V'(u) = F_0\left[(1 + u/a)^{-7} - (1 + u/a)^{-13}\right]$ (with $F_0 = 137.17$ and $a = 3$).

Due to the short-range nature of LJ, we also computed results for long-range linear-spring interactions with up to $N_b = 4$ neighbors. The summary of results in Fig. 3.2 confirms that the scaling law is indeed independent of the interaction potential and of the number of neighboring interactions.

Surprisingly, the scaling law is independent of the topology of the non-convex potential ψ. For verification, simulations were carried out on lattices with the three bistable interaction potentials shown in Fig. 3.3; all are fourth-order polynomials with the same value of $\Delta\psi = 2$. In analogy to Fig. 3.2, Fig. 3.3b shows the linear relation between the computed kinetic energy of the traveling wave and the wave speed for all three bistable potentials, which confirms the energy transport law.

Since the energy law is linear, superposition can be expected in case of multi-well transitions despite the highly-nonlinear scenario. This suggests that a multi-well transition can be broken down into individual bi-stable transitions and analyzed separately to determine the total energy transported. To test this hypothesis, numerical experiments were performed for transitions occurring in a triple-well energy landscape as shown in Fig. 3.4. Results for three different interaction potentials are summarized in Table 3.1 and show excellent agreement with deviations of less than 1%, thus confirming that superposition applies indeed. However, as seen from Fig. 3.4b, in the special case $\Delta\psi_1 < 0$ and $\Delta\psi_1 + \Delta\psi_2 > 0$, the second transition drags the first along, causing both transitions to move at the same speed. Therefore, for multiple transitions, to preserve single-valuedness of the solution, we conclude that $v_k \geq v_{k+1}$, where v_k is the velocity of the k^{th} transition.

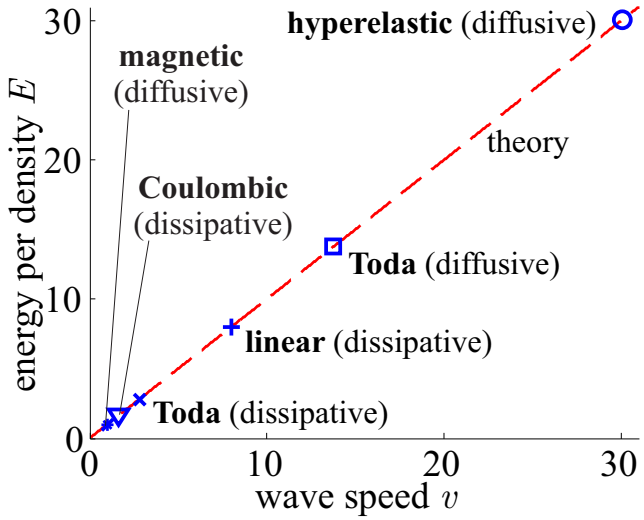

(a)

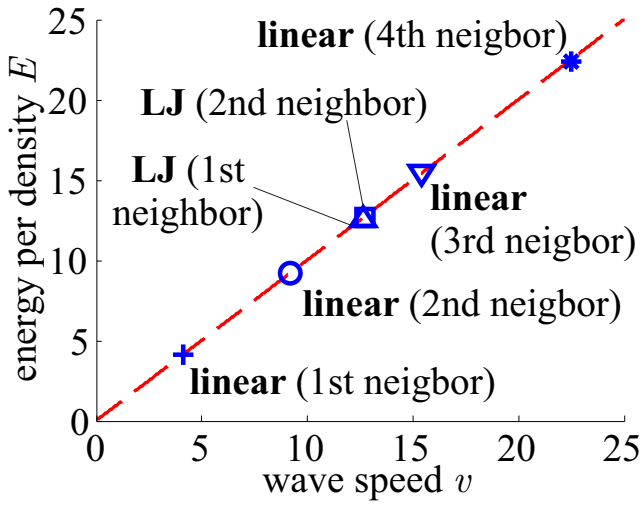

(b)

Figure 3.2: Plots of the kinetic energy E of the traveling wave vs. kink propagation speed v for (a) various examples of interaction potentials and (b) varying numbers of interacting neighbors. All examples use the bistable energy of Fig. 3.1a with $m = 1$ for dissipative and $m = 0.0001$ for weakly inertial or diffusive cases, and $a = 1$. All results lie almost perfectly on the predicted lines with slopes $E/v = \Delta\psi/2\gamma = 1$.

3.4 Discreteness effects

Discreteness effects become important in discrete systems when the width w of the transition wave is on the order of the lattice spacing (i.e., $w \sim a$). The continuum limit (3.14) of the discrete lattice model holds if the wave profile remains smooth. Smoothness is observed if dissipative effects dominate over inertial effects of the lattice ($\alpha^2 \gg mk_0$). However, in case of small dissipation and significant inertia ($mk_0 \gg \alpha^2$), the displacement profile displays rapid oscillations (twinkling

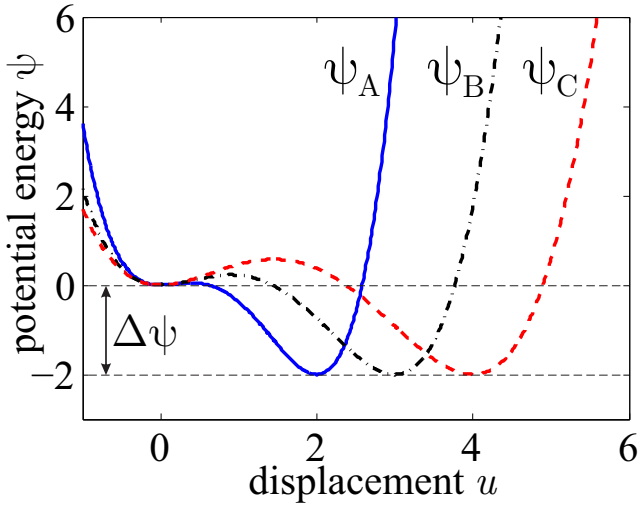

(a)

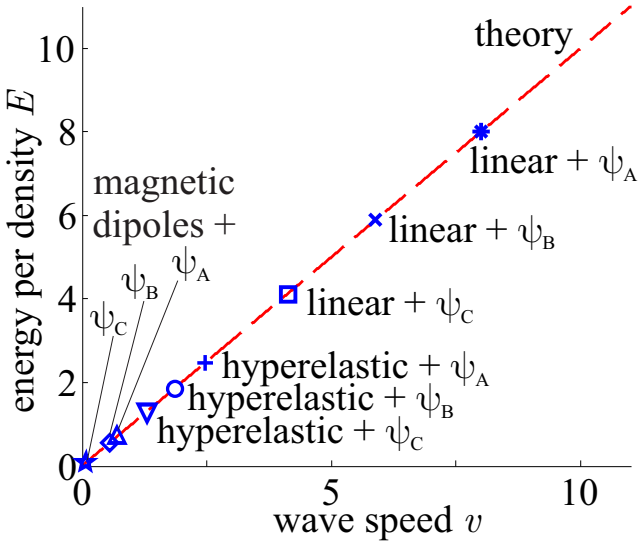

(b)

Figure 3.3: (a) Three different topologies of the on-site potential ψ with different equilibrium distances but with the same energy jump $\Delta\psi$; (b) resulting energy per density E vs. wave speed v for the different topologies and interaction potentials (all other parameters as in Fig. 3.2). Again, all computed values fall onto the predicted line with slope $E/v = \Delta\psi/2\gamma = 1$.

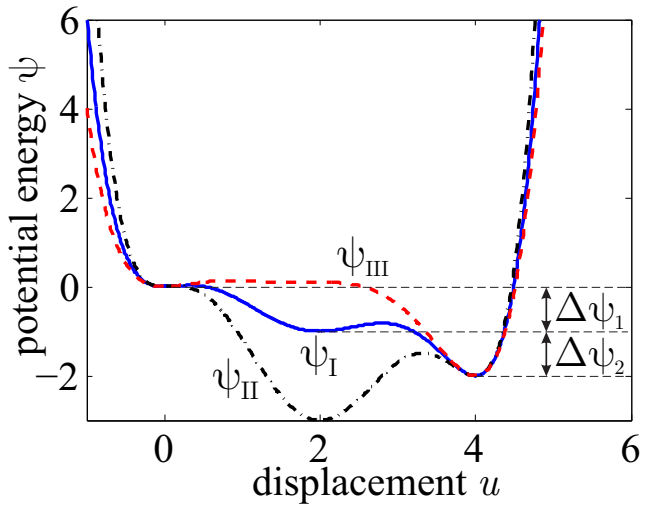

(a)

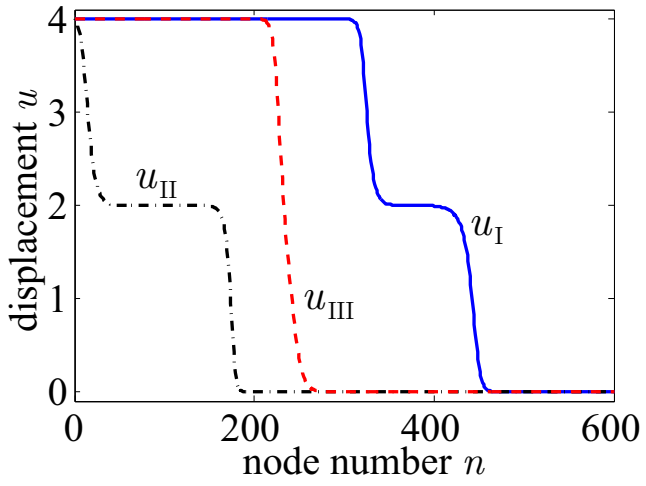

(b)

Figure 3.4: (a) The three possible topologies of a triple-well potential that generate propagating kinks: (I) $\Delta\psi_1, \Delta\psi_2 > 0$, (II) $\Delta\psi_1 > 0$, $\Delta\psi_2 < 0$, and (III) $\Delta\psi_1 < 0$, $\Delta\psi_1 + \Delta\psi_2 > 0$. (b) Resulting waveforms for the three cases: (I) two transition waves travel with different velocities, (II) only one partial transition wave propagates (the other is stationary as $\Delta\psi_2 < 0$), and (III) one complete transition wave propagates with a constant velocity (the second transition drags the first along).

modes) [9] in the wake of the traveling kink and the kinetic energy of the wave oscillates with a period $T = a/v$. An example of a weakly-dissipative discrete system is shown in Fig. 3.5. Here, the higher-order terms cannot be neglected when taking the continuum limit and hence the approximation in (3.9) fails to hold. In such cases, the energy law still applies if the energy E is replaced by its time average

$$\langle E \rangle = \frac{1}{T} \int_{t_0}^{t_0+T} E \, \mathrm{d}t' = v \int_{t_0}^{t_0+T} \sum_{i=1}^{N} \frac{1}{2} u_{i,t'}^2 \, \mathrm{d}t', \tag{3.24}$$

Interaction	$\Delta\psi_1$	$\Delta\psi_2$	v_1	v_2	$\frac{\Delta\psi_1 v_1+\Delta\psi_2 v_2}{2\gamma}$	E
Linear	0	2	4.5051	4.5051	4.5051	4.5029
	0.5	1.5	5.6130	5.6130	5.6130	5.6146
	1	1	7.2538	5.6741	6.4640	6.4114
	1.5	0.5	8.1123	3.1141	6.8628	6.8637
	2	0	8.5710	0.0307	8.5710	8.5760
Hyperelastic	0	2	1.4241	1.4240	1.4241	1.4231
	0.5	1.5	1.7733	1.7732	1.7732	1.7697
	1	1	2.2778	1.7762	2.0270	2.0089
	1.5	0.5	2.5308	0.9760	2.2421	2.1424
	2	0	2.6660	0.0132	2.6660	2.6670
Coulombic	0	2	0.9434	0.9434	0.9434	0.9429
	0.5	1.5	1.1476	1.1476	1.1476	1.1480
	1	1	1.4635	1.1492	1.3064	1.2964
	1.5	0.5	1.6398	0.6307	1.3875	1.3877
	2	0	1.7454	0.0000	1.7454	1.7464

Table 3.1: Numerical results for the sixth-order tri-stable potential energy with energy differences $\Delta\psi_1$ (first) and $\Delta\psi_2$ (second well). Wave speeds v_i (identified from contour plots by a linear regression fit) and total kinetic energies E are compared to the superposed theoretical predictions of the linear energy law (recall that travelling waves require $\Delta\psi_i > 0$).

where, $[t_0, t_0+T)$ represents one time period. The difference between the maximum energy level and the average energy is a measure of the kinetic energy barrier which is equivalent to the Peierls-Nabarro (PN) barrier that is created due to the discreteness of a lattice [96, 112]. As seen from Fig. 3.5, the energy oscillates about an average value as the wave travels through the lattice, and this average indeed equals the energy computed from the transport law (3.21).

3.5 Generalizations

3.5.1 Nonlinear damping

In case of nonlinear velocity-dependent on-site damping, the governing equation (3.1) changes into

$$\begin{aligned} &m\,u_{n,tt} + F(u_{n,t}) + \phi'(u_n) \\ &- \sum_{j=1}^{N_b} \left[V_j'\left(\frac{u_{n+j}-u_n}{ja}\right) - V_j'\left(\frac{u_n-u_{n-j}}{ja}\right)\right] = 0, \end{aligned} \tag{3.25}$$

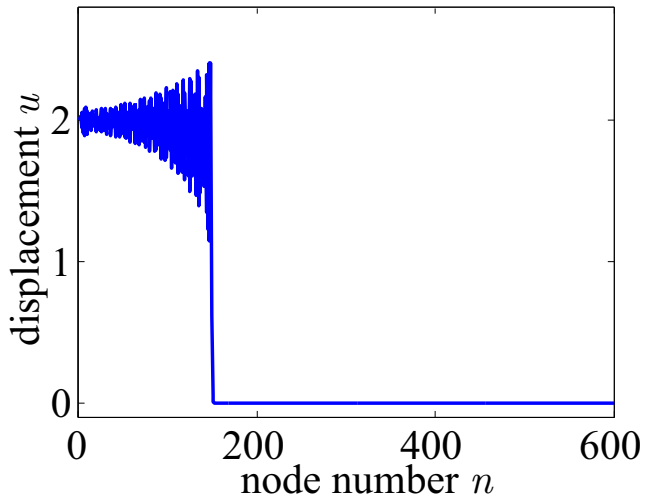

(a)

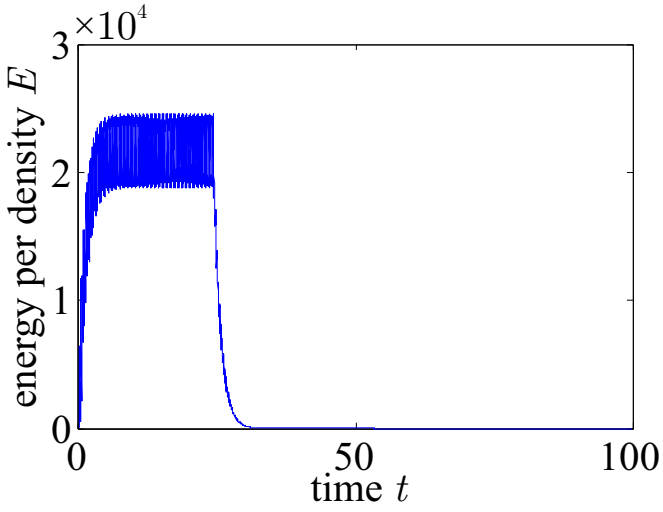

(b)

Figure 3.5: (a) Displacement profile and (b) kinetic energy when discreteness effects dominate and the wave profile is not smooth ($m = 1000$ with a hyperelastic interaction potential).

where $F(u_{n,t})$ is a generalized drag force. Following a similar procedure as that of Sec. 3.2.1 shows that

$$v\,\Delta\psi = -\frac{1}{a}\int_{-\infty}^{\infty} F(-vu_{,\xi})vu_{,\xi}\,\mathrm{d}\xi \simeq \sum_{n=1}^{N} F(u_{n,t})u_{n,t}. \tag{3.26}$$

The right-hand side represents the total power dissipated by the nonlinear damping and reduces to $2\gamma E$ in case of linear damping, i.e., for $F(u_{,t}) = \alpha u_{,t}$. As the second

law forces the dissipation to constantly drain energy from the system,

$$\sum_{n=1}^{N} F(u_{n,t})u_{n,t} \geq 0 \quad \Rightarrow \quad v\,\Delta\psi \geq 0. \tag{3.27}$$

The above result is analogous to the entropy condition in phase boundary propagation [3], where $\Delta\psi$ is the driving force on the phase front. Therefore, the above analysis may be interpreted as a derivation of the entropy condition for phase boundary propagation, in a general case. In the common case of linear damping, the power dissipated is proportional to the kinetic energy transported by the phase boundary. It is interesting to note that for linear on-site damping the dissipation removes only the contribution of the potential energy while preserving the kinetic energy.

3.5.2 Higher dimensions

Even though formulated in 1D, the above concepts also apply to general plane waves in higher dimensions. Consider, e.g., the time evolution the polarization vector $\boldsymbol{p}$, a diffusive phase-field variable, in ferroelectric ceramics. The potential energy density is commonly written as $W = \psi(\boldsymbol{p}) + \frac{\kappa}{2}|\boldsymbol{\nabla p}|^2$ with non-convex $\psi(\boldsymbol{p})$ and the nonlocal term representing energy stored in ferroelectric domain walls. One often derives the kinetics of domain switching from the gradient flow assumption [144, 170] with a drag coefficient γ, i.e.

$$\gamma\,\dot{\boldsymbol{p}} = -\frac{\delta W}{\delta \boldsymbol{p}} = -\frac{\partial \psi}{\partial \boldsymbol{p}} + \kappa\,\nabla^2 \boldsymbol{p}. \tag{3.28}$$

Ferroelectric switching is accommodated by the motion of planar domain walls which can be expressed as a plane wave $\boldsymbol{p}(\boldsymbol{x}, t) = \boldsymbol{p}(\boldsymbol{x}\cdot\boldsymbol{k} - vt) = \boldsymbol{p}(\xi)$, so that (3.28) becomes

$$-\kappa\,|\boldsymbol{k}|^2 p_{i,\xi\xi} - v\,\gamma\,p_{i,\xi} + \psi_{,i} = 0, \tag{3.29}$$

using indicial notation. Thus we recover the general form of governing equation (3.2). Multiplying by $p_{i,\xi}$ and integrating over time with $p_{i,\xi} = 0$ as $\xi \to \pm\infty$ yields

$$v\,\gamma \int_{-\infty}^{\infty} p_{i,\xi}\,p_{i,\xi}\,d\xi = \Delta\psi, \tag{3.30}$$

which leads to a restatement of the energy scaling law (3.21). Here, we observe that the speed of domain walls is related linearly to drag coefficient γ, the energy difference between the domains, and the shape of the domain wall (expressed by the above integral). This derivation also holds true if domain switching in a fully-electromechanically-coupled fashion is considered (with polarization $\boldsymbol{p}$, electric

field $\boldsymbol{e}$, and mechanical strain $\boldsymbol{\varepsilon}$ all represented as moving transition waves). A detailed derivation is shown in Chapter 6 as to how this theory can be used to calculate the velocity of domain walls. In summary, even though derived for 1D systems, the applicability of the energy scaling law is more general and applies to plane waves in both discrete and continuous systems.

3.6 Conclusions

We have derived an energy scaling law that applies to general nonlinear dissipative and diffusive lattices as well as to continuous systems, for arbitrary interaction potentials and non-convex on-site potentials. We have shown that dissipation or diffusion helps in stabilizing the waveform and get rid of small amplitude linear waves that can be seen in the conservative case depicted in Chapter 2. As a unique feature, linear superposition applies for multiple transitions even though the governing equations are highly nonlinear. Besides its surprising simplicity, the energy law is valuable to extract the speed, mobility, or transported energy of a transition wave from experimental data when only a subset of the latter is known. In the next chapter, we show an experimental system that shows an experimental demonstration of a discrete bistable lattice capable of showing a phase transition.

Chapter 4

UNIDIRECTIONAL TRANSITION WAVES IN DISCRETE BISTABLE LATTICES WITH NONLINEAR COUPLING

Research presented in this chapter has been adapted from the following publication:

Neel Nadkarni, Andres F. Arrieta, Christopher Chong, Dennis M. Kochmann, and Chiara Daraio. "Unidirectional Transition Waves in Bistable Lattices". In: *Physical Review Letters* 116.24 (June 2016), p. 244501. DOI: 10.1103/PhysRevLett.116.244501. URL: http://link.aps.org/doi/10.1103/PhysRevLett.116.244501.

We present a model system for strongly nonlinear transition waves generated in a periodic lattice of bistable members connected by magnetic links to study the kind of discrete dissipative phase transitions discussed in Chapter 3. The asymmetry of the on-site energy wells created by the bistable members produces a mechanical diode that supports only unidirectional transition wave propagation with constant wave velocity. We theoretically justify the cause of the unidirectionality of the transition wave and confirm these predictions by experiments and simulations. We further identify how the wave velocity and profile are uniquely linked to the double-well energy landscape, using the energy transport law as derived in Chapter 3.

4.1 Introduction

Unidirectional wave-guiding is a rare phenomenon of interest for mechanical diodes, rectifiers or switches that propagate stress waves in designated directions but not in reverse. For acoustic waves, this has been achieved through carefully engineered periodic lattices and topological metamaterials that exploit time-reversal asymmetry or transmission asymmetry, see e.g. [21, 70, 77, 81, 117, 126, 174]. Such systems, providing one-way acoustic insulation, are typically studied in the linearized regime and the associated elastic pressure waves display small amplitudes (and quickly decay in realistic structures with internal damping). In weakly-nonlinear lattices, directional wave-guiding has been achieved using cubic Kerr nonlinearities in non-homogeneous systems [129, 173]. However, strongly-nonlinear directional wave guides for the transmission of finite amplitude pulses or the mitigation of

impact shock waves have remained largely unexplored, partly due to their mathematical complexity and limited experimental realizations. Only one macroscopic experiment that has verified stable nonlinear transition waves in a chain of elastically-coupled rotational pendulums [130] as described in Chapter 1.1; and that system was bidirectional. Unfortunately, the lack of accessible experimental systems has left many previous theoretical studies unchallenged and, as a consequence, has rendered mechanical diodes in the nonlinear regime a rare find. In this chapter, we present an instructive homogeneous mechanical model that displays tunable unidirectional guiding of strongly-nonlinear transition waves and admits theoretical insight that agrees well with experimental findings.

We identify stable unidirectional transition wave propagation theoretically and experimentally in a 1D periodic lattice or "meta-structure" of bistable mechanical elements connected by nonlinear links. The double-well on-site potential is realized by pre-stressed composite shells which snap elastically from one stable equilibrium to another while undergoing large, nonlinear deformation. Magnetic inter-element connections generate nonlinear repulsive forces between bistable lattice members. As we demonstrate theoretically and verify numerically, the asymmetric potential energy wells make the wave propagation unidirectional: the transition from high to low energy produces a stable transition wave, whereas the reverse transition from low to high energy disintegrates incoming pressure waves, thereby acting as a diode for large-amplitude waves. This is in line with our theoretical observations in Chapter 3. This unidirectionality has potential for wave mitigation, impact energy absorption applications, or mechanical switches and filters. The described experimental setup serves as a model system that can enable the investigation of the rich nonlinear dynamics of periodic arrays with, in principle, arbitrary multi-stable on-site energy topologies.

4.2 Experimental system

The experimental setup consists of an array of bistable composite shells with an inter-element magnetic forcing. Individual bistable elements are made from carbon fiber reinforced plastic prepregs, laminated with a precise spatially distributed arrangement of laminae in the 0° and 90° directions. The combination of microstructure and cooldown after curing at elevated temperature induces a particular deformation field producing composite laminates exhibiting a tailorable strain potential topology, while admitting clamping of two opposite edges [6]. The dimensions for the elements used in the experiments are given in Table 4.1. Table 4.2 provides the

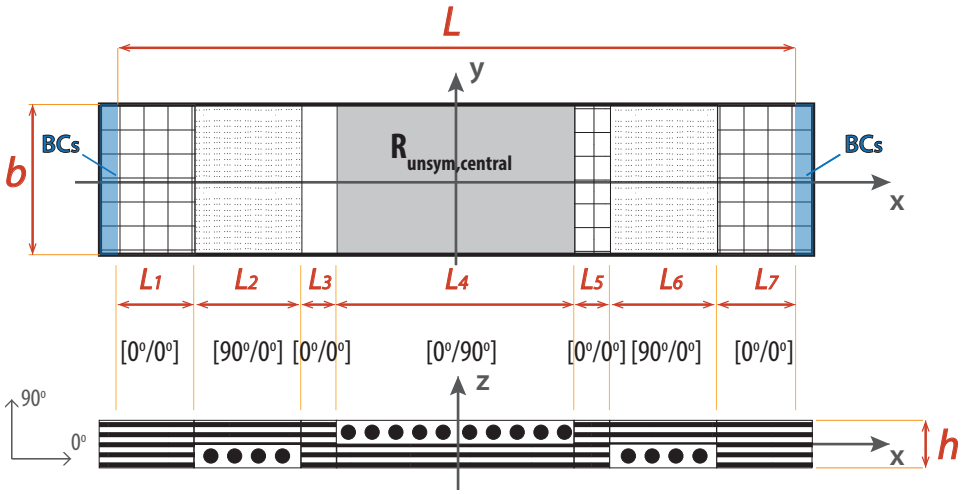

Figure 4.1: Tailored distribution of used bistable composite laminates.

material properties of the used c-m-p (CM-Preg T-C-120/625 CP002 35) prepreg system. The dimensions of the regions making up the fiber distribution of these laminates can provide a broad range of different potential wells and snapping forces.

The strain energy stored in the bistable laminate as a function of the out-of-plane displacement can be further tailored by varying the clamping distance, as well as the fiber distribution [71]. The topology of the resulting potential is designed to be inherently asymmetric with one of the wells having a lower energy than the other. To model the bistable element, the force-displacement curve is obtained with quasi-static displacement controlled tests which is fit with splines, see Fig. 4.2a. The magnitude of the snapping force is much higher at one transition point than the other. Furthermore, desired levels of force-displacement asymmetry and transition values can be designed by modifying the fiber distribution of the bistable members as required to control the characteristics of the propagating transition waves. The lattice used for experimentation consists of 20 bistable elements which are supported using clamps mounted on an aluminum rail. The rails are fixed to an optical

L [mm]	b [mm]	h [mm]	L_1 [mm]	L_2 [mm]	L_3 [mm]	L_4 [mm]	L_5 [mm]	L_6 [mm]	L_7 [mm]
220	64	0.25	31	15	5.0	120	5.0	15	31

Table 4.1: Geometric properties of the sections composing the spatially varying fiber for the bistable elements. Refer to for the schematic representation in Fig. 4.1 of the given parameters.

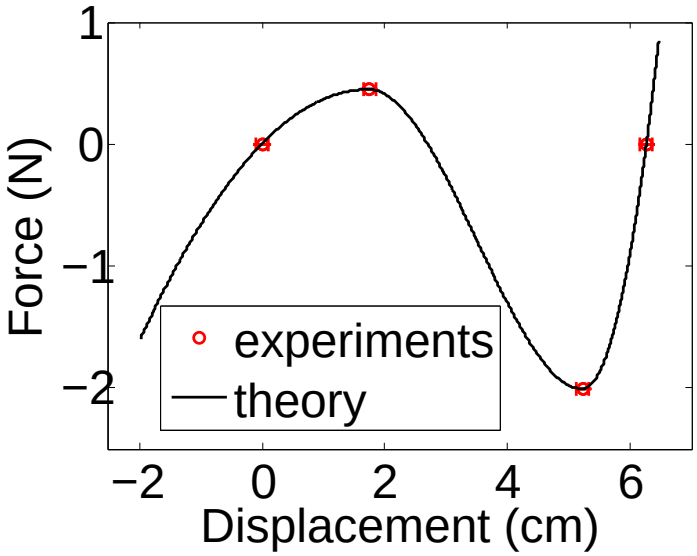

(a)

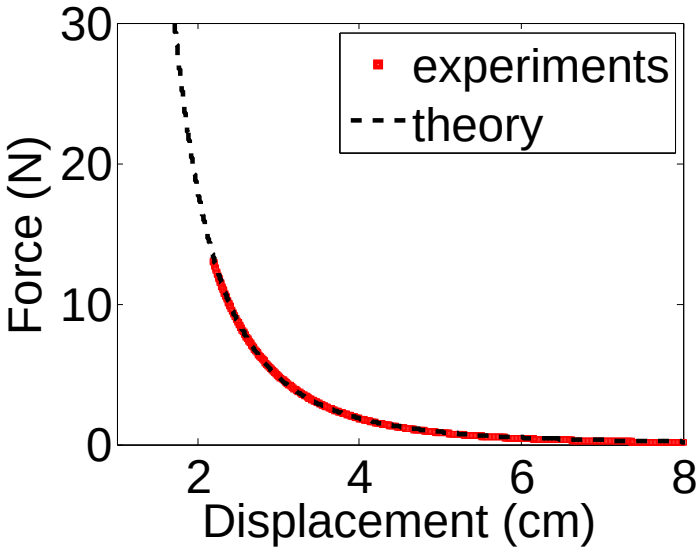

(b)

Figure 4.2: (a) Force displacement curve of the bistable element for clamping distance of 21.5 cm. The critical snapping points (maximum force) and equilibrium points are identified and fitted with splines while maintaining continuity in stiffness. (b) Magnetic force vs displacement plot for an NSNS-SNSN configuration. Numerical fit: $F = Ad^p$ with A = 4.95e-05 N/m^p and p = -3.274.

Material	Fibre vol. [%]	E_{11} [GPa]	E_{22} [GPa]	G_{12} [GPa]	ν_{12} [-]	ρ [$\frac{kg}{m^3}$]	α_{11} K^{-1}	α_{22}
CFRP	60	161	10	4.4	0.3	1570	-1.8E-8	2.25E-5

Table 4.2: Material properties for a typical ply of CFRP c-m-p (CM-Preg T-C-120/625 CP002 35) prepreg used to manufacture the bistable elementsly. Nominal prepreg thickness 0.125 mm.

table. Each bistable element is fitted on either face with two NdFeB ring magnets of the R-19-09-06 N type (mass of 10 g, inner diameter 9.5 mm, outer diameter 19.1 mm and thickness of 6.4 mm), supplied by Supermagnete. Similar to [95], the force-displacement curve of the magnets, shown in Fig. 4.2b, is fitted using a best-fit relation of the form: $F = Ad^p$, where F is the force and d is the displacement. The magnets are fixed to the bistable laminates and are arranged in a NSNS-SNSN configuration to exert repelling forces between the elements. They are laser aligned so that all lie along a straight line. A stereoscopic digital image correlation system from Correlated Solutions, with two Photron Ux100 cameras with a rate of 4000 fps, is used to acquire the displacements of four consecutive representative bistable elements. The initial displacement is triggered using a precision screw which provides a repeatable perturbation to the first lattice element. The lattice used for experimentation is shown in Fig. 4.3.

4.3 Stable wave propagation

We study the transition from the high energy well to the lower energy well. All the bistable elements in the system are placed in the high energy well and the first element is forced to snap to the lower energy state. The rail distance R is defined as the distance between the clamps at the two ends of the bistable element and the lattice distance L is the distance between two elements in the chain. We present results for three representative cases of stable wave propagation in Fig. 4.4 for various choices of R and L. Each experiment was repeated three times to obtain statistical variations. In general, the results obtained were highly repeatable. The deformation of the bistable element is 3D in nature; however, the out-of-plane displacement is significantly higher than the in-plane deformation, thereby causing the wave propagation to be quasi-1D, as can be observed in the snap-shot sequence of the propagating wave shown in Fig. 4.5. Experiments are compared with numerical

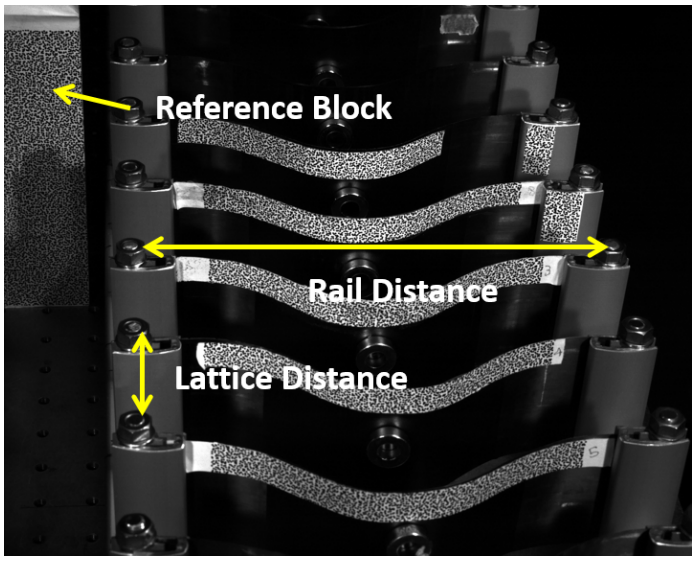

(a)

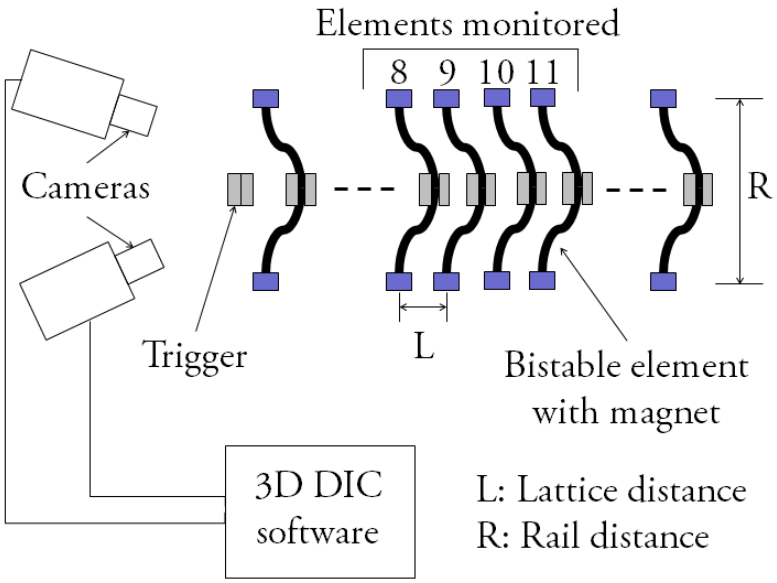

(b)

Figure 4.3: (a) The experimental lattice is shown along with the trigger magnet mounted on a precision screw. The displacements of elements 8 to 11 that are marked using a speckle pattern are tracked using a digital image correlation software (DIC). (b) A schematic of the experimental measurement technique is shown. The two cameras are synchronized and capture the 3D deformation field of the tracked specimens. The out-of-plane deformation is obtained using the Vic-3D DIC software.

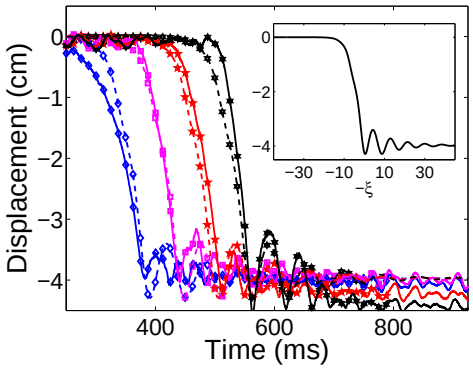

(a)

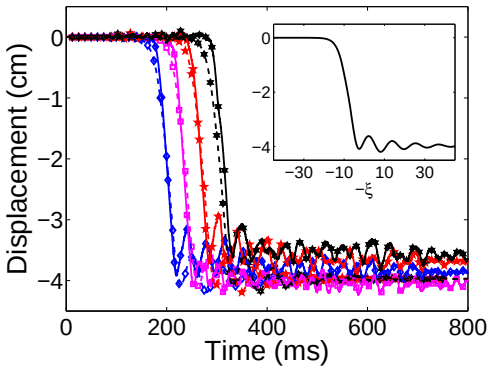

(b)

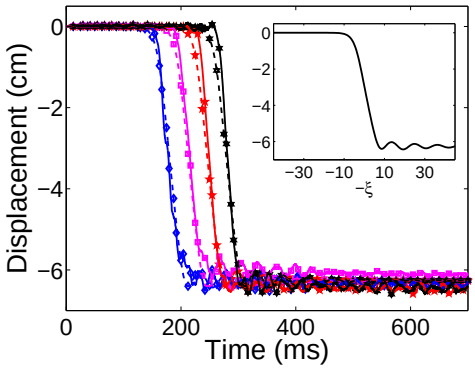

(c)

Figure 4.4: Transition wave propagation for three different combinations of lattice distance (L) and rail distance (R). The displacement time series is shown for the 8th - 11th element (blue diamonds, magenta squares, red 5 point stars and black 6 point starts respectively) for (a) L = 8 cm, R = 22.5 cm (b) L = 6 cm, R = 22 cm and (c) L = 8 cm, R = 21.5 cm. The negative values of the displacements indicate that the elements are deforming away from the camera. The direct numerical simulations of the discrete particle model Eq. (4.1) (dashed lines) are in good agreement with the experimental results (solid lines). The inset of each panel is the numerical solution of the exact transition wave. On reaching the boundary, the waves do not reflect back into the bulk and hence the transition is unidirectional.

simulations of the following 1D model of the discrete lattice:

$$\begin{aligned} mu_{n,tt} + A(u_{n+1} - u_n + L)^p - A(u_n - u_{n-1} + L)^p \\ + \alpha u_{n,t} + \phi'(u_n) = 0, \end{aligned} \tag{4.1}$$

where u_n is the displacement of the nth particle from its static equilibrium, A and $p < -1$ are parameters of the inter-element forcing function, m is the mass of the four magnets that compose each connecting element, L is the lattice distance, $\alpha > 0$ is the dissipation constant and $\phi(u)$ is a bistable potential. The parameters A, p and the bistable potential $\phi(u)$ are determined through the fitting procedure described above. Indices following a comma denote differentiation. The simulations are performed using a Newmark-β time integration scheme [106]. We expect the dissipation parameter to depend on the snapping trajectory of an individual bistable element, which is linked only to the rail distance. Therefore we assume α to be independent of the lattice distance and to only depend on the rail distance. For each rail distance R, the dissipation parameter α is calculated by matching the numerically obtained wave velocity with experiments for a fixed value of the lattice distance L. The snapping equilibrium distances for the used elements is slightly different ($\sim \pm 10\%$) owing to variability induced during the composite manufacturing process. Nevertheless, this variation does not affect the underlying physical behavior under examination. Comparing Figs. 4.4a and 4.4b, we see that the strain of the wave transition profile is broader for larger lattice spacings (Fig. 4.4a) and more spatially localized for small lattice spacings (Fig. 4.4b). The variation of wave localization (i.e. width of strain profile) and velocity as functions of lattice distance for different rail distances are shown in Fig. 4.6. The experimental result for $R = 21.5$ cm and $L = 6$ cm is an outlier in Fig. 4.6a. This is due to the fact that L (6 cm) is smaller than the snapping distance (~ 6.2 cm). This causes multiple intermediate snaps during the transition of the bistable element and the quasi-1D approximation fails to hold, thereby causing the experimental data to significantly deviate from the numerical results. The control parameters L and R allow for designing the level of wave localization as shown in Fig. 4.6b. Interestingly, in the proposed system, transition

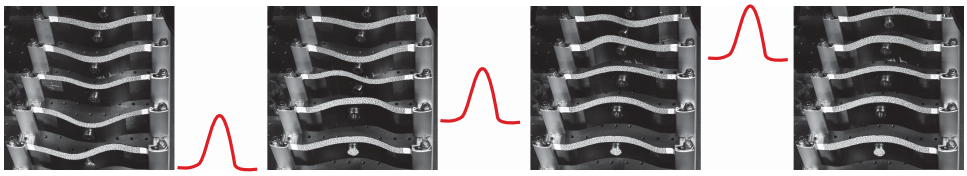

Figure 4.5: Snap-shot sequence showing the transition wave as it propagates through the experimental lattice. Images were acquired at 4000 fps.

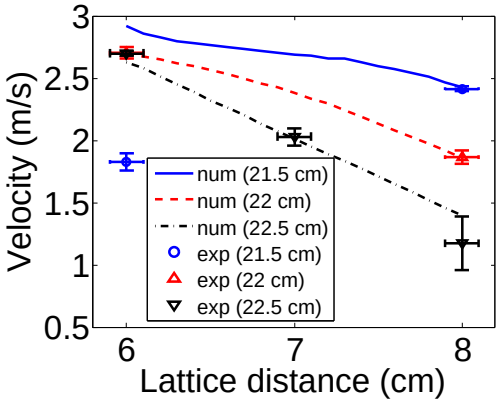

(a)

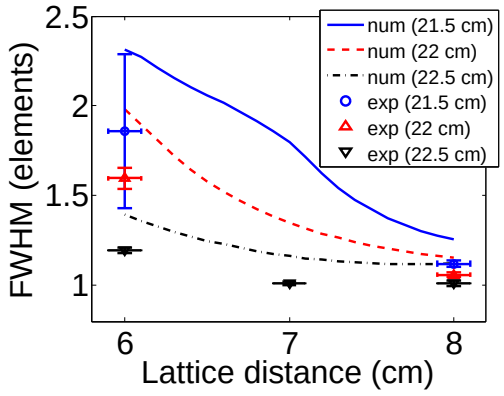

(b)

Figure 4.6: (a) Wave velocity as a function of lattice distance for different rail distances. The dissipation parameter has been optimized such that the wave velocity matches for lattice distance 8 cm for rail distances 21.5 cm and 22 cm, and lattice distance 7 cm for rail distance 22.5 cm. (b) Full width at half maximum (FWHM) of the strain profile of the transition wave as a function of lattice distance for different rail distances.

waves can be localized almost on a single element allowing for tightly packed and remarkably stable energy transmission. Hence, the waves can be localized to a single particle, similar to the case of repelling magnet chains [95]. This compares with a minimum of approximately 2.2 particles for pressure waves in granular chains [104, 105].

4.4 Numerical simulations for exact traveling waves

An interesting observation is that despite varying the initial guess, our algorithm converges to the same profile and wave velocity v, implying that for a fixed set of system parameters, there is a unique wave velocity of the transition wave. For

example, stronger initial impacts do not lead to faster waves, which is in contrast to the case of the granular chain [104]. Indeed, it appears the combination of an asymmetric bistable potential and the presence of damping leads to unique wave velocities, making this system more akin to reaction-diffusion type equations [163] rather than Hamiltonian lattices such as those of the the Klein-Gordon type [57, 175] (e.g. the Frenkel-Kontorova equation [51]) and Fermi-Pasta-Ulam type [52, 57] (e.g. the granular chain [104]). To probe this point even further, we restrict our attention to traveling wave solutions of the form of Eq. (4.1), namely those of the form $u_n(t) = u(Ln - vt) = u(\xi)$, where $u(\xi), \xi \in \mathbb{R}$ satisfies the advance-delay differential equation

$$\begin{aligned} v^2 m u_{\xi\xi} - v\alpha u_\xi + \beta\phi'(u) + A(u(\xi + L) - u(\xi) + L)^p \\ -A(u(\xi) - u(\xi - L) + L)^p = 0. \end{aligned} \tag{4.2}$$

Transition waves of Eq. (4.1) correspond to orbits of Eq. (4.2) that connect the equilibrium $u = u_i$ and $u = u_f$ where u_i and u_f are the positions of the potential wells of $\beta\phi$. Such special orbits of advance-delay equations, like Eq. (4.2), can be approximated numerically up to a prescribed tolerance [164]. In particular, one can make the discretization $u^j := u(j\Delta\xi)$ where $j \in \mathbb{Z}$ which, upon a choice of finite difference approximation of the derivatives, results in an algebraic equation that can be solved via Newton iterations:

$$\begin{aligned} v^2 m \frac{u^{j+1} - 2u^j + u^{j-1}}{\Delta\xi^2} - v\alpha \frac{u^{j+1} - u^{j-1}}{2\Delta\xi} + \beta\phi'(u^j) \\ +A(u^{j+q} - u^j + L)^p - A(u^j - u^{j-q} + L)^p = 0, \end{aligned} \tag{4.3}$$

where $\Delta\xi$ is chosen such that $q = L/\Delta\xi$ is an integer. We impose no-flux boundary conditions and let the wave velocity v be a variable of the system (rather than a fixed parameter). We find that, despite varying the initial guess for solving Eq. (4.2) numerically, our algorithm converges to the same profile and wave velocity v, implying that for a fixed set of system parameters, there is a unique wave velocity of the transition wave. The traveling wave formulation (4.2) is also natural for bifurcation and sensitivity studies. For example, the variation of the wave velocity with respect to the interaction potential coefficient p, and level of asymmetry are presented in the following section.

4.5 Robustness analysis

4.5.1 Sensitivity of wave velocity with respect to interaction coefficient

Fig. 4.7 shows the variation of the wave velocity for various coefficients of the interaction potential p. It can be seen that the velocity becomes zero beyond a

certain critical value of the parameter p. From a physical point of view, this is reasonable. The strength of inter-element forcing decreases with decreasing nonlinearity parameter p. When the initial element is snapped over, the small force due to magnetic coupling not sufficient for the subsequent element to snap over the on-site potential energy barrier, thereby causing the wave to stagnate. This is analogous to the propagation failure observed in discrete reaction-diffusion lattices [40]. The value of $p = -3.274$ in the experiments lies well above the critical range for each of the parameter values shown in Fig. 4.7. For a fixed lattice distance, the potential barrier decreases as the rail distance increases. Therefore, it is not surprising that the critical value of the nonlinearity p at which the wave stoppage occurs decreases as the rail distance increases, see Fig. 4.7a. For a constant rail distance, as the lattice distance increases, the interaction force between magnets in the undeformed state decreases (since the distance between the magnets that couple the elements is increasing). Hence, the nonlinearity p at which the wave stops propagating increases as the lattice distance increases, see Fig. 4.7b.

4.5.2 Sensitivity of wave velocity with respect to asymmetry of the on-site bistable potential

To obtain a theoretical approximation of the onsite potential $\psi(u)$ for the snapping elements, the experimentally measured values of the distance and corresponding force were fit by a polynomial spline (see Fig. 4.2). To investigate the role of the asymmetry numerically we introduce an asymmetry parameter ϵ where $\epsilon = 0$ corresponds to the asymmetry of the experimentally measured on-site potential, and $\epsilon = 1$ corresponds to a symmetric potential (see Fig. 4.8a and text below for details). As an example, we consider a rail distance of $R = 22.5$ cm and a lattice spacing of $L = 8$ cm. We performed a parametric continuation of roots of (4.1) with respect to the asymmetry parameter ϵ. The corresponding value of the wave speed v is plotted against the asymmetry parameter ϵ in Fig. 4.8b. Note the wave speed decreases as the asymmetry weakens.

4.5.3 Determination of the asymmetry parameter ϵ

Let the experimentally measured local minimum be (u_1, F_1), the local maximum be (u_2, F_2), and the largest root be $(u_3, 0)$, where the first entry of each of these coordinate pairs is the displacement and the second entry is the force (see red markers of Fig. 4.8a). To explore how the degree of asymmetry affects wave propagation, we modified the values of x_3 and (x_2, y_2) gradually until a symmetric function

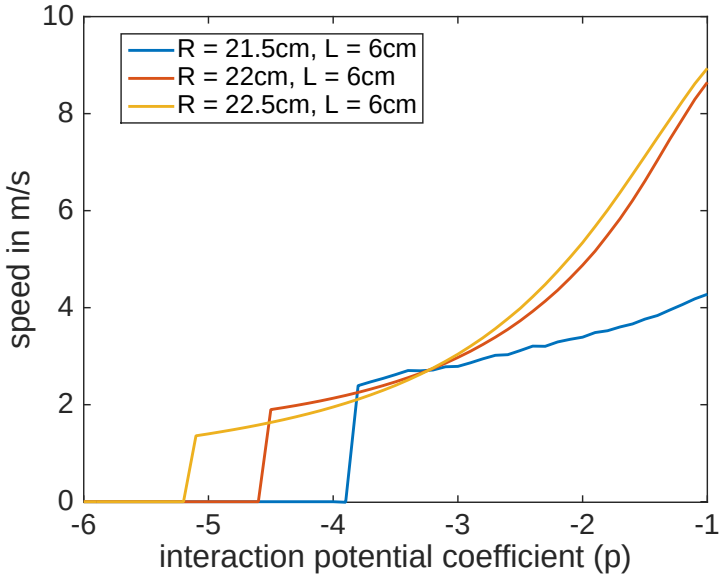

(a)

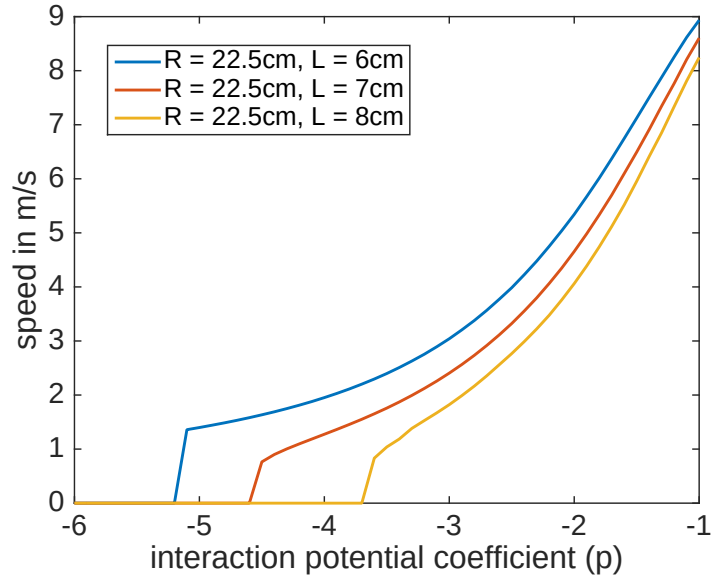

(b)

Figure 4.7: (a) Variation of wave velocity with interaction coefficient p for different rail distances while keeping the lattice distance constant. (b) Variation of wave velocity with interaction coefficient p for different lattice distances while keeping the rail distance constant.

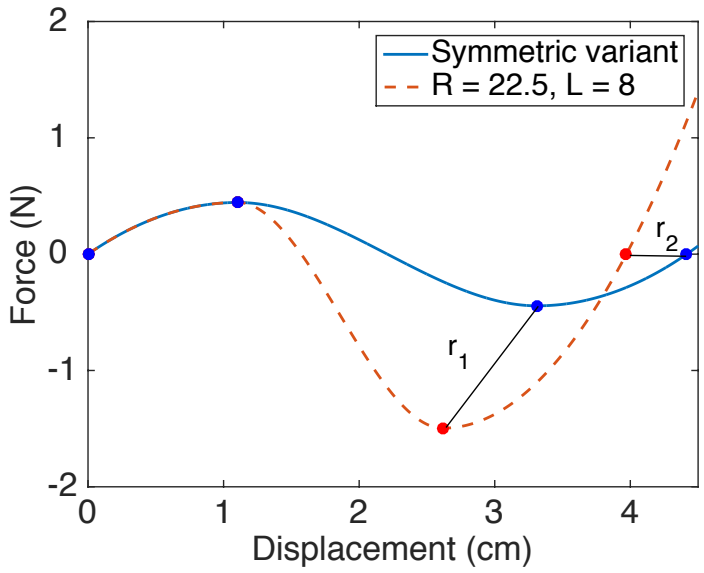

(a)

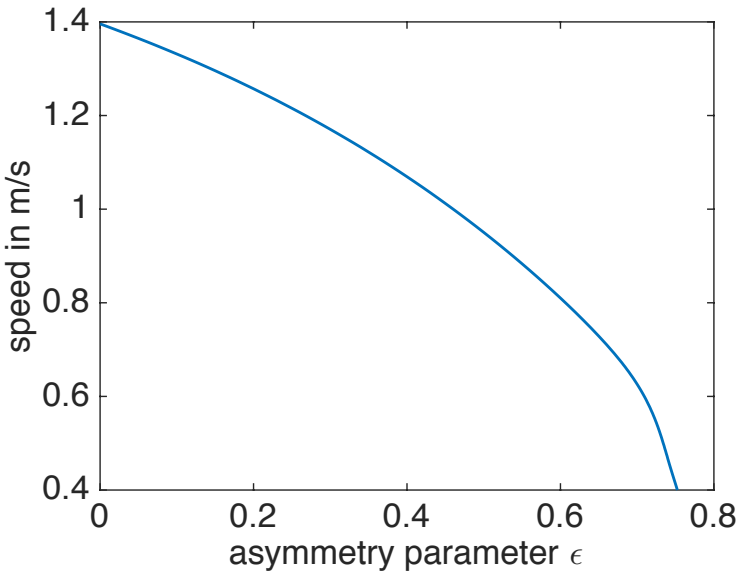

(b)

Figure 4.8: (a) Fitted onsite force for the case of $R = 22.5$ cm and $L = 8$ cm (dashed red line) and experimentally measured values (red markers). The symmetric counterpart of this function is also shown (blue solid line), which was obtained by modifying the local minimum and largest root along the lines r_1 and r_2 respectively. The fraction of the distance moved along these lines is the asymmetry parameter ϵ. (b) Plot of the wave speed as the asymmetry parameter ϵ is varied.

was obtained (see blue curve of Fig. 4.8a). The symmetric function of interest corresponds to the spline passing through the points $(0,0)$, (u_1, F_1), $(3u_1, -F_1)$ and $(4u_1, 0)$ (the spline was determined with the same procedure used to obtain the solid line of Fig. 4.2a). Let $r_1 = \sqrt{(u_2 - 3u_1)^2 + (F_2 + F_1)^2}$ be the distance between the experimentally measured local minimum (u_2, F_2) and the value $(3u_1, -F_1)$. Let $r_2 = \sqrt{(u_3 - 4u_1)^2}$ be the distance between the experimentally measured point $(u_3, 0)$ and the value $4u_1$. We then introduce an asymmetry parameter ϵ where $\epsilon = 0$ corresponds to the asymmetry of the experimentally measured onsite-potential and $\epsilon = 1$ corresponds to a symmetric potential. In particular we modify the values (u_2, F_2) and u_3 such that the distances r_1 and r_2 change like $r_1 \to r_1 - \epsilon r_1$ and $r_2 \to r_2 - \epsilon r_2$ for various values of $\epsilon \in [0, 1]$.

4.6 Wave disintegration

It can be shown that for a discrete system of this kind, stable wave propagation can occur if [98]

$$\psi(u_i) - \psi(u_f) = v\gamma \int_{-\infty}^{\infty} u_\xi^2 \, d\xi \geq 0 \Rightarrow \psi(u_i) \geq \psi(u_f). \tag{4.4}$$

Eq. (4.4) shows that the final state cannot have a higher energy than the initial state for stable wave propagation. This is because, in the case of high-to-low energy transition, the release of stored potential energy counters the effect of dissipation. This is not possible for a low-to-high energy transition. Therefore, in the case of an asymmetric bistable potential, a transition is allowed from the higher energy state to a lower energy state, as seen in the previous experiments; however in the opposite case, the wave does not propagate. The problem can also be approached through the entropy relation for phase boundary propagation [3]. Identifying that $\Delta\psi = \psi(u(\xi \to \infty)) - \psi(u(\xi \to -\infty))$ is the driving force on the transition wave, (4.4) can be rewritten as the entropy inequality,

$$v\Delta\psi \geq 0, \tag{4.5}$$

similar to the case of a martensitic phase transformation written in Chapter 1. Hence, the entropy inequality implicitly gives rise to the condition for unidirectional stable wave propagation in the discrete lattice. We observe this phenomenon in experiments. When all the elements are placed in the low energy well and a transition is forced, the elements snap back to their original low energy state. Therefore, the lattice works as a nonlinear unidirectional waveguide for transition waves.

4.7 Theoretical estimates of wave characteristics

Advance-delay differential equations such as Eq. (4.2) are notoriously difficult to analyze. One can obtain a system that is analytically tractable by considering a Taylor series approximation. In the case of Eq. (4.1), this results in the fourth order ordinary differential equation (ignoring higher order terms),

$$\begin{aligned} &-\tfrac{1}{24}L^2\rho c_0^2[(p-2)(p-1)u_{\xi\xi}^3(u_\xi+1)^{p-3} \\ &+4(p-1)u_{\xi\xi}u_{\xi\xi\xi}(u_\xi+1)^{p-2}+2u_{\xi\xi\xi\xi}(u_\xi+1)^{p-1}] \\ &\rho v^2 u_{\xi\xi}-\rho c_0^2\,u_{\xi\xi}(1+u_\xi)^{p-1}-v\gamma u_\xi+\psi'(u)=0, \end{aligned} \tag{4.6}$$

with $\xi = nL - vt$, $\rho = m/L$, $\rho c_0^2 = -AL^p p$, $\gamma = \alpha/L$, $\beta\phi'(u_n)/L = \psi'(u_n)$ and the subscript ξ implies differentiation. The governing equation (4.6) provides bounds for maximum particle velocity. When the particle velocity $u_t = -vu_\xi$ attains a maximum, the acceleration $u_{tt} = v^2 u_{\xi\xi} = 0$ is zero. Substituting this in (4.6) gives

$$|\tfrac{1}{12}a^2c_0^2u^*_{\xi\xi\xi\xi}(-A/v+1)^{p-1}| = |-\gamma A+\psi'(u^*)|, \tag{4.7}$$

where the asterisk indicates evaluation where u_ξ is at a maximum. In the continuum limit ($L \to 0$), the term on the left hand side in (4.7) is negligible. Therefore,

$$A \simeq \psi'(u^*)/\gamma \le F_m/\gamma \tag{4.8}$$

where F_m is the maximum force or the snapping force of the bistable element and u^* is the displacement at maximum u_ξ, thus providing an upper bound estimate of the maximum particle velocity. The width of the strain profile of the transition wave can be estimated by assuming an ansatz of the form

$$u_\xi(\xi) = \frac{A}{v}\,\mathrm{sech}^2\frac{1.76\,\xi}{w} \tag{4.9}$$

where w is the full width at half-maximum (FHWM). Substituting (4.9) in (4.4) and evaluating the integral yields

$$w = 1.32\,\frac{v\Delta\psi}{A^2\gamma} \ge 1.32\,\frac{\gamma v\Delta\psi}{F_m^2}, \tag{4.10}$$

thus providing a lower bound on the width of the wave (or the amount of localization that can be achieved). Finally, the kinetic energy transported by the wave oscillates about a mean value, as seen in Fig. 4.9. It can be shown using (4.4), that the average kinetic energy transported ($\langle E\rangle$) can be computed as

$$\langle E\rangle = \frac{\Delta\psi}{2\gamma}\rho v \tag{4.11}$$

(with $\rho = m/L$) which scales linearly with the velocity of wave propagation [98] and the oscillation frequency is $f = v/L$.

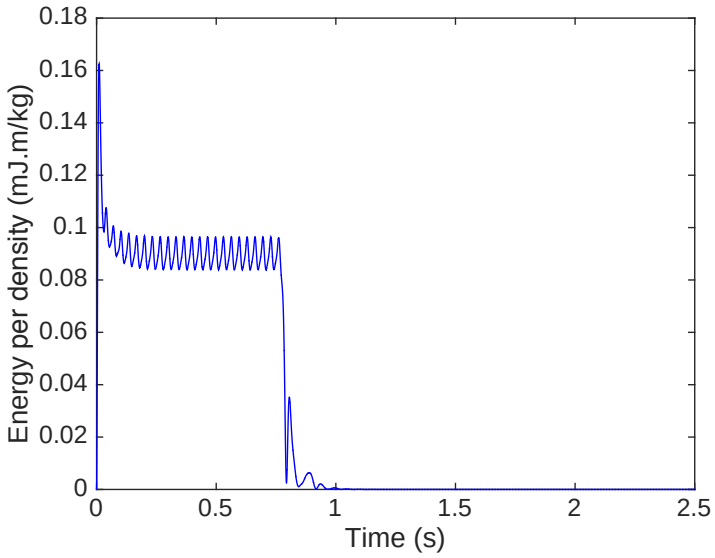

Figure 4.9: Energy profile of a simulation for R=21.5 cm and L=8 cm. The energy drops to zero when the wave reaches the end of the lattice.

4.8 Conclusions

We have introduced a model lattice system comprised of tailored bistable elements connected by magnets sustaining strongly nonlinear unidirectional propagation of transition pressure waves. A reduced 1D discrete analytical model is developed which allows for wave tailoring, by designing the strain potential topology of the bistable members, the direction of propagation, velocity and profile of the transition waves. The designed on-site potential exhibited by the bistable members enables the realization of mechanical diodes and wave guides with far-reaching applications, from energy absorption and harvesting, to impact mitigation and imaging. In addition, our model system allows for accessible experimental investigation of hitherto difficult to access transition wave phenomena in solids.

Chapter 5

STABLE MECHANICAL SIGNAL PROPAGATION THROUGH DISSIPATIVE MEDIA: AN APPLICATION IN STRUCTURAL DYNAMICS

Research presented in this chapter has been adapted from the following publication:

Jordan R. Raney, Neel Nadkarni, Chiara Daraio, Dennis M. Kochmann, Jennifer A. Lewis, and Katia Bertoldi. "Stable propagation of mechanical signals in soft media using stored elastic energy". en. In: *Proceedings of the National Academy of Sciences* 113.35 (Aug. 2016), pp. 9722–9727. ISSN: 0027-8424, 1091-6490. DOI: 10.1073/pnas.1604838113. URL: http://www.pnas.org/content/113/35/9722.

Soft structures with rationally designed architectures capable of large, nonlinear deformation present opportunities for unprecedented, highly-tunable devices and machines. However, the highly-dissipative nature of soft materials intrinsically limits or prevents certain functions, such as the propagation of mechanical signals. In Chapter 3, we showed that the dissipation stabilizes the nonlinear transition wave instead of hampering its propagation. In this chapter, we use this feature to design structures from soft materials that have high inherent damping to propagate mechanical signals over large distances where linear waves are damped out. In particular, we present an architected soft system comprised of elastomeric bistable beam elements connected by elastomeric linear springs. The dissipative nature of the polymer readily damps linear waves, preventing propagation of any mechanical signal beyond a short distance, as expected. However, the unique architecture of the system enables propagation of stable, nonlinear solitary transition waves with constant, controllable velocity and pulse geometry over arbitrary distances. Since the high damping of the material removes all other linear, small amplitude excitations, the desired pulse propagates with high fidelity and controllability. This phenomenon can be used to control signals, as demonstrated by the design of soft mechanical diodes and logic gates. The experiments were performed by our collaborator Jordan R. Raney in the laboratories of Prof. Katia Bertoldi and Prof. Jennifer A. Lewis at Harvard University, while the numerical simulations were performed by the author

of this thesis.

5.1 Introduction

Soft, highly deformable materials have enabled the design of new classes of tunable and responsive systems and devices, including bioinspired soft robots [135, 165], self-regulating microfluidics [39], adaptive optics [29], reusable energy-absorbing systems [123, 133], structures with highly programmable responses [46], and new morphological computing paradigms [101]. However, their highly deformable and dissipative nature also poses unique challenges. While it has been demonstrated that the nonlinear response of soft structures can be exploited to design machines capable of performing surprisingly sophisticated functions on actuation [109, 135, 165], their high intrinsic dissipation has prevented the design of completely soft machines. Sensing and control functionalities, which require transmission of a signal over a distance, still typically rely on the integration of stiff electronic components within the soft material [88, 149], introducing interfaces that are often a source of mechanical failure.

The design of soft control and sensing systems (and, consequently, completely soft machines) requires the ability to propagate a stable signal without distortion through soft media. There are two limiting factors intrinsic to materials that work against this: dispersion (signal distortion due to frequency-dependent phase velocity) and dissipation (loss of energy over time as the wave propagates through the medium). Dispersion can be controlled or eliminated through nonlinear effects produced via the control of structure in the medium [104]. For example, periodic systems based on Hertzian contact [21, 105, 142], tensegrity structures [50], rigid bars and linkages [30], and bistable elastic elements [97] can behave as non-dispersive media, with the nonlinearity of their local mechanical response canceling out the tendency for the signal to disperse at sufficiently large amplitudes. However, dissipation is still an overarching problem. Structures designed to propagate elastic waves are typically built from stiff materials with low intrinsic dissipation (e.g., metals) and excited with small amplitude excitation (to avoid plastic energy loss). This approach minimizes, but does not eliminate, dissipation. In soft, highly dissipative media, the problem is further exacerbated and there is no robust strategy currently available to propagate signals in these systems.

Here, we report an architected medium made of a highly dissipative, soft material that overcomes both dispersive and dissipative effects and enables the propagation of

a mechanical signal over arbitrary distances without distortion. A stable mechanical signal can be transmitted over long distances through a dissipative medium only if additional energy is continuously supplied during its propagation. To achieve such behavior, we use bistable elastomeric beams that are capable of storing elastic energy in the form of deformation and then, stimulated by the wavefront, releasing it during the propagation of the wave, without the need of any external stimulus. Importantly, dissipation allows stable wave propagation by balancing the elastic energy release. The damping intrinsic to the soft materials removes all signals except the desired transition wave, which therefore propagates with high fidelity, predictability, and controllability. The proposed architecture is capable of propagating stable waves with constant velocity over arbitrary distances, overcoming both dissipative and dispersive effects, despite the soft, dissipative material of which it is composed. Together, these effects enable the design of a new class of functional devices, such as soft mechanical logic elements. The ability to 3D print soft mechanical logic enables a new degree of customizability and tunability relative to previous examples of mechanical logic [21, 36, 76, 81].

5.2 System architecture and fabrication

The fundamental building block of our system is a bistable element (formed by two tilted beams) connected to a horizontal element with linear response, all made of elastomeric material (Fig. 5.1A). The tilted beams have aspect ratio $L/t = 18$ (with $L = 7$ mm), while their inclination angle is determined by their end-to-end distance d. The horizontal coupling elements are designed to have a linear mechanical response (Fig. 5.1B), with their morphology selected to achieve a range of effective stiffnesses (an important parameter for determining the dynamic behavior of the system). Systems comprising up to 100 building blocks arranged to form a one dimensional chain (see Fig. 5.1A) are fabricated with high fidelity using direct ink writing, an extrusion-based 3D printing method [75]. A viscoelastic polydimethylsiloxane (PDMS) ink was used for 3D printing. This consisted of a shear-thinning PDMS material, Dow Corning SE-1700 (85 wt.%), with a lower viscosity PDMS additive, Dow Corning Sylgard 184 (15 wt.%). The viscoelastic yield properties are tailored (see supporting information of Ref. [133] for rheological characterization) to ensure that the uncured ink both flows readily during printing, yet maintains its shape until it is permanently cross-linked in a subsequent curing step (100°C for 30 min). This material was extruded through a tapered nozzle (200 μm inner diameter tapered nozzle from Nordson EFD) during programmed

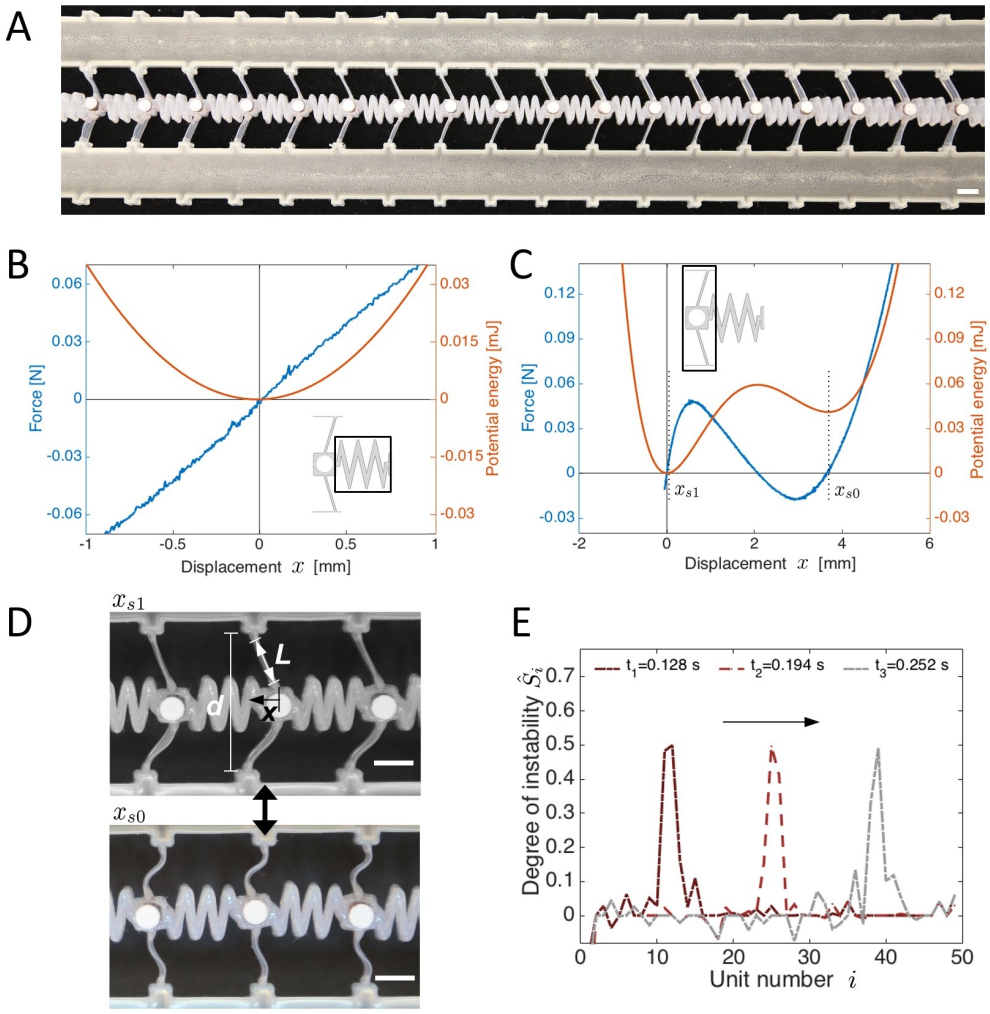

Figure 5.1: (A) The system consists of a 1D series of bistable elements connected by soft coupling elements (scale bar represents 5 mm); (B) the coupling elements are designed to exhibit a linear mechanical response, while (C-D), the bistable elements possess two stable states (scale bars represent 5 mm); the bistability originates from lateral constraint (d) on a beam pair that is displaced (x) perpendicularly to the constraint; the mechanical response is fully determined by the aspect ratio (L divided by the thickness of the beam) and d; the two stable configurations of the bistable element correspond to the displacements $x = x_{s1} = 0$ and $x = x_{s0}$; (E) in certain cases a stable nonlinear transition wave propagates through the system (with each bistable element undergoing a displacement from $x = x_{s0}$ to $x = x_{s1}$); the instability ($\hat{S}_i$) propagates with constant velocity and geometry, enabled by both (i) the balance of nonlinear and dispersive effects and (ii) the balance of dissipation and energy release; here, we show snapshots of the evolving state of the chain, with $t_1 = 0.128$ s, $t_2 = 0.194$ s, and $t_3 = 0.252$ s relative to the start of the experiment, in this case with $d = 18.6$ mm.

translation of the nozzle over a fixed substrate (PTFE-coated aluminum). Ink extrusion was controlled via fixed pressure (Nordson EFD Ultimus V pressure box), with the nozzle precisely positioned using a custom 3D positioning stage (Aerotech). After printing and curing of the PDMS ink, two regions parallel with and adjacent to the functional region of wave propagation are infilled with epoxy (Momentive Epon 828) to prevent undesired structural bending that would make measuring the response of the system difficult. The lateral distance between these rigid supports, d, is defined by acrylic braces of precise dimensions, that were made using an Epilog Laser Mini cutting system. The acrylic braces also serve to elevate the soft structure (via the epoxy supports) without contacting it, to eliminate any interactions between the wave pulse and the table surface. A cylindrical copper rod (3.175 mm diameter) was cut to pieces of 5.17 mm length (giving a mass of approximately 0.47 g), which were press fit into the printed structure to enable optical tracking of periodic points along the structure. The top surfaces of these copper cylinders were painted with flat white paint to produce excellent light contrast for visualization of the transition wave propagation.

We characterize the static response of both the bistable elements and the connecting horizontal elements. A commercial quasistatic test system, Instron 5566, in displacement control at a displacement rate of 2 mm/min was used for measuring the force-displacement response. The force-displacement curve shown in Fig. 5.1B shows the linear response of the horizontal elements. In particular, for the element shown in Fig. 5.1A, with a zig-zag morphology of length 10 mm, width 5 mm, and thickness 5.4 mm, we measure a stiffness $k = dF/dx = 80$ N/m. Note that the value of k can be significantly altered (from 30 N/m to 2100 N/m) by choosing different connector geometries or different extrusion rates during printing as seen in Fig. 5.2. In contrast with the linear response of the connecting elements, the bistable elements, each comprised of two tilted beams, are characterized by a highly nonlinear response with a regime of negative incremental stiffness (see the region with negative slope in Fig. 5.1C). The associated instability leads to a rapid shape change that has been studied in the context of both natural [47] and synthetic systems [14, 43, 110, 147]. The associated potential energy, $V(x)$ (defined such that $\partial V/\partial x = -F$, and calculated by first fitting a fifth degree polynomial to the measured force-displacement data and then integrating), is characterized by two local minima at $x = x_{s1} = 0$ and $x = x_{s0}$ (see Fig. 5.1C), corresponding to the two stable states shown in Fig. 5.1D. Importantly, the stable configuration at x_{s0} is characterized by an energy state higher than that of the undeformed one (at $x_{s1} = 0$).

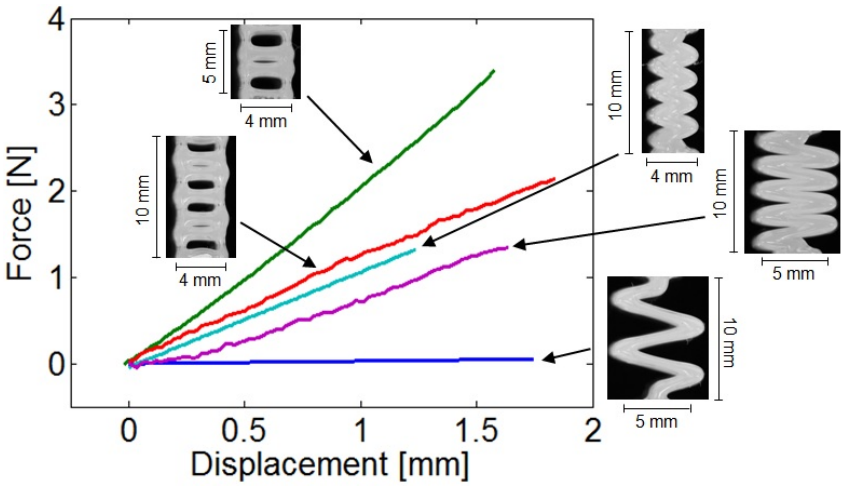

Figure 5.2: Using different geometries for the linear coupling elements leads to very different effective spring stiffnesses, which greatly affects the width and velocity of the propagating pulse. The stiffnesses were measured using an Instron 5566 in displacement control with a rate of 2 mm/min. The measured stiffnesses of the linear elements shown here were measured to vary from 30 N/m to 2100 N/m.

Therefore, similar to a phase transition, the transition between the two stable states involves a net change in stored potential energy, which, depending on the direction of the transition, either absorbs energy [133] or releases stored potential energy. Here we demonstrate that the release of energy associated with this transition can be exploited to overcome dissipation and to propagate a mechanical signal over arbitrary distances, enabling the design of a new class of soft and highly tunable devices, such as the mechanical logic elements demonstrated later.

5.3 Experimental results

5.3.1 Small amplitude excitation

To characterize the dynamic response of the system, we first consider small-amplitude excitations with white noise up to 5 kHz generated by an electrodynamic shaker (model K2025E013, Modal Shop) directly connected to one end of the sample. We monitor the propagation of the mechanical signal using two miniature accelerometers (352C22, PCB Piezotronics) attached to both ends of the chain (see Fig. 5.3A). Spectra were obtained for three different chain lengths (6, 15, and 50 bistable units in length) and was determined to be independent of d. The rigid epoxy supports were held apart at fixed distances by acrylic braces. These ensure that the morphology of the soft structure remains in a controlled configuration during the dynamic tests. The acrylic braces were in turn glued to steel laboratory stands on an

optical table, to minimize undesired vibrations. As expected for a soft, dissipative material, the transmittance spectra (defined as the ratio between the measured output and input accelerations, $A_{\text{out}}(\omega)/A_{in}(\omega)$) clearly indicate that small-amplitude excitations are rapidly dissipated due to the strong damping intrinsic to the material (see Fig. 5.3B). In fact, at frequencies above 550 Hz, all energy is essentially dissipated before traveling through only 6 bistable units (independently of the direction of transmission or the state of the bistable elements). For longer distances (50-100 repeating units) even lower frequencies (100 Hz or less) show a drop of at least 20 dB through the structure, meaning that no more than about 1% of the input acceleration is measured at the output for these low frequencies. These results confirm that the material from which the medium is architected is intrinsically highly dissipative and does not enable propagation of small-amplitude elastic waves over long distances.

5.3.2 Response under large amplitude excitations

While the architected medium does not enable propagation of small-amplitude elastic waves over long distances due to the intrinsic damping of the polymer, moderate- and large-amplitude excitation can lead to a very different response. If the bistable elements are initially set to their lower-energy (undeformed) stable configuration ($x = x_{s1} = 0$ in Fig. 5.1C, corresponding to the top image in Fig. 5.1D), displacing an element even to large amplitudes does not lead to a transition wave due to the energetically unfavorable (energy-absorbing) transition of each element [97, 98]. Therefore, since small-amplitude linear modes also disintegrate because of dissipation (Fig. S2), there exist no stable modes of energy transport when the elements are in the low energy state. However, if the bistable elements are initially set to their higher-energy (deformed) stable configuration ($x = x_{s0}$ in Fig. 5.1C, corresponding to the bottom image in Fig. 5.1D), a sufficiently large displacement applied to any of the bistable elements can cause the displaced element to transition states, producing a nonlinear transition wave that propagates indefinitely outward from the point of initiation with constant speed and shape. This is due to both (i) an equilibrium between dispersive and nonlinear effects of the periodic structure [99] and (ii) a release of energy that equals the effects of dissipation as, stimulated by the wavefront, each of the bistable elements along the chain transitions from its higher to lower stable energy state (i.e., from $x = x_{s0}$ to $x = x_{s1} = 0$).

To characterize the propagation of such nonlinear waves experimentally, we used a high-speed camera and tracked the location of each bistable element along the chain as a function of time. Measurements of the transition waves were made

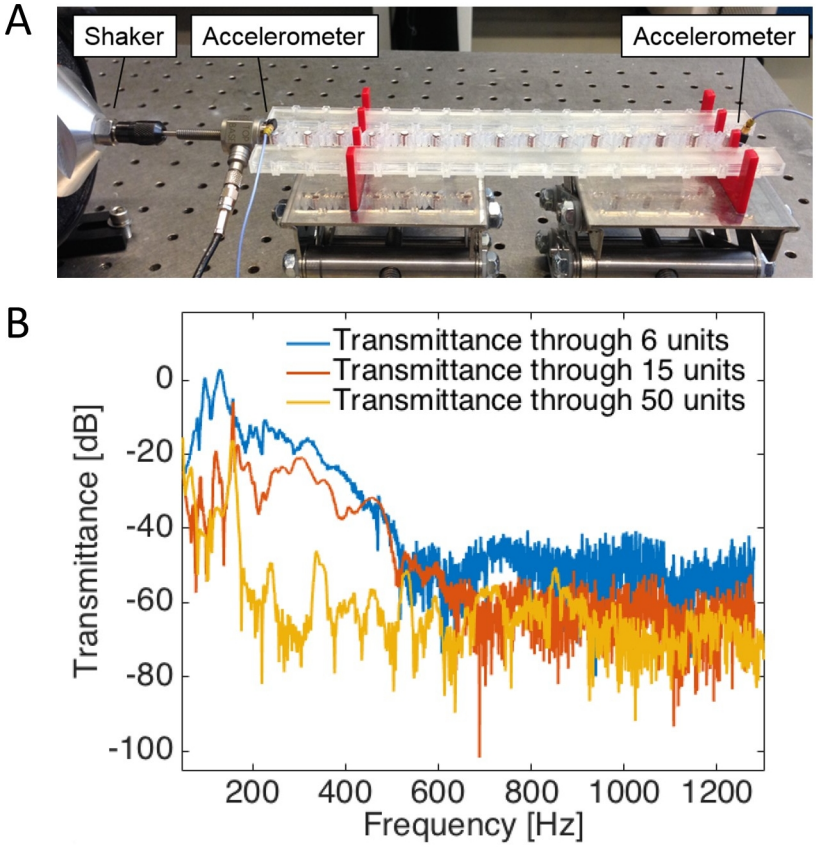

Figure 5.3: (A) The shaker (left) was attached to an accelerometer that was directly glued to the samples; the accelerator used to measure the output was glued to the other end of the sample; the acrylic braces (red) were used to hold the soft architecture at well-defined widths, and were glued to the laboratory stands to prevent unwanted movement; (B) small amplitude, linear excitation from either end of the chain is rapidly dissipated due to the damping intrinsic to the polymer, as is particularly evident with increasing frequency, shown here for samples with 6, 15, and 50 bistable units.

using a Phantom v7.1 camera. Two halogen floodlights were positioned to provide sufficient lighting for the high-speed camera to record the experiments solely with light reflected from the sample. Since at the wavefront, the bistable elements transition from one stable configuration to the other, we monitor the displacement of each unit relative to its two stable configurations (x_{s0} and x_{s1}). For the i-th unit, we therefore introduce two normalized distances,

$$\hat{x}_i^{s1} = \left|\frac{x_i - x_{s1}}{x_{s0} - x_{s1}}\right|, \qquad \hat{x}_i^{s0} = \left|\frac{x_{s0} - x_i}{x_{s0} - x_{s1}}\right|, \tag{5.1}$$

x_i being the position of the i-th bistable element along the chain. In Fig. 5.1E we visualize the propagation of the nonlinear wave by showing for each unit its

normalized distance from the nearest stable configuration,

$$\hat{S}_i = \min\left(\hat{x}_i^{s1}, \hat{x}_i^{s0}\right), \tag{5.2}$$

at different times. If $\hat{S}_i = 0$, the i-th element is in either of its two stable configurations, while $\hat{S}_i > 0$ indicates that the unit is passing through the energy barrier separating them. The experimental data of Fig. 5.1E clearly show that, at the wavefront, a few bistable units (in this case about 4) are undergoing a change from one stable state to the other at any given time, and that the transition sequentially propagates through the elements along the chain. Importantly, we also find that this transition wave propagates with a constant shape, clearly indicating that both dispersive and dissipative effects are overcome in the structure.

The speed of the nonlinear wave can be obtained by monitoring the evolution of the normalized distance $\hat{x}^{s0}$ for each bistable unit during the entire experiment, as in Fig. 5.4A. Since in this contour map the blue and red colors indicate bistable units in the high-energy and low-energy stable configurations, respectively, the sequential change of each of the elements along the chain from one stable state to the other is evident. Furthermore, the constant slope of the boundary between the pre- (blue) and post- (red) transition regions reveals a constant propagation velocity (in this case 3.4 ± 0.1 m/s). For systems with low wave speeds (usually $k = 80$ N/m and v on the order of a few meters per second), a 500 Hz recording rate was used. For higher-speed systems (usually $k = 2100$ N/m and v between 10-20 m/s) a higher recording rate of 1000 Hz was used. Note also that the pulse width for any time can be extracted from the map by taking a horizontal slice (i.e., a fixed time) of the plot in Fig. 5.4A and measuring the number of bistable elements in the midst of transitioning between solid blue and solid red (approximately 4 elements in width).

Another unique aspect of this system is that the propagation velocity and pulse shape are the same (within the margin of error) whether the wave is initiated in compression or tension, as revealed by comparison of the contour plots reported in Fig. 5.4A (for compression) and Fig. 5.4B (for tension). In both cases, the transition wave propagates with a constant velocity (3.4 m/s) and pulse width (~ 4 elements). The propagation of rarefaction pulses is a rare find and thus a noteworthy feature of this system. While compressive nonlinear solitary waves have been observed in nonlinear periodic systems as in, e.g., Hertzian contact-based chains [49, 66, 104] as well as in macroscopic nonlinear chains using magnetic connectors [95, 98], rarefaction pulses have not been found in those – among other reasons due to the

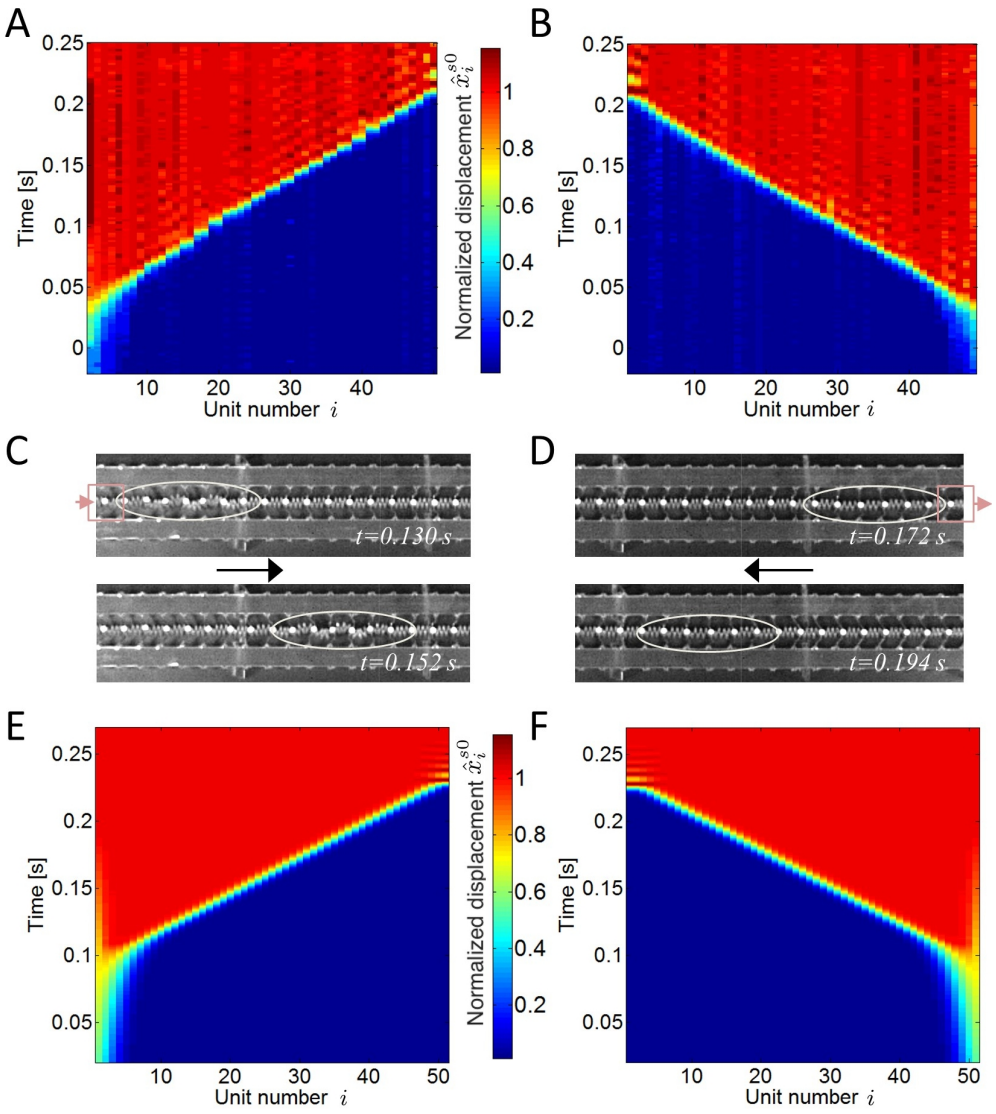

Figure 5.4: The transition wave can be initiated anywhere along the chain, with compressive and rarefaction pulses proceeding in opposite directions from the point of initiation (here d = 18.6 mm). (A-B) the normalized displacements of the individual bistable elements ($\hat{x}_i$ for each of the i elements in the chain) during the propagation of the wave, as recorded with a high speed camera at 500 Hz; these panels show the propagation of the transition with a constant velocity and pulse width, after a brief initiation period during which steady-state is established; (C-D) Optical images of the experiments during wave propagation (obtained from a high-speed camera), corresponding to the data in panels A-B; (E-F) Simulations corresponding to the experiments shown in panels A-B, showing excellent quantitative agreement; for the compression initiated pulse, the initiating displacement of the wave takes place on the left of the chain and is in the same direction as the pulse propagation; for the tension initiated pulse, the initiating displacement takes place on the right of the chain, and the local tensile displacement is in the opposite direction of the wave propagation.

lack of stiffness in tension. Finally, we note that the transition wave can also be initiated at any intermediate location along the chain, in which case a compressive pulse travels in one direction and a rarefaction pulse travels in the other direction, both propagating outward from the point of initiation.

5.4 Numerical results

We characterize the transition wave propagation using a 1D mechanical model, in which the position $x_i(t)$ of the middle of the i-th bistable element is governed by

$$m\frac{d^2x_i}{dt^2} - k[x_{i+1} - 2x_i + x_{i-1}] + \gamma\frac{dx_i}{dt} + \frac{dV}{dx_i} = 0, \tag{5.3}$$

where V is the quasi-1D on-site potential of each bistable element, γ is a linear damping parameter and k the connector spring stiffness. The linear damping model is a leading-order approximation to the complex dissipative nature of elastomers. The bistable potential V is numerically computed by nonlinear finite-element quasi-static simulations. A single bistable beam element consists of two inclined beams with a mass placed at the center. As the mass is rigid compared to the compliant beams, it is assumed that the force on the mass by the bistable structure is produced solely by the deformation of the beams. Due to the symmetry of the structure, the quasi-static deformation of only one tilted beam is modeled with appropriate boundary conditions. The beam is modeled using slender corotational beam finite elements [74] whose one-dimensional stretching and bending deformation are governed by a nonlinear Neo-Hookean material model with an initial slope of $E = 1.8$ MPa. Results of an example simulation are shown in Fig. 5.5A). The undeformed beam is first subjected to an initial vertical pre-compression v_0 according to the d value. The boundary node 'B' is then displaced horizontally from one stable point to another in displacement control and the resulting force required is recorded. The force-displacement function obtained in this way is fit with a seventh-order polynomial. The force-displacement polynomial is validated by comparison with the experimentally-measured force-displacement curve for $d = 17.5$ mm, as shown in Fig. 5.5B; note that the computed forces are multiplied by 2 to account for the force of one bistable element containing two tilted beams. This simulation was repeated for different d values to compute $V(x, d)$. We validate the numerically-obtained force–displacement curves by comparison to the experimental data shown in Fig. 5.1C. To simulate the response of the system under large-amplitude excitations, initially all nodes are placed in the high-energy configuration. The first node is then excited by displacing it from the high-energy stable point to the low-energy one, and the system response in time is

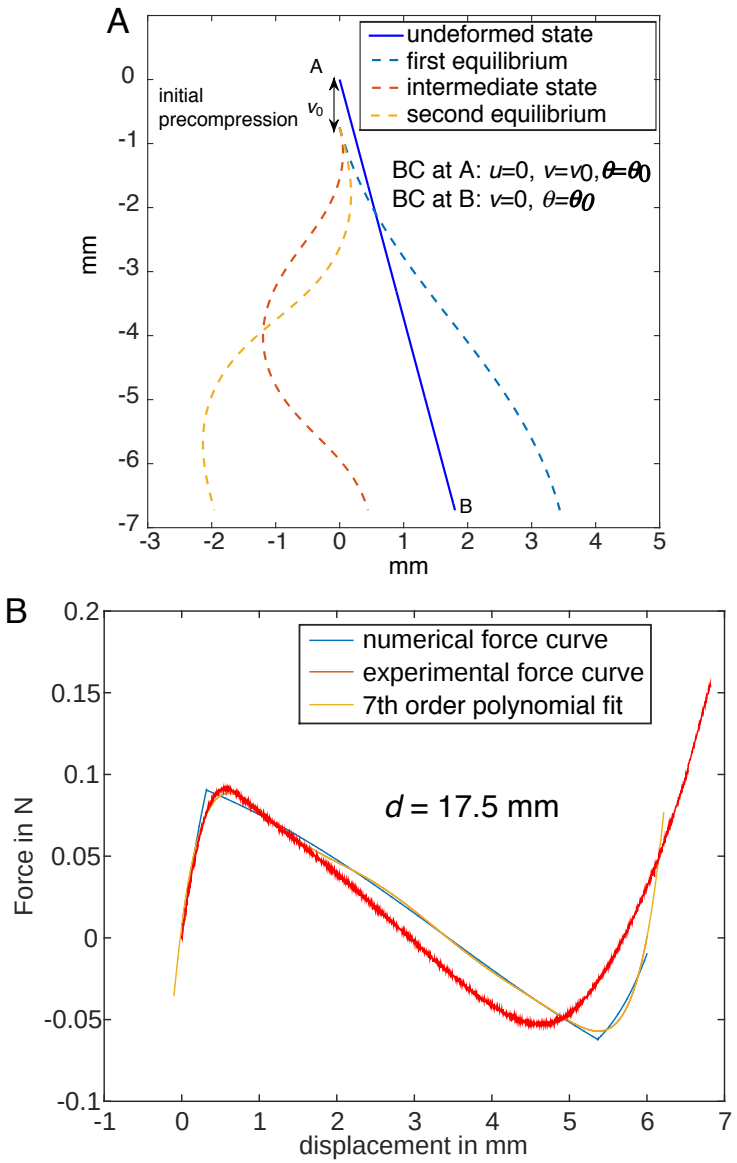

Figure 5.5: (A) An example of the beam deformation simulation is shown. All simulations were performed on only one half of the bistable element (i.e., on one tilted beam). Different configurations of the beam are shown as it is displaced from one stable configuration to another. The force at node 'B' is measured (and doubled to account for bistable element consisting of two tilted beams). (B) The numerical, experimental and best-fit force-displacement curves are shown for d = 17.5 mm. The graphics indicate that experimental and numerical results are in good agreement.

solved using a Newmark-β scheme. The only unknown model parameter, γ, was determined by fitting experimental wave speed data for a combination of values (k, d) = (80 N/m,17.5 mm) (see Fig. 5.6 for the comparison of experimental and simulation results by which the dissipation parameter was determined). With all

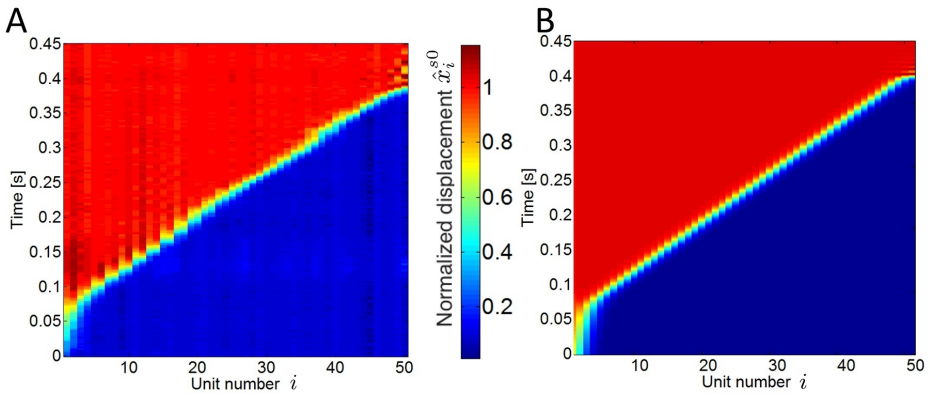

Figure 5.6: (A-B) Experimental and simulation results, respectively, corresponding to (k, d) = (80 N/m,17.5 mm), as used to determine the dissipation parameter in the model.

model parameters thereby determined, we examined systems with different combinations of geometric parameters with k ranging from 50 N/m-2500 N/m, d ranging from 14.5 mm to 19.0 mm with d = 19.0 mm corresponding to the undeformed state. As an example, Fig. 5.4E and Fig. 5.4F show simulated compression-initiated and tension-initiated pulses, respectively, which show excellent agreement with the experimental data discussed earlier (Fig. 5.4A-B).

5.5 Control of wave propagation

Results reported so far were obtained by testing a system characterized by connecting elements with stiffness k = 80 N/m and bistable beams with aspect ratio L/t = 18 and constant end-to-end distance d. However, both the width of the pulse and its propagation velocity can be greatly changed by manipulating either the nonlinear response of the bistable elements or the stiffness k of the linear coupling elements. While changes in k require fabrication of new units with different morphology (see Fig. 5.2), we can take advantage of the high-deformability of soft materials to tune the nonlinear response of the bistable beams by applying small lateral loads to change the beam end-to-end distance d. Critically, the wave characteristics are observed to depend only on such geometric parameters, and are independent of the initial conditions, consistent with the theory developed in Chapter 3.

We use our simulations to systematically investigate the effects of the parameters d and k on the behavior of the propagating wave. The results reported in Fig. 5.7A for four representative values of d show two key features. First, d has a large effect on the energy barrier separating the two stable configurations, which is reflected also in changes in the peak forces during transition. Second, d strongly affects the displacement necessary to obtain snap-through (from the high-energy state back to

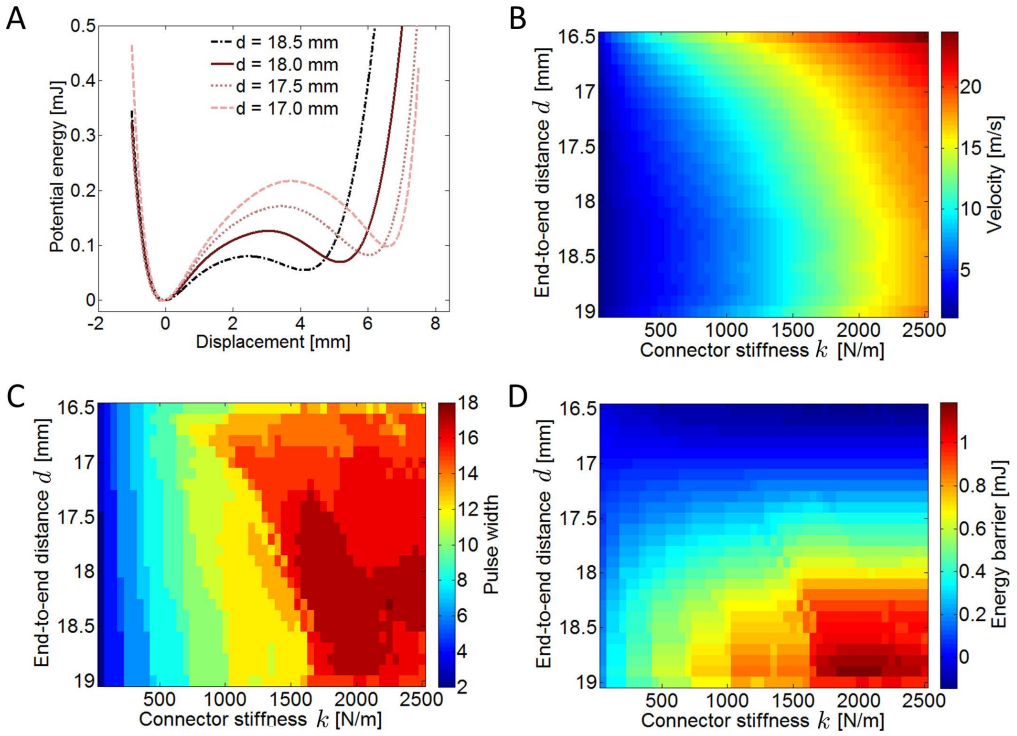

Figure 5.7: (A) The on-site potential as a function of x and d, as determined via quasi-static 1D displacement-controlled simulations of an individual bistable element; (B-C) Simulated values of pulse velocity and pulse width, respectively, as a function of end-to-end distance d and connector stiffness k; (D) The measured energy landscape (panel A) of the individual bistable elements is combined with the simulated pulse widths (panel C) to compute an approximate energy barrier E_{tot} for the entire propagating pulse (a function of both d and k).

the low-energy state) and thereby to initiate the transition during wave propagation. Using the numerical values for the on-site potential $V(x)$, simulations were subsequently performed to predict the wave characteristics for different connector element stiffnesses, k, and end-to-end distances, d. The wave speed (which is computed by tracking the point of maximum particle velocity), increases monotonically with increasing k (see Fig. 5.7B). However, the effect of d on the wave velocity is more complicated. The wave velocity is highly sensitive to changes in d when d is small, but much less sensitive when d is large. The associated width of the transition wave was also noted, defined as the number of nodes that simultaneously have displacements between 10% and 90% of the transition displacement. The results reported in (Fig. 5.7C) indicate that the pulse width increases with increasing k, showing the same trend as the velocity. For a constant connector stiffness value k, d does not have an effect on the width for lower stiffnesses but shows a similar variation as the

velocity for higher stiffnesses.

It is interesting to note that the trends for velocity (Fig. 5.7B) and width (Fig. 5.7C) contours show a correlation with the energy barrier for different d values as shown in Fig. 5.7A. For a constant inter-connecting element stiffness, the d values corresponding to high-energy barriers show lower velocity and width. This is because, when the energy barrier is high, each element needs to absorb more energy to overcome the barrier, thereby causing a slower transition rate and therefore a lower wave speed and vice-versa. Consequently, the energy barrier is the most important criterion in determining the transition speed and width of the displacement profile.

Because the N bistable elements that constitute a particular pulse are not simultaneously in morphologies that place them in the peak of their individual energy barriers, the total pulse energy barrier, E_{tot}, is calculated as

$$E_{\text{tot}} = \sum_{j=1}^{N} V(x_j) - V(x_{s0}), \tag{5.4}$$

where V and N are determined from the simulation results (Figs. 5.7A and C, respectively) and the x_j values are approximated by distributing them equally between x_{s1} and x_{s0} (i.e., $x_j = j\frac{x_{s0}-x_{s1}}{N+1}$). Fig. 5.7D shows this total potential energy barrier (E_{tot}), associated with the transition events of the individual bistable elements from their higher energy state ($x = x_{s0}$) to their lower energy state ($x = x_{s1}$). As expected, as the number of elements in the pulse (N) and the energy barrier for the individual elements increase, so does the total energy barrier required to initiate the pulse along a given portion of the chain, since the total energy barrier is the sum of the transient barriers of the individual elements currently undergoing transition.

While the results reported in Fig. 5.7 were obtained numerically, we also experimentally characterized the propagation of large amplitude waves in systems characterized by different values of k and d. First, to validate the numerical predictions for the on-site potential, we performed quasi-static 1D displacement-controlled experiments for different d values on an individual bistable element. The experimental results reported in Fig. 5.8 show a convincing agreement with the numerical results (Fig. 5.7A). Next, we experimentally investigated the effect of d and k on both wave velocity and pulse width. To explore the effect of d on the wave behavior, we tested the propagation of a transition wave through a system in which different values of d were assigned for the different experiments (Fig. 5.9). This can be done without fabricating a new sample for each experiment, since different values of d can be

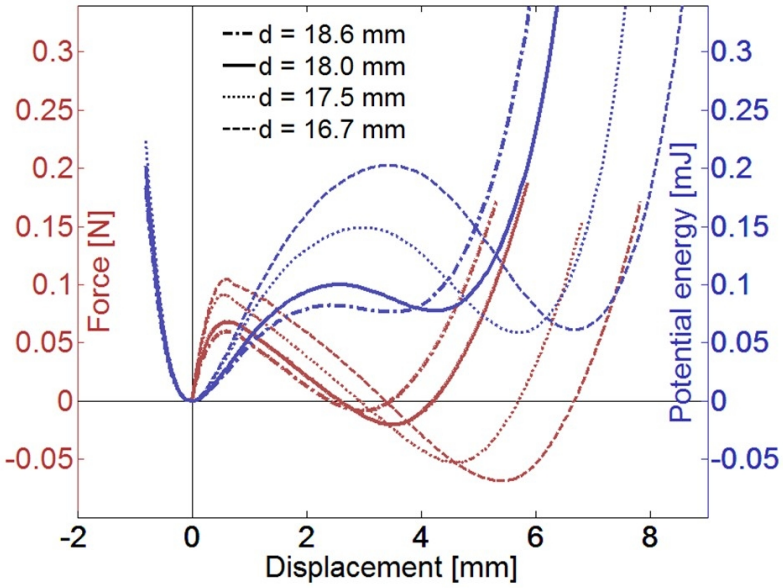

Figure 5.8: Experimental data obtained by directly measuring the force-displacement behavior of a single bistable element for different lateral constraints, d; the potential energy is calculated from this, showing a large effect of d on the energy barrier of the bistable elements.

achieved by applying a defined lateral displacement (d = 17.5 mm and 18.6 mm in Fig. 5.9). Comparison between the experimental results show an evident change in slope of the interface between the pre- and post-transitioned states (blue and red, respectively), indicating a variation in pulse velocity (the slope of the interface is inversely proportional to the speed). In particular, we observe a change in the wave

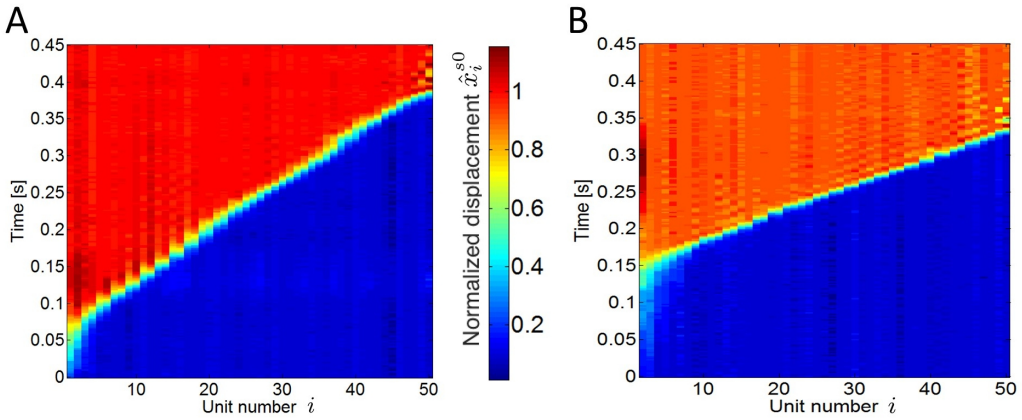

Figure 5.9: (A) Experiments show that when d is small (17.5 mm here) the energy barrier between the two stable states is larger and the wave propagation is slower; (B) when d is larger (18.6 mm here) the smaller energy barrier allows a larger propagation speed, as evidenced by the changed slope.

speed from about 1.9 m/s to 3.4 m/s for $d = 17.5$ mm and $d = 18.6$ mm, respectively, in a system for which $k = 80$ N/m. This trend is in agreement with simulations. In contrast, it is apparent that the pulse width is not significantly affected by d, as the number of bistable elements in the midst of transitioning between solid blue and solid red remains approximately constant as a function of time.

Figs. 5.11A and B show data for an experiment conducted on a system with stiff and soft connecting elements (2100 N/m and k=80 N/m, respectively – see insets in Fig. 5.11C). First, by comparing the slope of the boundaries in Figs. 5.11A and B, it is evident that the stiffness of the connecting elements affects the pulse velocity. In fact, we find velocities of approximately 18 m/s and 3.4 m/s for $k = 2100$ N/m and $k = 80$ N/m, respectively. Moreover, k strongly affects the pulse width (i.e., the number of bistable elements that at any given time are simultaneously in the process of transitioning between stable states). This is evident in Fig. 5.11C, where we compare experimental snapshots of $\hat{S}_i$ for the two systems and observe widths of approximately 25 and 4 elements for $k = 2100$ N/m and $k = 80$ N/m, respectively. Therefore, the stiffness of the linear connecting elements also greatly affects the pulse propagation confirming the results of our simulations.

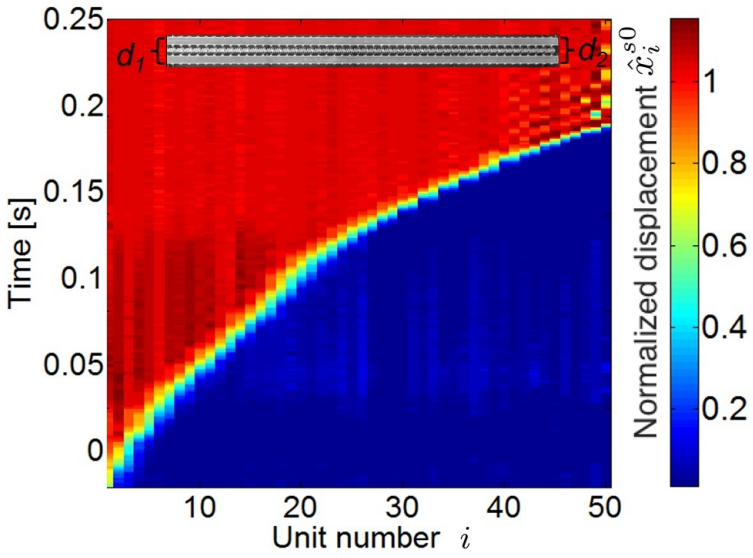

Figure 5.10: Because the system is deformable, different values of d can be used along the length of the system, resulting in spatially-varying energy barriers to propagation; this can be used to vary the velocity along the length of the chain, as it is here for a gradient structure (d is about $d_1 = 14.5$ mm at the left end and about $d_2 = 19.0$ mm at the right end, corresponding to measured speeds of 0.8 and 5.2 m/s, respectively).

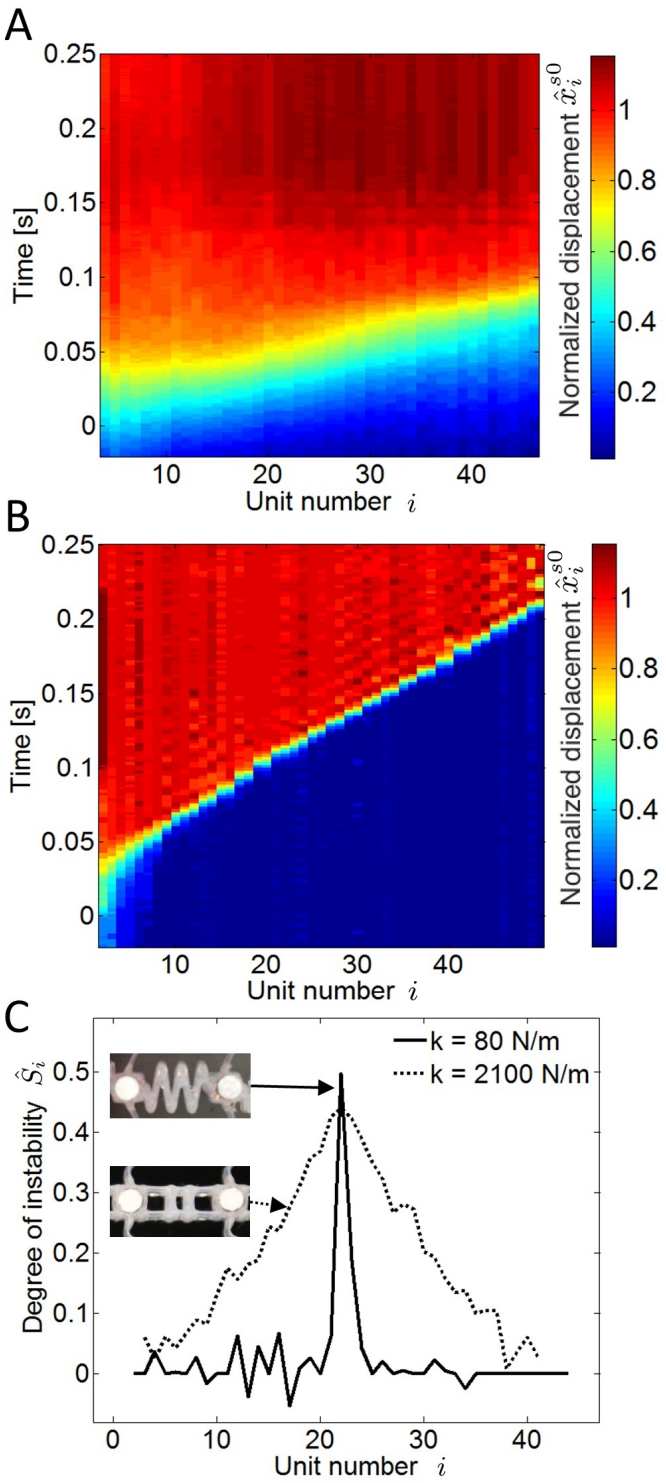

Figure 5.11: (A) When k is high (2100 N/m here) experiments show that both the pulse width and the pulse velocity (as determined by the slope) are much higher, even with the same value of d (18.6 mm), than (B) when k is low (80 N/m here); (C) this same comparison can be made by taking experimental snapshots of the two different systems (k=80 N/m and k=2100 N/m, corresponding to the differences in morphology of these elements, as pictured in the insets).

5.6 Tunable functional devices

Having demonstrated that the energy barrier for a transition wave to propagate can be controlled by tuning d and k, we now demonstrate how functional devices can be designed by carefully arranging the linear and nonlinear elements along the chain. To this end, it is critical to note that the pulse propagates independent of its initial conditions, so that it can be manipulated through entirely local geometric changes. This can be understood as a result of the high damping of the system, in which only the specific signal compatible with the local geometric parameters is able to propagate.

For example, an accelerator can be designed by applying different values of d spatially along the length of the system to achieve a controlled variation in velocity. Interestingly, this can be done without fabricating a specifically graded system, since the deformable architecture allows different values of d to be applied along the length of the system. The experimental results reported in Fig. 5.10 for a chain where d is approximately 14.5 mm at one end and about 19 mm at the other show an evident change in slope of the interface between the pre- and post-transitioned states (blue and red, respectively), indicating a variation in pulse velocity (the slope of the interface is inversely proportional to the speed). In particular, we observe a change in the wave speed by more than a factor of 6 from the left end of the chain to the right (0.8 to 5.2 m/s). The velocity can be seen to be continually varying along the length of the chain, but at each location it matches the expected velocities from Fig. 5.7B.

Further, a mechanical diode can be designed as a heterogeneous chain with soft linear horizontal connecting elements (corresponding to a low-energy barrier) in one region and stiff ones (corresponding to a high-energy barrier) in another region. As an example, in Fig. 5.12 we show results for such a system set to $d = 17.5$ mm comprised of 25 bistable elements with soft connecting elements ($k = 80$ N/m) and 25 bistable elements with stiff connecting elements ($k = 2100$ N/m). As shown in Fig. 5.7D, propagating pulses in these two distinct portions of the system are associated with very different energy barriers. When a pulse is initiated in the soft region ($k = 80$ N/m), where it possesses a small width (approximately 4 units) and a resulting low energy barrier (E_{tot}=0.2-0.3 mJ), it is unable to continue propagating when it reaches the stiff region ($k = 2100$ N/m), where a wide pulse (approximately 20 units) and high energy barrier are encountered (E_{tot} =1 mJ). As a result, the pulse freezes indefinitely at the soft-stiff boundary, with the wave

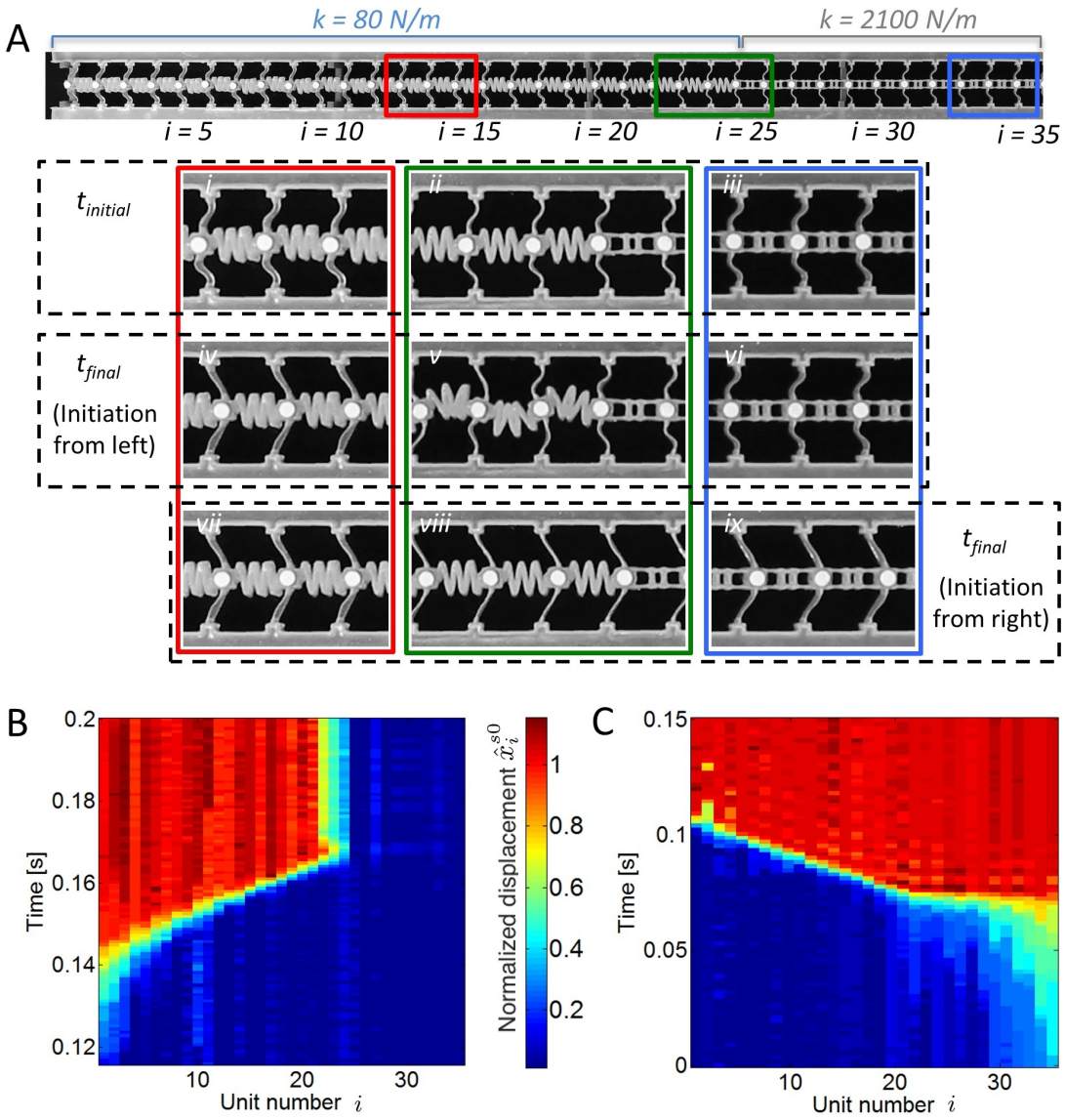

Figure 5.12: (A) A functional soft mechanical diode can be realized by creating a heterogeneous chain comprised of a region with soft connectors and a small energy barrier (left) and a region with stiff connectors and a large energy barrier (right); a pulse initiated in the soft region (from the left) cannot pass into the stiff region due to the large energy barrier, causing the pulse to freeze indefinitely at the interface (panel A, windows *iv* – *vi* and panel A); in contrast (panel A, windows *vii-ix* and panel (C) when the pulse is initiated in the stiff region the propagation continues into the soft region and through the whole chain without interruption.

energy that has not already been dissipated being stored in the elastic deformation of the local structure (Fig. 5.12A-center, Fig. 5.12B). In contrast, a pulse initiated in the stiff region readily propagates through the soft region as well (Fig. 5.12A-bottom, Fig. 5.12C), although a kink in wave velocity is observed at the transition between stiff and soft (a result of the change in k - Fig. 5.12C). The fact that the wave velocity rapidly changes at the boundary is an interesting manifestation of the system's insensitivity to initial conditions. Also, note that the large-amplitude wave is essentially insensitive to any fabrication-induced imperfections in the system.

The final equilibrium wave profile of the system depends on the internal equilibrium between the energy generated by the transition and the energy dissipated by the material damping and is therefore not dependent on the initial conditions. The latter only affect the transient time needed for the pulse to achieve its equilibrium configuration. Indeed, integration of Eq. (5.3) under the assumption of a smooth, stable propagating wave form shows that the total kinetic energy per mass, E, transported by the pulse and its velocity v are related by $E/v = \Delta V/(2\gamma)$, where ΔV denotes the potential energy difference between the two stable points, consistent with the results of Chapter 3. The initial conditions (as well as the connector stiffness k) do not affect this scaling law.

Using similar principles, more complicated functional devices can be designed, such as mechanical logic gates (Fig. 5.13). One can define the high-energy state of the bistable element ($x = x_{s0}$ in Fig. 5.1D) as logical state 0 and the low energy state ($x = x_{s1}$ in Fig. 5.1D) as logical state 1, and then design systems that predictably control pulse propagation in accordance with the energy barrier relationships in Fig. 5.7D. For example, the bifurcated chain in Fig. 5.13 was designed with a fixed value of k everywhere (80 N/m), corresponding to the left of Fig. 5.7D, with the two input chains set to $d = 17.5$ mm. When the end-to-end distance of the tilted beams in the vertical output chain, d_{out}, is small (e.g., $d_{\text{out}} = 16.7$ mm) the energy barrier is sufficiently high that both input chains must have been activated by propagating transition waves in order to continue propagation through the output (Fig. 5.13B), behaving as a soft mechanical logical AND gate. However, the very same system becomes a logical OR gate when d_{out} is increased sufficiently (e.g., to $d_{\text{out}} = 18.6$ mm), as in Fig. 5.13C. In this case, since the energy barrier of the output chain is smaller (less than 0.1 mJ), if either of the input chains has propagated the transition wave, the wave will propagate through the output chain. Similar behavior can be obtained by other combinations of beam geometries and linear connectors,

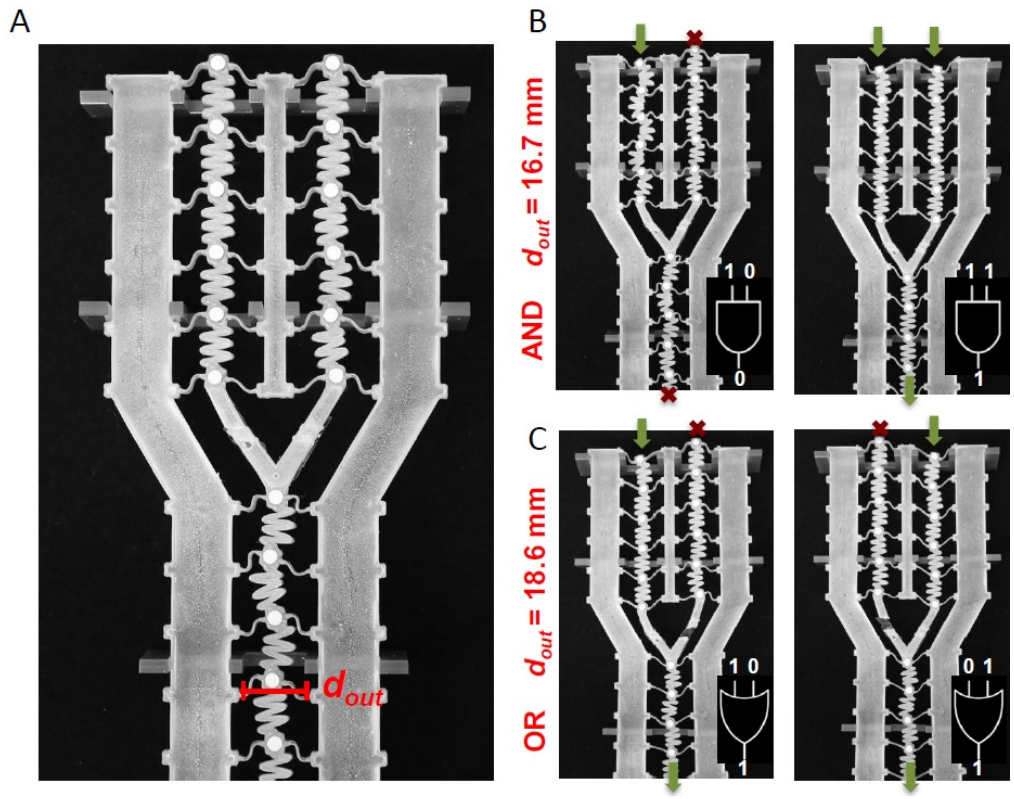

Figure 5.13: (A) A bifurcated chain demonstrating tunable logic in a soft mechanical system; the distance d_{out} determines the logical behavior, producing either an AND or an OR gate from the same system; (B) when d_{out} is small (in this case 16.7 mm) the energy barrier is higher, and both input chains must be transitioned in order for the wave to propagate through the output, comprising the function of a logical AND gate; (C) by increasing d_{out} (to 18.6 mm in this case), the energy barrier to continue propagation in the output chain decreases in a predictable manner, producing logical OR behavior in which a transition wave in either input chain has sufficient energy to initiate propagation in the output chain.

using Fig. 5.7D as a guide.

5.7 Conclusions

We have designed, printed, and demonstrated a system that enables the propagation of a signal without distortion through soft, dissipative media over arbitrary distances. The soft medium damps out linear waves, leaving only the desired transition wave. The precisely architected system makes use of beam-based units exhibiting asymmetric bistabilities to achieve the propagation of nonlinear transition waves in which the dissipation inherent to the polymer is overcome by the local release of elastically-stored energy during the transition of the individual bistable units from a high-energy to a low-energy configuration. The medium thereby undergoes a phase

transition as the wave pulse propagates through it. Interestingly, the wave pulse itself locally stimulates the release of the stored elastic energy as it propagates. While we have used beam pairs as a simple way to produce the (1D) asymmetric bistable potential that we use to store elastic energy along the path of the wave, other higher-dimensional arrangements of beams [133] and shells [14] would also exhibit asymmetric bistability, and could therefore also be explored as alternative architectures for the phenomenon studied here.

Due to the intrinsically unidirectional transition from the high- to the low-energy state that each individual bistable unit undergoes during propagation, an external source of energy must be provided to reset the bistable elements to their higher energy state if additional propagation events are desired (which, for example, could be provided pneumatically or via chemical reactions, as has been demonstrated in other soft autonomous systems [157]). The high quality of the printed elastomer ensures that the system can be reused in this manner indefinitely, with a consistent response from cycle to cycle.

The soft system has the advantage of facile tunability (e.g., changing d) and control over wave speed, pulse width, and pulse energy, with pulse propagation independent of the initial conditions. Additionally, the linear coupling springs between the bistable units exert a large effect on pulse width and energy. A simple mechanical model was shown to accurately capture the wave characteristics and guide the design of functional soft logic devices, such as diodes, OR gates, and AND gates. This form of logic could be harnessed to introduce some level of feedback and control in truly soft autonomous systems (i.e., without the use of rigid electronics that introduce materials mismatches that can lead to failure). It is also unique in that the system undergoes relatively large-amplitude shape changes during its function, so that the process and output can be easily visualized. As discussed in previous work [133], the mechanical response of the beams is scale-independent, and the elastic nature of the mechanism ensures a mechanical response that is independent of rate and loading history. Our findings can therefore be adapted to other scales and contexts.

Chapter 6

CONCLUSIONS AND FUTURE DIRECTIONS

6.1 Summary

In this thesis, we studied nonlinear dynamical transitions between different states of equilibrium in deterministic systems. The switching behavior occurs in the form of a localized nonlinear transition wave, the properties of which, depended on the type of system under consideration. We systematically investigated the theory for conservative, dissipative, and diffusive systems and analyzed properties such as wave profile, velocity and energy transported in these lattices and experimentally verified the dissipative case experimentally in a strongly nonlinear lattice. Further, we used this theory to design novel structures in soft material systems capable of transmitting nonlinear transition waves.

In Chapter 2, we studied the mechanics of an array of bistable elements connected through linear springs. We showed that there are three different modes of wave propagation in this system. In the linearized regime, linear elastic waves propagate where the wave number and frequency are linked through the dispersion relation. There is a low-frequency bandgap due to the presence of the bistable elements. In the weakly nonlinear regime of wave propagation, the bistable forcing function can be approximated by a cubic polynomial and the governing equation can be reduced to a nonlinear Schrödinger equation through a perturbation analysis. This equation has an envelope solitary wave solution. Finally, in the large amplitude strongly nonlinear regime of wave propagation, we find a family of kink soliton solutions that can propagate through the system. The kinks have a constant Hamiltonian that is proportional to the inverse of $\sqrt{c_0^2 - v^2}$, where c_0 is characteristic sound speed, and v is the velocity of the system. We derived closed form solutions for all three regimes of wave propagation.

In Chapter 3, dissipative and diffusive phase transitions in discrete systems and continua were studied. In these systems, we found that the small-amplitude modes that are seen in the conservative case are damped out and only the large-amplitude kink transition wave solution is stable. Unlike family of solutions seen in the conservative bistable lattice, the transition wave, in this case, has a stationary form and travels with a constant velocity that is independent of the initial conditions. The

kinetic energy is an invariant and linearly scales with the velocity of the wave for any general nonlinear interaction potential and on-site bistable topology. We showed that, as the kinetic energy scaling is linear, superposition holds for multi-stable phase transitions. For a general nonlinear damping, the energy scaling is converted to a dissipation inequality or a statement of the second law of thermodynamics. When discreteness effects become prominent, the kinetic energy oscillates about a mean and the mean is linearly related to the velocity through the energy law.

In Chapter 4, we constructed a strongly nonlinear mechanical system with interaction nonlinearities and on-site asymmetric bistable topologies, that allows transitions from a high-energy phase to a low-energy phase. We showed that the transition waves in this system are unidirectional and can propagate only from the high-energy phase to the low-energy phase. We further showed that, due to discreteness effects, the energy of the traveling wave oscillates about a mean value. The mean value is given by the kinetic energy transport law from Chapter 4 and the frequency of oscillations is related to the velocity of wave propagation and the lattice parameter. We also perform a sensitivity analysis with respect to the bistable potential and interaction coefficient. We found that, below a critical interaction coefficient, the transition wave does not propagate, which is similar to propagation failure seen in reaction-diffusion bistable systems.

In Chapter 5, we used this theory to design new structures (made of highly dissipative materials such as polymers) capable of undergoing phase transitions to transmit stable mechanical signals. As these materials are dissipative in nature, linear signals are damped out quickly, which poses a challenge for signal propagation. We tackled this problem by designing a lattice similar to the one proposed in Chapter 2. The nonlinearity of instabilities was utilized to counter the effect of dissipation and dispersion to propagate stable transition waves. We found that the properties of this waveform can be controlled by changing the pre-compression within the lattice. Further, we built functional logic devices from these structures to replicate diodes, AND, and OR gates.

6.2 Future work

6.2.1 A note on ferroelecrtrics

Ferroelectric materials are a class of piezoelectric materials that show a spontaneous polarization in their equilibrium configuration below a certain temperature called the Curie temperature. The micro-structure of a ferroelectric material typically

consists of regions of different crystal orientations called grains. Each grain is composed of a mixture of different variants of polarization configurations. A region having a homogeneous state of polarization is called a domain and the boundary separating two domains is called a domain wall. Upon the application of an external electric field, the domain walls start moving such that the net polarization aligns itself with the electric field. An electric field can thus be used to switch the state of polarization within the material. This switching phenomenon has been used for applications such as memory devices [132]. Further, the strain field and polarization are coupled and hence the field can also be used for deforming the material, making ferroelectrics excellent candidates for actuation mechanisms. Modeling the electromechanical coupling and the domain switching process across the various scales is key to understanding the mechanics of these materials. In the past, these materials have been modeled using phase-field techniques with polarization being the order parameter using a Ginzburg-Landau-Devonshire potential. Numerical simulations have been performed for single crystal and polycrystalline $BaTiO_3$, $PbTiO_3$, and $PbZr_{1-x}Ti_xO_3$ (PZT) based on this approach [78–80, 144, 170, 171]. The dynamics of ferroelectric domain wall motion (that leads to switching) is modeled using a gradient flow technique in which the driving force is chosen to be proportional to the polarization evolution. This section focuses on how the energy transport law, derived in Chapter 3, can be used to compute the domain wall velocity in the Ginzburg-Landau-Devonshire model for a ferroelectric ceramic. We further show that the scaling between the velocity and electric field in the theoretical model is different from that as seen in experiments, and further delineate a technique to model the kinetics accurately.

We describe a ferroelectric body Ω by displacement field $\boldsymbol{u}(\boldsymbol{x}, t)$, electric potential $\phi(\boldsymbol{x}, t)$, and the polarization field $\boldsymbol{p}(\boldsymbol{x}, t)$, where $\boldsymbol{x} \in \Omega$ and $t \in \mathbb{R}$ denote position and time, respectively. The kinematic relations introduce the infinitesimal strain tensor $\boldsymbol{\varepsilon} = \frac{1}{2}(\nabla \boldsymbol{u} + \nabla \boldsymbol{u}^{\mathsf{T}})$ and the electric field $\boldsymbol{e} = -\nabla\phi$. Tractions $\boldsymbol{t}_0$ and displacement $\boldsymbol{u}_0$ boundary conditions are applied on subsets of the body, $\partial\Omega_t$ and $\partial\Omega_u$, respectively. Similarly, q_0 and ϕ_0 are charges and voltages applied to subsets of the surface, $\partial\Omega_q$ and $\partial\Omega_\phi$, respectively. The body force is $\boldsymbol{b}$ and the volume free charge density within the material is ω. The Helmholtz energy density of the body is

$$\Psi(\boldsymbol{p}, \nabla\boldsymbol{p}, \varepsilon, \boldsymbol{d}) = \psi_{\text{Landau}}(\boldsymbol{p}) + \psi_{\text{grad}}(\nabla\boldsymbol{p}) + \psi_{\text{ES}}(\boldsymbol{p}, \varepsilon) + \frac{1}{2}\kappa_0|\boldsymbol{d} - \boldsymbol{p}|^2 \tag{6.1}$$

where $\boldsymbol{p}$ is the polarization, ε is the infinitesimal strain tensor, $\boldsymbol{d}$ is the electric displacement vector, and κ_0 is the permittivity of free space. The Landau energy

has minima corresponding to the spontaneous polarizations within the material, the gradient term captures the domain wall energy density and ψ_{ES} accounts for the electromechanical coupling energy density. The constitutive relation $\boldsymbol{d} = \kappa_0 \boldsymbol{e} + \boldsymbol{p}$ relates the electric field and displacement via permittivity κ_0. The electric enthalpy density of the body is given by the Legendre transform of the Helmholtz energy density,

$$W(\boldsymbol{p}, \nabla \boldsymbol{p}, \varepsilon, \boldsymbol{e}) = \sup_{\boldsymbol{d}} \Psi(\boldsymbol{p}, \nabla \boldsymbol{p}, \varepsilon, \boldsymbol{d}) - \boldsymbol{e} \cdot \boldsymbol{d}. \tag{6.2}$$

The total energy of the body is therefore given by

$$\begin{aligned} \Pi = &\int_\Omega \left[\psi_{\mathrm{Landau}}(\boldsymbol{p}) + \psi_{\mathrm{grad}}(\nabla \boldsymbol{p}) + \psi_{\mathrm{ES}}(\boldsymbol{p}, \varepsilon) \,\mathrm{d}V - \boldsymbol{e} \cdot \boldsymbol{p} - \frac{\kappa_0}{2} \boldsymbol{e} \cdot \boldsymbol{e} \right] \mathrm{d}V \\ &- \int_{\partial\Omega_t} \boldsymbol{t}_0 \cdot \boldsymbol{u} \,\mathrm{d}S + \int_{\partial\Omega_q} q_0 \phi \,\mathrm{d}S - \int_\Omega \boldsymbol{b} \cdot \boldsymbol{u} \,\mathrm{d}V + \int_\Omega \omega \phi \,\mathrm{d}V. \end{aligned} \tag{6.3}$$

We assume that the external body and surface microforces that arise due to variations in $\boldsymbol{p}$ and $\nabla \boldsymbol{p}$ [144] are zero. The governing equations in static equilibrium can be obtained by minimizing the variational derivative of the free energy functional. Computing the first variation gives

$$\begin{aligned} \delta\Pi = &\int_\Omega \left(y_i \delta p_i + \sigma_{ij} \delta \varepsilon_{ij} + \tau_{ij} \delta p_{i,j} + d_i \delta \phi_{,i} \right) \mathrm{d}V \\ &- \int_{\partial\Omega_t} t_{0i} \delta u_i \,\mathrm{d}S + \int_{\partial\Omega_q} q_0 \delta \phi \,\mathrm{d}S - \int_\Omega b_i \delta u_i \,\mathrm{d}V + \int_\Omega \omega \delta \phi \,\mathrm{d}V. \end{aligned} \tag{6.4}$$

where we introduce the thermodynamic work conjugates $y_i = \partial W / \partial p_i$, $\tau_{ij} = \partial W / \partial p_{i,j}$ and stresses $\sigma_{ij} = \partial W / \partial \varepsilon_{ij}$. Here and in the following, we used conventional index notation with the Einstein summation convention. By integrating by parts, we obtain

$$\begin{aligned} \delta\Pi = &\int_\Omega \left(y_i - \tau_{ij,j} \right) \delta p_i - \left(\sigma_{ij,j} + b_i \right) \delta u_i - \left(d_{i,i} - \omega \right) \delta \phi \,\mathrm{d}V \\ &+ \int_{\partial\Omega_t} \left(\sigma_{ij} n_j - t_{0i} \right) \delta u_i \,\mathrm{d}S + \int_{\partial\Omega_q} \left(d_i n_i + q_0 \right) \delta \phi \,\mathrm{d}S + \int_{\partial\Omega} \tau_{ij} n_j \delta p_i \,\mathrm{d}S. \end{aligned} \tag{6.5}$$

As the energy is minimized, the first variation is equated to zero, which must hold for any subbody. Hence, we get the governing equations

$$\operatorname{div} \boldsymbol{\sigma} + \boldsymbol{b} = 0 \quad \text{in } \Omega \qquad \text{and} \qquad \boldsymbol{\sigma} \boldsymbol{n} = \boldsymbol{t}_0 \quad \text{on } \partial\Omega_t, \tag{6.6a}$$

$$\operatorname{div} \boldsymbol{\tau} - \boldsymbol{y} = 0 \quad \text{in } \Omega \qquad \text{and} \qquad \boldsymbol{\tau} \boldsymbol{n} = 0 \quad \text{on } \partial\Omega, \tag{6.6b}$$

$$\operatorname{div} \boldsymbol{d} = \omega \quad \text{in } \Omega \qquad \text{and} \qquad \boldsymbol{d} \cdot \boldsymbol{n} + q_0 = 0 \quad \text{on } \partial\Omega_q, \tag{6.6c}$$

along with essential boundary conditions $\boldsymbol{u} = \boldsymbol{u}_0$ on $\partial\Omega_u$, and $\phi = \phi_0$ on $\partial\Omega_\phi$. The equations represent mechanical equilibrium, electromechanical phase equilibrium and Gauss' law, respectively. Under non-equilibrium conditions, as in the case of dynamics, the right hand side of mechanical equilibrium equation is replaced by $\rho\ddot{\boldsymbol{u}}$ where ρ is the density of the body, and the phase equilibrium equation is replaced by a dissipative thermodynamic driving force $\boldsymbol{f}(\boldsymbol{p}, \dot{\boldsymbol{p}}, \nabla\boldsymbol{p}, \boldsymbol{e})$ that can be derived from a dissipation potential ϕ^* such that,

$$\boldsymbol{f}(\boldsymbol{p}, \dot{\boldsymbol{p}}, \nabla\boldsymbol{p}, \boldsymbol{e}) = \frac{\partial\phi^*}{\partial\dot{\boldsymbol{p}}} \qquad \text{and} \qquad \frac{\delta W}{\delta p} + \frac{\partial\phi^*}{\partial\dot{\boldsymbol{p}}} = 0. \tag{6.7}$$

We assume that the dissipation potential is differentiable everywhere. The Gauss' law remains unchanged in the dynamic case. The Clausius-Duhem entropy inequality in terms of the electric enthalpy states that

$$\dot{W} - \boldsymbol{\sigma} \cdot \dot{\boldsymbol{\varepsilon}} + \boldsymbol{d} \cdot \dot{\boldsymbol{e}} \leq 0, \tag{6.8}$$

thereby providing the constraint,

$$f(\boldsymbol{p}, \dot{\boldsymbol{p}}, \nabla\boldsymbol{p}, \boldsymbol{e}) \cdot \dot{\boldsymbol{p}} \geq 0. \tag{6.9}$$

The simplest kinetic law for the polarization field, compatible with these equations and commonly used in phase field models for ferroelectrics [144, 170], is based on gradient flow, i.e., $\boldsymbol{f}(\boldsymbol{p}, \dot{\boldsymbol{p}}, \nabla\boldsymbol{p}, \boldsymbol{e}) = \mu\dot{\boldsymbol{p}}$ with $\mu > 0$, giving rise to the Allen-Cahn-type evolution law $\mu\dot{p}_i = \tau_{ij,j} - y_i$ with inverse isotropic mobility μ.

We consider PZT as the model material for the analysis. The phase diagram of PZT is shown in Fig. 6.1 Above a $PbTiO_3$ composition of 50%, PZT can exist in one of two phases, a high-temperature cubic phase and a low-temperature tetragonal phase. The line separating the two phases is the Curie temperature line. A schematic of the two structural phases of PZT is shown in Fig. 6.2. Below the Curie temperature, the micro-structure of PZT consists of a mixture of six tetragonal variants as depicted in Fig. 6.3. This mixture can be modeled using a phase field Ginzburg-Landau energy density functional with the polarization as the mesoscale order parameter. The Ginzburg-Landau function has a minima corresponding to the polarization of each of these six variants. The total internal energy functional can be computed using first principles ab-initio DFT calculations. For our study, we use the energy functional by Völker et al. [155]. The Landau energy is given by a sixth-order

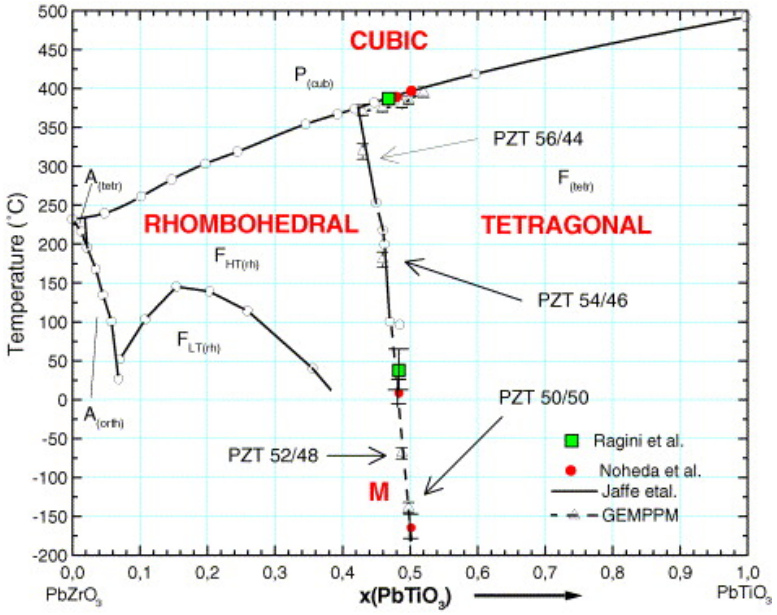

Figure 6.1: Phase diagram of PZT. (The figure has been adapted from [23])

polynomial of the form

$$\begin{aligned}\psi_{\text{Landau}}(\boldsymbol{p}) =& \alpha_1(p_1^2+p_2^2+p_3^2)+\alpha_{11}(p_1^4+p_2^4+p_3^4)+\alpha_{12}(p_1^2p_2^2+p_1^2p_3^2+p_2^2p_3^2)\\ &+\alpha_{111}(p_1^6+p_2^6+p_3^6)+\alpha_{123}(p_1^2p_2^2p_3^2)\\ &+\alpha_{112}(p_1^4(p_2^2+p_3^2)+p_2^4(p_3^2+p_1^2)+p_3^4(p_2^2+p_1^2)).\end{aligned} \tag{6.10}$$

This energy has minimas at the six spontaneous polarization states of the crystal.

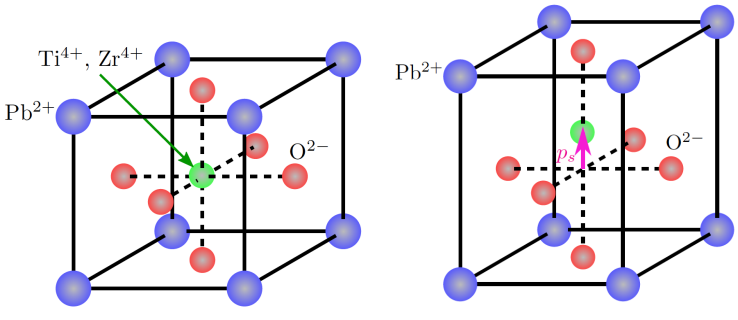

(a) T<T_c (b) T>T_c

Figure 6.2: (a) Cubic structure of PZT below the Curie temperature. (b) Tetragonal structure of PZT above the Curie temperature. (adapted from [161])

The gradient term is given by

$$\begin{aligned}\psi_{\text{grad}}(\nabla p) =& \frac{1}{2}G_{11}(p_{1,1}^2 + p_{2,2}^2 + p_{3,3}^2) + G_{12}(p_{1,1}p_{2,2} + p_{1,1}p_{3,3} + p_{3,3}p_{2,2}) \\ &+ \frac{1}{2}G_{44}((p_{1,2} + p_{2,1})^2 + (p_{1,3} + p_{3,1})^2 + (p_{2,3} + p_{3,2})^2),\end{aligned} \tag{6.11}$$

while the elastic energy and polarization coupling term have the following combined form,

$$\begin{aligned}\psi_{\text{ES}}(\boldsymbol{p}, \varepsilon) =& \frac{1}{2}C_{11}(\varepsilon_{11}^2 + \varepsilon_{22}^2 + \varepsilon_{33}^2) + C_{12}(\varepsilon_{11}\varepsilon_{22} + \varepsilon_{11}\varepsilon_{33} + \varepsilon_{11}\varepsilon_{22}) \\ &+ 2C_{44}(\varepsilon_{12}^2 + \varepsilon_{13}^2 + \varepsilon_{32}^2) + q_{11}(\varepsilon_{11}p_1^2 + \varepsilon_{22}p_2^2 + \varepsilon_{33}p_3^2) \\ &+ q_{12}(\varepsilon_{11}(p_2^2 + p_3^2) + \varepsilon_{22}(p_1^2 + p_3^2) + \varepsilon_{33}(p_1^2 + p_2^2)) \\ &+ q_{44}(p_1p_2\varepsilon_{12} + p_2p_3\varepsilon_{23} + p_2p_3\varepsilon_{23}) \\ &+ \beta_1(p_1^4 + p_2^4 + p_3^4) + \beta_2(p_1^2p_2^2 + p_1^2p_3^2 + p_2^2p_3^2).\end{aligned} \tag{6.12}$$

with

$$\begin{aligned}q_{11} &= -C_{11}Q_{11} - 2C_{12}Q_{12}, \\ q_{12} &= -C_{12}(Q_{11} + Q_{12}) - C_{11}Q_{12}, \\ q_{44} &= -4C_{44}Q_{44}.\end{aligned} \tag{6.13}$$

We use conventional index notation with comma indices denoting partial derivatives. The values of all constants in the energy densities are tabulated in Table 6.1. For our simulations, we normalize our results using the spontaneous polarization $p_0 = 0.58\,\text{C/m}^2$, the energy barrier between the wells $\Psi_{\text{max}} = 1.8325 \times 10^8\,\text{J/m}^3$, the length and time scales, $L = 10^{-11}$ m and $T = 10^{-10}$ s respectively.

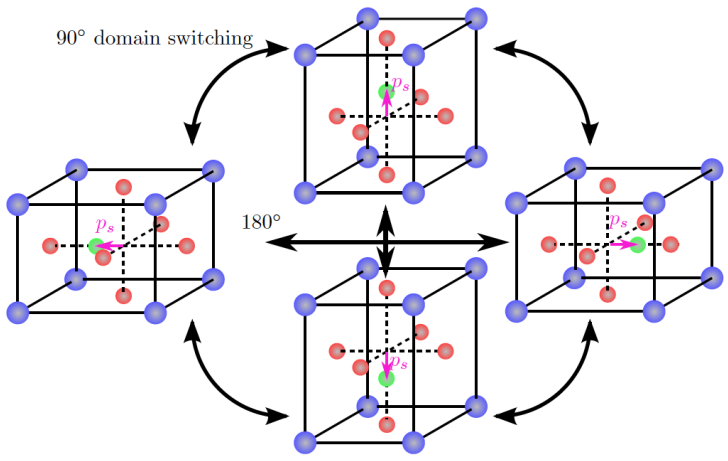

Figure 6.3: Four of the six Variants of PZT. The other two variants have polarizations into the plane and out of the plane (adapted from [161]).

Constant	Unit	Value
α_1	JmC^{-2}	-8.499×10^8
α_{11}	Jm^5C^{-4}	1.950×10^8
α_{12}	Jm^5C^{-4}	-9.750×10^8
α_{111}	Jm^9C^{-6}	2.117×10^9
α_{112}	Jm^9C^{-6}	1.687×10^{10}
α_{123}	Jm^9C^{-6}	4.823×10^9
G_{11}	Jm^3C^{-2}	2.9×10^{-11}
G_{12}	Jm^3C^{-2}	6.95×10^{-11}
G_{44}	Jm^3C^{-2}	6.95×10^{-11}
C_{11}	Jm^-3	351×10^9
C_{12}	Jm^-3	115×10^9
C_{44}	Jm^-3	91×10^9
Q_{11}	m^4C^{-2}	3.579×10^{-2}
Q_{12}	m^4C^{-2}	-5.335×10^{-3}
Q_{44}	m^4C^{-2}	1.923×10^{-2}

Table 6.1: Constants used in the energy density computation.

In order to understand the kinetics of domain walls in ferroelectrics, we consider a hypothetical situation that mimics the experiments performed on single-crystals [90, 91], as shown in Fig. 6.4. The 180° domain wall separates two anti-parallel polarizations p^- and p^+ in an infinite single crystal. An electric field is applied to the two ends of the crystal through a voltage drop between two electrodes separated by a distance l_e, causing the domain wall to move with a speed v. The tractions are zero on each material boundary and the surface charges are zero on the vertical boundaries at $x_1 \rightarrow \pm\infty$. The body forces and volume charges are assumed to be zero and inertial effects are ignored.

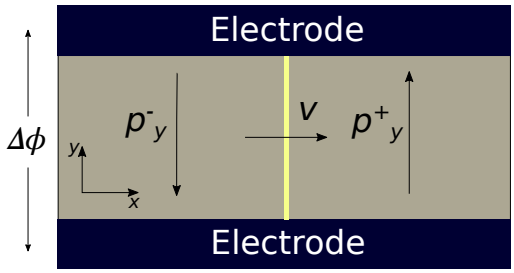

Figure 6.4: Schematic view of a 180° domain wall in a single-crystal ferroelectric ceramic capacitor with applied electric field e parallel to the domain wall that is moving with a velocity v.

In a spatially uniform region away from the domain wall, we may assume that

$$\boldsymbol{p}(\boldsymbol{x}) = \boldsymbol{p}, \quad \boldsymbol{\varepsilon}(\boldsymbol{x}) = \boldsymbol{\varepsilon} \quad \text{and} \quad \boldsymbol{y}(\boldsymbol{e}, \boldsymbol{p}, \boldsymbol{\varepsilon}) = 0. \tag{6.14}$$

The domain wall propagation can be thought of as a transition wave where the switching occurs from one set of polarization and strain state to another set,

$$\boldsymbol{x} \to \pm\infty : \qquad \boldsymbol{p} \to \boldsymbol{p}^{\pm}, \quad \boldsymbol{\varepsilon} \to \boldsymbol{\varepsilon}^{\pm} \tag{6.15}$$

The strains and polarizations are independent of the y-coordinate and therefore, from (6.14), we conclude that $\boldsymbol{e}$ is also independent of y. As there is no potential applied in the x-direction, the Gauss' law reduces to

$$e_{y,y} = 0 \quad \Rightarrow \quad e_y = \frac{\Delta\phi}{l_e}. \tag{6.16}$$

Similarly, the equations of mechanical equilibrium can be simplified as

$$\begin{aligned} \sigma_{xx,x} = 0 \quad &\Rightarrow \quad \sigma_{xx} = C_1 = 0, \\ \sigma_{yx,x} = 0 \quad &\Rightarrow \quad \sigma_{yx} = C_2 = 0. \end{aligned} \tag{6.17}$$

The constants are zero because of the zero-traction boundary conditions on all surfaces. σ_{yy} is also zero due to the boundary condition on the top and bottom. The spontaneous electrostrictive strains can be computed using (6.17) to give,

$$\begin{aligned} \varepsilon_{xx} &= Q_{12} p_y^2, \\ \varepsilon_{yy} &= Q_{11} p_y^2, \\ \varepsilon_{xy} &= 0. \end{aligned} \tag{6.18}$$

Finally, using the phase equilibrium equation and assuming a traveling wave solution with $\xi = x - vt$, we obtain

$$\begin{aligned} -v\mu\, p_{x,\xi} = \tau_{xx,x} + \tau_{xy,y} - y_x \quad &\Rightarrow \quad y_x = 0, \\ -v\mu\, p_{y,\xi} = \tau_{yx,x} + \tau_{yy,y} - y_y \quad &\Rightarrow \quad -v\mu\, p_{y,\xi} = \tau_{yx,\xi} - y_y. \end{aligned} \tag{6.19}$$

Multiplying the second equation by $p_{y,x}$ and integrating over the real axis gives

$$\begin{aligned} v \int_{-\infty}^{\infty} \mu p_{y,\xi}^2 d\xi &= -\int_{-\infty}^{\infty} \tau_{yx,\xi} p_{y,\xi} d\xi + \int_{-\infty}^{\infty} y_y p_{y,\xi} d\xi \\ &= [[-\tau_{yx} p_{y,\xi}]] + \int_{-\infty}^{\infty} \tau_{yx} p_{y,\xi\xi} d\xi + \int_{-\infty}^{\infty} y_y p_{y,\xi} d\xi, \end{aligned} \tag{6.20}$$

where $[[(\cdot)]]$ denotes a jump across the interface of the quantity $(\cdot)$. As the polarization states are uniform at $\pm\infty$, $[[-\tau_{yx} p_{y,\xi}]] = 0$. Now, let us consider $W_{,\xi}$:

$$W_{,\xi} = y_i p_{i,\xi} + \sigma_{ij}\varepsilon_{ij,\xi} + \tau_{ij} p_{i,j\xi} - d_i e_{i,\xi} = y_y p_{y,\xi} + \tau_{yx} p_{y,\xi\xi}. \tag{6.21}$$

Substituting this result in (6.20), we obtain

$$v = \frac{[[W]]}{\int_{-\infty}^{\infty} \mu p_{y,\xi}^2 \, d\xi}. \tag{6.22}$$

The term on the right-hand side determines the Eshelby traction acting on the domain wall. (6.22) is the energy transport equation for a ferroelectric ceramic. The polarization profile can be approximated by a hyperbolic tangent profile that goes from a $p^+(e_y)$ state to a $p^-(e_y)$ state. $p^\pm(e_y)$ are the polarizations corresponding to the stable minimizers of W. Fig. 6.5a shows the variation of $p^\pm(e_y)$ with the applied electric field. We define the coercive field e_c as the field for which the energy W becomes convex and has only one energy well or, in other words, p^+ and p^- coincide. We will restrict our attention to fields $e < e_c$. Fig. 6.5b shows a stationary polarization profile, for no applied electric field, that can be approximated as,

$$p_y(\xi) \approx \frac{p^+ + p^-}{2} + \frac{p^+ - p^-}{2} \tanh \frac{\xi}{h}, \tag{6.23}$$

where h is a measure of the width of the domain wall. Substituting this form in (6.22) with the approximate profile of the traveling wave gives,

$$v \approx \frac{3h[[W(p(e_y), 0, \varepsilon(e_y), e_y)]]}{\mu[p^+(e_y) - p^-(e_y)]^2} \tag{6.24}$$

We assume that h is a constant and independent of e_y. The width h is computed for a static ($e = 0$) simulation shown in Fig. 6.5b. Therefore, (6.24) provides an explicit approximate form for the velocity as a function of the electric field. A comparison between theory and experiments is shown in Fig. 6.6. The theory matches very well with the numerical simulations for small electric fields. There is a small discrepancy between the theory and numerics for electric fields close to the coercive field of PZT. This is because, at larger electric fields ($e \approx e_c$), the width of the domain wall is no longer equal to the width of a stationary domain wall, and hence the velocity is not accurately determined by the theory. In this manner, the energy law can be utilized to relate the domain wall velocity to the electric field.

In all previous continuum modeling studies, including the present, a deterministic Ginzburg-Landau formulation has been used to predict the domain wall motion in ferroelectric ceramics. However, this formulation does not lead to the correct scaling of the domain wall velocity with the applied electric field. According to experiments in single crystals of $BaTiO_3$ and $PbZr_{0.2}Ti_{0.8}O_3$, for small electric fields, the velocity of a 180° domain wall v is seen to have an Arrhenius-type relationship

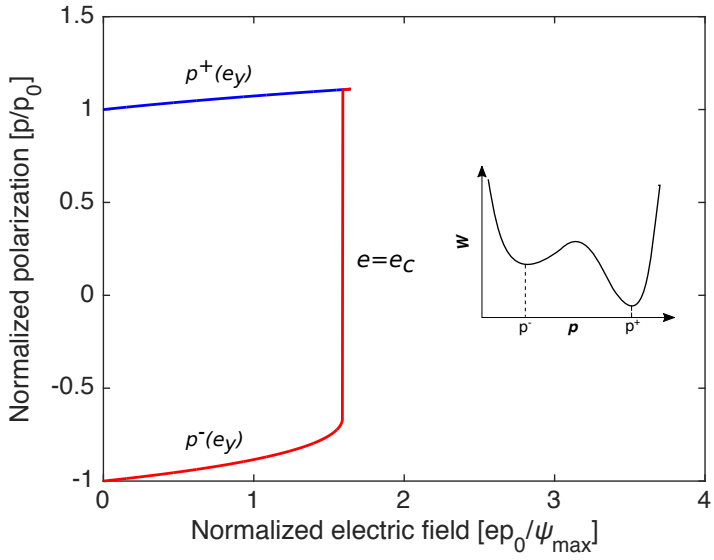

(a)

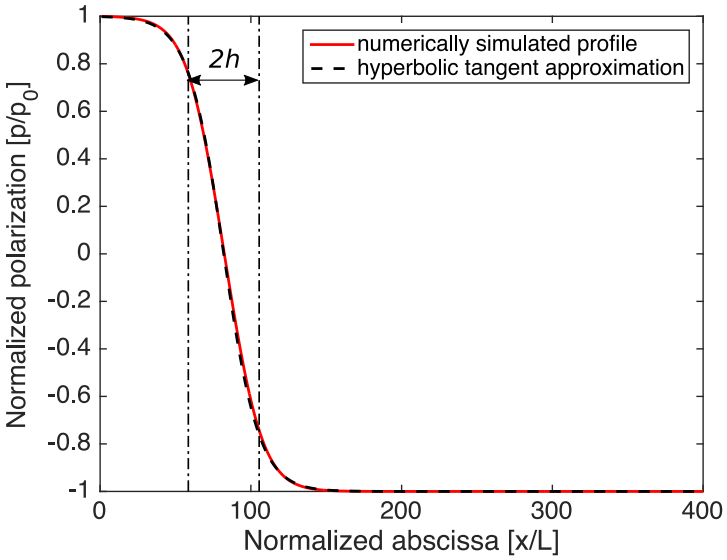

(b)

Figure 6.5: (a) Plot of equilibrium polarizations p^+ and p^- as functions of the applied electric field. The inset shows the energy W for a given electric field e_y with p^- and p^+ as its local minimizers. $p^\pm$ coincide for $e \geq e_c$. (b) Comparison between the simulated profile of the polarization for a stationary domain wall and the hyperbolic tangent approximation. As can be seen, the arc-tangent profile accurately represents the variation of polarization across the domain wall.

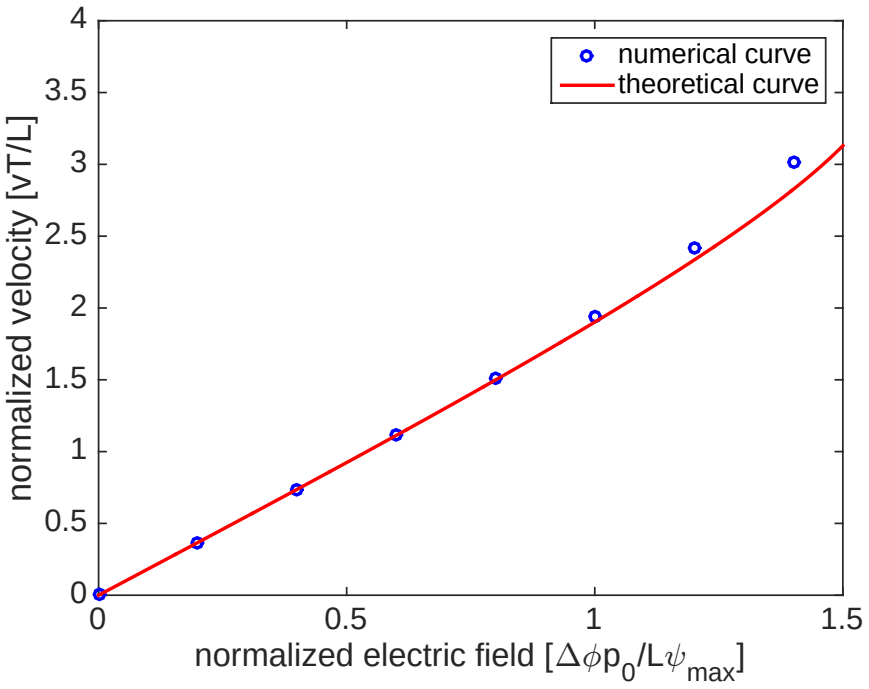

Figure 6.6: A comparison between theory and numerical simulations of the variation of velocity of the domain wall with applied potential difference.

with the applied electric field e,

$$v \propto \exp -\frac{e_a}{e} \tag{6.25}$$

where e_a is a thermal activation electric field [91, 151]. This relationship was first discovered by W. J. Merz and hence the relationship is known as Merz's law [91]. First principles molecular dynamics calculations have also confirmed the nature of this creep-dominated evolution process [82, 136]. As we show, using the energy scaling law, the relationship between the velocity and the electric field in the Ginzburg-Landau-Devonshire formulation seen in Fig. 6.6 is not consistent with the expected Arrhenius form. This gap between theory and experiments needs to be bridged. The switching is a statistically governed process caused by thermal activation, with nucleation occurring at defect sites. Hence, these statistical effects need to be included to capture the accurate kinetics of domain wall motion. A possible technique to model these thermal effects is by adding a Langevin force to the polarization evolution equation and measuring the average switching time. Defect sites can be modeled through a reduced Landau-Devonshire energy barrier at random sites within the numerical domain. According to the Kolmogorov-Avrami-Ishibashi model [8, 58, 68], the probability of switching is determined by a

characteristic time τ given by

$$\tau^{-1} \propto e^{-\Delta W/k_B T}, \tag{6.26}$$

where k_B is the Boltzmann constant, T is the temperature, and ΔW is the energy barrier encountered during switching. As the probability of switching is determined by the energy barrier, nucleation would therefore be preferred at these defect sites, in agreement with experiments. Further work, along these lines, will be reported in the future.

6.2.2 Future directions in theory of bistable lattices and continua

In a conservative lattice of bistable elements, when the on-site potential is asymmetric, a kink transition wave propagates with a constant velocity. However, as energy is generated at every subsequent transition of a bistable element in the lattice, it leads to background oscillations that grow with time. We believe that the oscillations have a structure similar to a dispersive shock wave [61, 85]. Characterizing these oscillations is a natural extension to the current work presented in this thesis.

For dissipative and diffusive systems, it is known that, if a transition wave solution exists, it obeys the energy transport law. However, whether a solution always exists or if there are certain conditions under which a solution exists is still not known. Therefore, proving the existence of such solutions is an important step in characterizing these solutions. A linearized state space analysis around the equilibrium points may suggest specific criteria for transition wave propagation.

6.2.3 Future directions in experiments in bistable lattices

In the chain of bistable elements with magnetic interactions, introduced in Chapter 4, all the elements were identically manufactured. It would be interesting to analyze the effect of defects in this system, e.g., when one of the elements is replaced by a different element, or the lattice spacing between two elements in the middle is changed, or if one of the elements is placed in reverse. Another interesting experiment would be to investigate a traveling wave through a superlattice with two different types of bistable elements.

The diodes and logic gates introduced in Chapter 5 promise novel applications. One potential application can be actuation in soft robotic systems such as octobots, where the bit of information propagated can be used to provide a certain instruction to the robot.

A drawback of the current system is that it allows for the propagation of a transition wave only once. If these elements can be set back to their original state through piezo-actuation, then they can be used multiple times for propagating waves.

These systems also show similarity to axon propagation in a myelinated nerve fiber [18]. Hence, they can be used as model systems to study neural circuits.

BIBLIOGRAPHY

[1] Rohan Abeyaratne and James K. Knowles. "A continuum model of a thermoelastic solid capable of undergoing phase transitions". In: *Journal of the Mechanics and Physics of Solids* 41.3 (Mar. 1993), pp. 541–571. ISSN: 0022-5096. DOI: 10.1016/0022-5096(93)90048-K. URL: http://www.sciencedirect.com/science/article/pii/002250969390048K.

[2] Rohan Abeyaratne and James K. Knowles. "Dynamics of propagating phase boundaries: Thermoelastic solids with heat conduction". en. In: *Archive for Rational Mechanics and Analysis* 126.3 (1994), pp. 203–230. ISSN: 0003-9527, 1432-0673. DOI: 10.1007/BF00375642. URL: http://link.springer.com/article/10.1007/BF00375642.

[3] Rohan Abeyaratne and James K. Knowles. "Kinetic relations and the propagation of phase boundaries in solids". en. In: *Archive for Rational Mechanics and Analysis* 114.2 (1991), pp. 119–154. ISSN: 0003-9527, 1432-0673. DOI: 10.1007/BF00375400. URL: http://link.springer.com/article/10.1007/BF00375400.

[4] Rohan Abeyaratne and James K. Knowles. "On the dissipative response due to discontinuous strains in bars of unstable elastic material". In: *International Journal of Solids and Structures* 24.10 (Jan. 1988), pp. 1021–1044. ISSN: 0020-7683. DOI: 10.1016/0020-7683(88)90105-9. URL: http://www.sciencedirect.com/science/article/pii/0020768388901059.

[5] Rohan Abeyaratne, Kim Sang-Joo, and James K. Knowles. "A one-dimensional continuum model for shape-memory alloys". In: *International Journal of Solids and Structures* 31.16 (Aug. 1994), pp. 2229–2249. ISSN: 0020-7683. DOI: 10.1016/0020-7683(94)90208-9. URL: http://www.sciencedirect.com/science/article/pii/0020768394902089.

[6] Andres F. Arrieta, Izabela K. Kuder, Tobias Waeber, and Paolo Ermanni. "Variable stiffness characteristics of embeddable multi-stable composites". In: *Composites Science and Technology* 97 (2014), pp. 12–18. ISSN: 0266-3538. DOI: http://dx.doi.org/10.1016/j.compscitech.2014.03.017. URL: http://www.sciencedirect.com/science/article/pii/S0266353814001006.

[7] W. Atkinson and N. Cabrera. "Motion of a Frenkel-Kontorova Dislocation in a One-Dimensional Crystal". In: *Physical Review* 138.3A (May 1965), A763–A766. DOI: 10.1103/PhysRev.138.A763. URL: http://link.aps.org/doi/10.1103/PhysRev.138.A763.

[8] Melvin Avrami. "Granulation, phase change, and microstructure kinetics of phase change. III". In: *The Journal of chemical physics* 9.2 (1941), pp. 177–184.

[9] Alexander M. Balk, Andrej V. Cherkaev, and Leonid I. Slepyan. “Dynamics of chains with non-monotone stress–strain relations. I. Model and numerical experiments”. In: *Journal of the Mechanics and Physics of Solids* 49.1 (Jan. 2001), pp. 131–148. ISSN: 0022-5096. DOI: 10.1016/S0022-5096(00)00025-9. URL: http://www.sciencedirect.com/science/article/pii/S0022509600000259.

[10] Alexander M. Balk, Andrej V. Cherkaev, and Leonid I. Slepyan. “Dynamics of chains with non-monotone stress–strain relations. II. Nonlinear waves and waves of phase transition”. In: *Journal of the Mechanics and Physics of Solids* 49.1 (Jan. 2001), pp. 149–171. ISSN: 0022-5096. DOI: 10.1016/S0022-5096(00)00026-0. URL: http://www.sciencedirect.com/science/article/pii/S0022509600000260.

[11] J. M. Ball and R. D. James. “Fine Phase Mixtures as Minimizers of Energy”. en. In: *Analysis and Continuum Mechanics*. DOI: 10.1007/978-3-642-83743-2_36. Springer Berlin Heidelberg, 1989, pp. 647–686. ISBN: 978-3-540-50917-2 978-3-642-83743-2. URL: http://link.springer.com/chapter/10.1007/978-3-642-83743-2_36.

[12] B. Banerjee. *An introduction to metamaterials and waves in composites*. Boca Raton, FL: CRC Press, 2011.

[13] M. Bär, M. Eiswirth, H.-H. Rotermund, and G. Ertl. “Solitary-wave phenomena in an excitable surface reaction”. In: *Physical Review Letters* 69.6 (Aug. 1992), pp. 945–948. DOI: 10.1103/PhysRevLett.69.945. URL: http://link.aps.org/doi/10.1103/PhysRevLett.69.945.

[14] N. P. Bende, A. A. Evans, S. Innes-Gold, L. A. Marin, I. Cohen, R. C. Hayward, and C. D. Santangelo. “Geometrically controlled snapping transitions in shells with curved creases”. In: *PNAS* 112 (2015), p. 11175.

[15] T. B. Benjamin and K. Hasselmann. “Instability of Periodic Wavetrains in Nonlinear Dispersive Systems [and Discussion]”. In: *Proceedings of the Royal Society A: Mathematical, Physical and Engineering Sciences* 299.1456 (June 1967), pp. 59–76. ISSN: 1364-5021. DOI: 10.1098/rspa.1967.0123. URL: http://rspa.royalsocietypublishing.org/cgi/doi/10.1098/rspa.1967.0123.

[16] K. Bertoldi and M.C. Boyce. “Wave propagation and instabilities in monolithic and periodically structured elastomeric materials undergoing large deformations”. In: *Phys. Rev. B* 78.18 (2008), p. 184107. DOI: 10.1103/PhysRevB.78.184107. URL: http://link.aps.org/doi/10.1103/PhysRevB.78.184107.

[17] D. Bigoni, S. Guenneau, A. B. Movchan, and M. Brun. “Elastic metamaterials with inertial locally resonant structures: Application to lensing and localization”. In: *Phys. Rev. B* 87.17 (May 2013), p. 174303. DOI:

10.1103/PhysRevB.87.174303. URL: http://link.aps.org/doi/10.1103/PhysRevB.87.174303.

[18] S. Binczak, J. C. Eilbeck, and A. C. Scott. "Ephaptic coupling of myelinated nerve fibers". In: *Physica D: Nonlinear Phenomena* 148 (Jan. 2001), pp. 159–174. ISSN: 0167-2789. DOI: 10.1016/S0167-2789(00)00173-1. URL: http://www.sciencedirect.com/science/article/pii/S0167278900001731.

[19] A. R. Bishop and W. F. Lewis. "A theory of intrinsic coercivity in narrow magnetic domain wall materials". In: *J. Phys. C: Solid State Phys.* 12.18 (1979), p. 3811. URL: http://stacks.iop.org/0022-3719/12/i=18/a=027.

[20] T. Blesgen, F. Fraternali, J. R. Raney, A. Amendola, and C. Daraio. "Continuum limits of bistable spring models of carbon nanotube arrays accounting for material damage". In: *Mechanics Research Communications* 45 (Oct. 2012), pp. 58–63. ISSN: 0093-6413. DOI: 10.1016/j.mechrescom.2012.07.006. URL: http://www.sciencedirect.com/science/article/pii/S0093641312001346.

[21] Nicholas Boechler, Georgios Theocharis, and C Daraio. "Bifurcation-based acoustic switching and rectification". In: *Nature Materials* 10.9 (2011), pp. 665–668.

[22] Victoria Booth, Thomas Erneux, and Jean-Pierre Laplante. "Experimental and Numerical Study of Weakly Coupled Bistable Chemical Reactors". In: *The Journal of Physical Chemistry* 98.26 (June 1994), pp. 6537–6540. ISSN: 0022-3654. DOI: 10.1021/j100077a019. URL: http://dx.doi.org/10.1021/j100077a019.

[23] A. Bouzid, E. M. Bourim, M. Gabbay, and G. Fantozzi. "PZT phase diagram determination by measurement of elastic moduli". In: *Journal of the European Ceramic Society* 25.13 (Aug. 2005), pp. 3213–3221. ISSN: 0955-2219. DOI: 10.1016/j.jeurceramsoc.2004.07.018. URL: http://www.sciencedirect.com/science/article/pii/S0955221904003103.

[24] O. M. Braun, A. R. Bishop, and J. Röder. "Hysteresis in the Underdamped Driven Frenkel-Kontorova Model". In: *Phys. Rev. Lett.* 79.19 (Nov. 1997), pp. 3692–3695. DOI: 10.1103/PhysRevLett.79.3692. URL: http://link.aps.org/doi/10.1103/PhysRevLett.79.3692 (visited on 04/02/2015).

[25] O. M. Braun, Yu. S. Kivshar, and I. I. Zelenskaya. "Kinks in the Frenkel-Kontorova model with long-range interparticle interactions". In: *Physical Review B* 41.10 (Apr. 1990), pp. 7118–7138. DOI: 10.1103/PhysRevB.41.7118. URL: http://link.aps.org/doi/10.1103/PhysRevB.41.7118 (visited on 04/08/2014).

[26] Oleg M. Braun and Yuri Kivshar. *The Frenkel-Kontorova Model: Concepts, Methods, and Applications*. en. Google-Books-ID: fWvrCAAAQBAJ. Springer Science & Business Media, Mar. 2013. ISBN: 978-3-662-10331-9.

[27] Oleg M. Braun and Yuri S. Kivshar. "Nonlinear dynamics of the Frenkel-Kontorova model". In: *Physics Reports* 306.1–2 (Dec. 1998), pp. 1–108. ISSN: 0370-1573. DOI: 10.1016/S0370-1573(98)00029-5. URL: http://www.sciencedirect.com/science/article/pii/S0370157398000295.

[28] B. Budiansky. "Theory of Buckling and Post-buckling Behavior in Elastic Structures". In: *Advances of Applied Mechanics*. Elsevier, 1974, pp. 1–65. URL: http://www.sciencedirect.com/science/article/pii/S0065215608700309.

[29] F. Carpi, G. Frediani, S. Turco, and D. De Rossi. "Bioinspired tunable lens with muscle-like electroactive elastomers". In: *Adv. Funct. Mater.* 21 (2011), pp. 4152–4158.

[30] B. G. Chen, N. Upadhyaya, and V. Vitelli. "Nonlinear conduction via solitons in a topological mechanical insulator". In: *PNAS* 111.36 (2014), pp. 13004–13009.

[31] Andrej Cherkaev, Elena Cherkaev, and Leonid Slepyan. "Transition waves in bistable structures. I. Delocalization of damage". In: *Journal of the Mechanics and Physics of Solids* 53.2 (Feb. 2005), pp. 383–405. ISSN: 0022-5096. DOI: 10.1016/j.jmps.2004.08.002. URL: http://www.sciencedirect.com/science/article/pii/S0022509604001395.

[32] M. Cirillo, R. D. Parmentier, and B. Savo. "Mechanical analog studies of a perturbed sine-Gordon equation". In: *Physica D: Nonlinear Phenomena* 3.3 (Aug. 1981), pp. 565–576. ISSN: 0167-2789. DOI: 10.1016/0167-2789(81)90040-3. URL: http://www.sciencedirect.com/science/article/pii/0167278981900403.

[33] J. C. Comte, P. Marquié, and M. Remoissenet. "Dissipative lattice model with exact traveling discrete kink-soliton solutions: Discrete breather generation and reaction diffusion regime". In: *Phys. Rev. E* 60.6 (Dec. 1999), pp. 7484–7489. DOI: 10.1103/PhysRevE.60.7484. URL: http://link.aps.org/doi/10.1103/PhysRevE.60.7484 (visited on 04/01/2015).

[34] Jun Cui, Yong S. Chu, Olugbenga O. Famodu, Yasubumi Furuya, Jae Hattrick-Simpers, Richard D. James, Alfred Ludwig, Sigurd Thienhaus, Manfred Wuttig, Zhiyong Zhang, and Ichiro Takeuchi. "Combinatorial search of thermoelastic shape-memory alloys with extremely small hysteresis width". en. In: *Nature Materials* 5.4 (Apr. 2006), pp. 286–290. ISSN: 1476-1122. DOI: 10.1038/nmat1593. URL: http://www.nature.com/nmat/journal/v5/n4/full/nmat1593.html.

[35] Thierry Dauxois and Michel Peyrard. *Physics of solitons*. Cambridge University Press, 2006.

[36] T. Devaux, V. Tournat, O. Richoux, and V. Pagneux. “Asymmetric acoustic propagation of wave packets via the self-demodulation effect”. In: *Phys. Rev. Lett.* 115 (2015), p. 234301.

[37] Yiqun Ding, Zhengyou Liu, Chunyin Qiu, and Jing Shi. “Metamaterial with Simultaneously Negative Bulk Modulus and Mass Density”. In: *Phys. Rev. Lett.* 99.9 (Aug. 2007), p. 093904. DOI: 10.1103/PhysRevLett.99.093904. URL: http://link.aps.org/doi/10.1103/PhysRevLett.99.093904.

[38] S. Dusuel, P. Michaux, and M. Remoissenet. “From kinks to compactonlike kinks”. In: *Physical Review E* 57.2 (Feb. 1998), pp. 2320–2326. DOI: 10.1103/PhysRevE.57.2320. URL: http://link.aps.org/doi/10.1103/PhysRevE.57.2320.

[39] D. T. Eddington, R. H. Liu, J. S. Moore, and D. J. Beebe. “An organic self-regulating microfluidic system”. In: *Lab Chip* 1.2 (2001), pp. 96–99.

[40] Thomas Erneux and Grégoire Nicolis. “Propagating waves in discrete bistable reaction-diffusion systems”. In: *Physica D: Nonlinear Phenomena* 67.1 (Aug. 1993), pp. 237–244. ISSN: 0167-2789. DOI: 10.1016/0167-2789(93)90208-I. URL: http://www.sciencedirect.com/science/article/pii/016727899390208I.

[41] J. D. Eshelby. “The Determination of the Elastic Field of an Ellipsoidal Inclusion, and Related Problems”. en. In: *Proceedings of the Royal Society of London A: Mathematical, Physical and Engineering Sciences* 241.1226 (Aug. 1957), pp. 376–396. ISSN: 1364-5021, 1471-2946. DOI: 10.1098/rspa.1957.0133. URL: http://rspa.royalsocietypublishing.org/content/241/1226/376.

[42] N. Fang, D. Xi, J. Xu, M. Ambati, W. Srituravanich, C. Sun, and X. Zhang. “Ultrasonic metamaterials with negative modulus”. In: *Nature Materials* 5.6 (2006), pp. 452–456. ISSN: 1476-1122. DOI: 10.1038/nmat1644.

[43] A. Fargette, S. Neukirch, and A. Antkowiak. “Elastocapillary Snapping: Capillarity Induces Snap-Through Instabilities in Small Elastic Beams”. In: *Phys. Rev. Lett.* 112 (2014), p. 137802.

[44] B. F. Feeny and A. R. Diaz. “Twinkling Phenomena in Snap-Through Oscillators”. In: *Journal of Vibration and Acoustics* 132.6 (2010).

[45] Richard FitzHugh. “Impulses and Physiological States in Theoretical Models of Nerve Membrane”. In: *Biophysical Journal* 1.6 (July 1961), pp. 445–466. ISSN: 0006-3495. URL: http://www.ncbi.nlm.nih.gov/pmc/articles/PMC1366333/.

[46] B. Florijn, C. Coulais, and M. van Hecke. “Programmable mechanical metamaterials”. In: *Phys. Rev. Lett.* 113 (2014), p. 175503.

[47] Y. Forterre, J. M. Skotheim, J. Dumais, and L. Mahadevan. "How the Venus flytrap snaps". In: *Nature* 433.7024 (2005), pp. 421–425.

[48] F. Fraternali, T. Blesgen, A. Amendola, and C. Daraio. "Multiscale mass-spring models of carbon nanotube foams". In: *Journal of the Mechanics and Physics of Solids* 59.1 (Jan. 2011), pp. 89–102. ISSN: 0022-5096. DOI: 10.1016/j.jmps.2010.09.004. URL: http://www.sciencedirect.com/science/article/pii/S0022509610001808.

[49] F. Fraternali, G. Carpentieri, A. Amendola, R. E. Skelton, and V. F. Nesterenko. "Multiscale tunability of solitary wave dynamics in tensegrity metamaterials". In: *Applied Physics Letters* 105 (2014), p. 201903.

[50] F. Fraternali, L. Senatore, and C. Daraio. "Solitary waves on tensegrity lattices". In: *Journal of the Mechanics and Physics of Solids* 60.6 (June 2012), pp. 1137–1144. ISSN: 00225096. DOI: 10.1016/j.jmps.2012.02.007. URL: http://linkinghub.elsevier.com/retrieve/pii/S0022509612000385.

[51] YI Frenkel and T Kontorova. "The model of dislocation in solid body". In: *Zh. Eksp. Teor. Fiz.* 8 (1938).

[52] Gero Friesecke and Jonathan A. D. Wattis. "Existence theorem for solitary waves on lattices". In: *Communications in Mathematical Physics* 161.2 (1994), pp. 391–418. URL: http://projecteuclid.org/euclid.cmp/1104269908.

[53] Pradipta Giri, Kamal Choudhary, Arghya Dey, Arindam Biswas, Aniruddha Ghosal, and A. K. Bandyopadhyay. "Discrete energy levels of bright solitons in lithium niobate ferroelectrics". In: *Phys. Rev. B* 86.18 (Nov. 2012), p. 184101. DOI: 10.1103/PhysRevB.86.184101. URL: http://link.aps.org/doi/10.1103/PhysRevB.86.184101 (visited on 04/01/2015).

[54] D. J. Hartl and D. C. Lagoudas. "Aerospace applications of shape memory alloys". en. In: *Proceedings of the Institution of Mechanical Engineers, Part G: Journal of Aerospace Engineering* 221.4 (Apr. 2007), pp. 535–552. ISSN: 0954-4100, 2041-3025. DOI: 10.1243/09544100JAERO211. URL: http://pig.sagepub.com/content/221/4/535.

[55] A. L. Hodgkin and A. F. Huxley. "Propagation of Electrical Signals Along Giant Nerve Fibres". In: *Proceedings of the Royal Society of London. Series B, Biological Sciences* 140.899 (1952), pp. 177–183. ISSN: 0080-4649. URL: http://www.jstor.org/stable/82686.

[56] Bambi Hu, Bin Lin, and Jicong Shi. "Generalized Frenkel-Kontorova models". In: *Physica A: Statistical Mechanics and its Applications* 205.1–3 (Apr. 1994), pp. 420–442. ISSN: 0378-4371. DOI: 10.1016/0378-4371(94)90521-5. URL: http://www.sciencedirect.com/science/article/pii/0378437194905215 (visited on 04/09/2015).

[57] Gérard Iooss and Klaus Kirchgässner. “Travelling Waves in a Chain of Coupled Nonlinear Oscillators”. In: *Communications in Mathematical Physics* 211.2 (2000), pp. 439–464. ISSN: 0010-3616. DOI: 10.1007/s002200050821. URL: http://dx.doi.org/10.1007/s002200050821.

[58] Yoshihiro Ishibashi and Yutaka Takagi. “Note on ferroelectric domain switching”. In: *Journal of the Physical Society of Japan* 31.2 (1971), pp. 506–510.

[59] Yuji Ishimori and Toyonori Munakata. “Kink Dynamics in the Discrete Sine-Gordon System A Perturbational Approach”. In: *Journal of the Physical Society of Japan* 51.10 (Oct. 1982), pp. 3367–3374. ISSN: 0031-9015. DOI: 10.1143/JPSJ.51.3367. URL: http://journals.jps.jp/doi/abs/10.1143/JPSJ.51.3367.

[60] W. G. Jenks, S. S. H. Sadeghi, and J. P. Wikswo Jr. “SQUIDs for nondestructive evaluation”. en. In: *Journal of Physics D: Applied Physics* 30.3 (1997), p. 293. ISSN: 0022-3727. DOI: 10.1088/0022-3727/30/3/002. URL: http://stacks.iop.org/0022-3727/30/i=3/a=002.

[61] Shu Jia, Wenjie Wan, and Jason W. Fleischer. “Dispersive Shock Waves in Nonlinear Arrays”. In: *Physical Review Letters* 99.22 (Nov. 2007), p. 223901. DOI: 10.1103/PhysRevLett.99.223901. URL: http://link.aps.org/doi/10.1103/PhysRevLett.99.223901.

[62] B. D. Josephson. “Possible new effects in superconductive tunnelling”. In: *Physics Letters* 1.7 (July 1962), pp. 251–253. ISSN: 0031-9163. DOI: 10.1016/0031-9163(62)91369-0. URL: http://www.sciencedirect.com/science/article/pii/0031916362913690.

[63] Yoshiki Kashimori, Takeshi Kikuchi, and Kichisuke Nishimoto. “The solitonic mechanism for proton transport in a hydrogen bonded chain”. In: *J. Chem. Phys.* 77.4 (Aug. 1982), pp. 1904–1907. ISSN: 0021-9606, 1089-7690. DOI: 10.1063/1.444043. URL: http://scitation.aip.org/content/aip/journal/jcp/77/4/10.1063/1.444043 (visited on 04/02/2015).

[64] J. Keener. “Propagation and Its Failure in Coupled Systems of Discrete Excitable Cells”. In: *SIAM Journal on Applied Mathematics* 47.3 (June 1987), pp. 556–572. ISSN: 0036-1399. DOI: 10.1137/0147038. URL: http://epubs.siam.org/doi/abs/10.1137/0147038.

[65] James P. Keener and James Sneyd. *Mathematical Physiology*. Vol. 1. Springer, 1998.

[66] Devvrath Khatri, Duc Ngo, and Chiara Daraio. “Highly nonlinear solitary waves in chains of cylindrical particles”. English. In: *Granular Matter* 14.1 (2012), pp. 63–69. ISSN: 1434-5021. DOI: 10.1007/s10035-011-0297-9. URL: http://dx.doi.org/10.1007/s10035-011-0297-9.

[67] Oskar Klein. “Quantum theory and five dimensional theory of relativity”. In: *Z. Phys.* 37 (1926), pp. 895–906.

[68] Andrei Nikolaevich Kolmogorov. “On the statistical theory of the crystallization of metals”. In: *Bull. Acad. Sci. USSR, Math. Ser* 1 (1937), pp. 355–359.

[69] O. Kresse and L. Truskinovsky. “Lattice friction for crystalline defects: from dislocations to cracks”. In: *Journal of the Mechanics and Physics of Solids* 52.11 (Nov. 2004), pp. 2521–2543. ISSN: 0022-5096. DOI: 10.1016/j.jmps.2004.04.011. URL: http://www.sciencedirect.com/science/article/pii/S0022509604000997.

[70] Ramya Krishnan, S. Shirota, Y. Tanaka, and N. Nishiguchi. “High-efficient acoustic wave rectifier”. In: *Solid State Communications* 144.5–6 (2007), pp. 194–197. ISSN: 0038-1098. DOI: http://dx.doi.org/10.1016/j.ssc.2007.08.036. URL: http://www.sciencedirect.com/science/article/pii/S0038109807006308.

[71] I. K. Kuder, A. F. Arrieta, and P. Ermanni. “Design Space Exploration of Embeddable Variable Stiffness Bi-Stable Composites”. In: *Composite Structures* 122 (2015), pp. 445–455. DOI: 10.1016/j.compstruct.2014.11.061.

[72] M. S. Kushwaha, P. Halevi, L. Dobrzynski, and B. Djafari-Rouhani. “Acoustic band structure of periodic elastic composites”. In: *Phys. Rev. Lett.* 71.13 (1993), pp. 2022–2025. DOI: 10.1103/PhysRevLett.71.2022. URL: http://link.aps.org/doi/10.1103/PhysRevLett.71.2022.

[73] Jean Pierre Laplante and Thomas Erneux. “Propagation failure in arrays of coupled bistable chemical reactors”. In: *The Journal of Physical Chemistry* 96.12 (June 1992), pp. 4931–4934. ISSN: 0022-3654. DOI: 10.1021/j100191a038. URL: http://dx.doi.org/10.1021/j100191a038.

[74] Thanh-Nam Le, Jean-Marc Battini, and Mohammed Hjiaj. “Efficient formulation for dynamics of corotational 2D beams”. In: *Computational Mechanics* 48.2 (2011), pp. 153–161.

[75] J. A. Lewis. “Direct Ink Writing of 3D Functional Materials”. In: *Adv. Funct. Mater.* 16 (2006), pp. 2193–2204.

[76] F. Li, P. Anzel, J. Yang, P. G. Kevrekidis, and C. Daraio. “Granular acoustic switches and logic elements”. In: *Nature Communications* 5 (2014), p. 5311.

[77] Xue-Feng Li, Xu Ni, Liang Feng, Ming-Hui Lu, Cheng He, and Yan-Feng Chen. “Tunable unidirectional sound propagation through a sonic-crystal-based acoustic diode”. In: *Physical Review Letters* 106.8 (2011), p. 084301.

[78] Y. L. Li, S. Choudhury, Z. K. Liu, and L. Q. Chen. "Effect of external mechanical constraints on the phase diagram of epitaxial PbZr1-xTixO3 thin films-thermodynamic calculations and phase-field simulations". In: *Applied Physics Letters* 83.8 (Aug. 2003), pp. 1608–1610. ISSN: 0003-6951, 1077-3118. DOI: 10.1063/1.1600824. URL: http://scitation.aip.org/content/aip/journal/apl/83/8/10.1063/1.1600824.

[79] Y. L. Li, S. Y. Hu, Z. K. Liu, and L. Q. Chen. "Effect of substrate constraint on the stability and evolution of ferroelectric domain structures in thin films". In: *Acta Materialia* 50.2 (Jan. 2002), pp. 395–411. ISSN: 1359-6454. DOI: 10.1016/S1359-6454(01)00360-3. URL: http://www.sciencedirect.com/science/article/pii/S1359645401003603.

[80] Y. L. Li, S. Y. Hu, Z. K. Liu, and L. Q. Chen. "Phase-field model of domain structures in ferroelectric thin films". In: *Applied Physics Letters* 78.24 (June 2001), pp. 3878–3880. ISSN: 0003-6951, 1077-3118. DOI: 10.1063/1.1377855. URL: http://scitation.aip.org/content/aip/journal/apl/78/24/10.1063/1.1377855.

[81] B Liang, XS Guo, J Tu, D Zhang, and JC Cheng. "An acoustic rectifier". In: *Nature Materials* 9.12 (2010), pp. 989–992.

[82] Shi Liu, Ilya Grinberg, and Andrew M. Rappe. "Intrinsic ferroelectric switching from first principles". en. In: *Nature* 534.7607 (June 2016), pp. 360–363. ISSN: 0028-0836. DOI: 10.1038/nature18286. URL: http://www.nature.com/nature/journal/v534/n7607/abs/nature18286.html.

[83] Z. Liu, X. Zhang, Y. Mao, Y.Y. Zhu, Z. Yang, C.T. Chan, and P. Sheng. "Locally Resonant Sonic Materials". In: *Science* 289.5485 (2000), pp. 1734–1736. DOI: 10.1126/science.289.5485.1734. URL: http://www.sciencemag.org/content/289/5485/1734.abstract.

[84] Zhengyou Liu, C. T. Chan, and Ping Sheng. "Analytic model of phononic crystals with local resonances". In: *Phys. Rev. B* 71.1 (Jan. 2005), p. 014103. DOI: 10.1103/PhysRevB.71.014103. URL: http://link.aps.org/doi/10.1103/PhysRevB.71.014103.

[85] Nicholas K. Lowman and Mark A. Hoefer. "Dispersive Shock Waves in Viscously Deformable Media". In: *Journal of Fluid Mechanics* 718 (Mar. 2013). arXiv:1401.7864 [nlin], pp. 524–557. ISSN: 0022-1120, 1469-7645. DOI: 10.1017/jfm.2012.628. URL: http://arxiv.org/abs/1401.7864.

[86] L. G. Machado and M. A. Savi. "Medical applications of shape memory alloys". In: *Brazilian Journal of Medical and Biological Research* 36.6 (June 2003), pp. 683–691. ISSN: 0100-879X. DOI: 10.1590/S0100-879X2003000600001. URL: http://www.scielo.br/scielo.php?

script=sci_abstract&pid=S0100-879X2003000600001&lng=en&nrm=iso&tlng=pt.

[87] Yuriy Makhlin, Gerd Schön, and Alexander Shnirman. "Quantum-state engineering with Josephson-junction devices". In: *Reviews of Modern Physics* 73.2 (May 2001), pp. 357–400. DOI: 10.1103/RevModPhys.73.357. URL: http://link.aps.org/doi/10.1103/RevModPhys.73.357.

[88] A. D. Marchese, C. D. Onal, and D. Rus. "Autonomous soft robotic fish capable of escape maneuvers using fluidic elastomer actuators". In: *Soft Robotics* 1.1 (2014), pp. 75–87.

[89] Qingping Meng, Myung-Geun Han, Jing Tao, Guangyong Xu, David O Welch, and Yimei Zhu. "Velocity of domain-wall motion during polarization reversal in ferroelectric thin films: Beyond Merz's Law". In: *Physical Review B* 91.5 (2015), p. 054104.

[90] W. J. Merz. "Switching Time in BaTiO3: Dependence on Crystal Thickness". In: *Journal of Applied Physics* 27.8 (1956), pp. 938–943. URL: http://dx.doi.org/10.1063/1.1722518.

[91] Walter J. Merz. "Domain Formation and Domain Wall Motions in Ferroelectric BaTiO3 Single Crystals". In: *Physical Review* 95.3 (1954). PR, pp. 690–698. URL: http://link.aps.org/doi/10.1103/PhysRev.95.690.

[92] D.A.B. Miller. "On perfect cloaking". In: *Optics Express* 14.25 (2006), pp. 12457–12466. ISSN: 1094-4087. DOI: 10.1364/OE.14.012457. URL: http://www.opticsinfobase.org/oe/abstract.cfm?uri=oe-14-25-12457.

[93] R. C. Miller and A. Savage. "Motion of 180o Domain Walls in Metal Electroded Barium Titanate Crystals as a Function of Electric Field and Sample Thickness". In: *Journal of Applied Physics* 31.4 (1960), pp. 662–669. DOI: http://dx.doi.org/10.1063/1.1735663. URL: http://link.aip.org/link/?JAP/31/662/1.

[94] G.W. Milton, M. Briane, and J.R. Willis. "On cloaking for elasticity and physical equations with a transformation invariant form". In: *New Journal of Physics* 8.10 (2006), p. 248. URL: http://stacks.iop.org/1367-2630/8/i=10/a=248.

[95] M. Molerón, A. Leonard, and C. Daraio. "Solitary waves in a chain of repelling magnets". In: *Journal of Applied Physics* 115 (2014), p. 184901. DOI: http://dx.doi.org/10.1063/1.4872252.

[96] F. R. N. Nabarro. "Dislocations in a simple cubic lattice". en. In: *Proceedings of the Physical Society* 59.2 (1947), p. 256. ISSN: 0959-5309. DOI: 10.1088/0959-5309/59/2/309. URL: http://stacks.iop.org/0959-5309/59/i=2/a=309.

[97] Neel Nadkarni, Andres F. Arrieta, Christopher Chong, Dennis M. Kochmann, and Chiara Daraio. "Unidirectional Transition Waves in Bistable Lattices". In: *Physical Review Letters* 116.24 (June 2016), p. 244501. DOI: 10.1103/PhysRevLett.116.244501. URL: http://link.aps.org/doi/10.1103/PhysRevLett.116.244501.

[98] Neel Nadkarni, Chiara Daraio, Rohan Abeyaratne, and Dennis M. Kochmann. "Universal energy transport law for dissipative and diffusive phase transitions". In: *Physical Review B* 93.10 (Mar. 2016), p. 104109. DOI: 10.1103/PhysRevB.93.104109. URL: http://link.aps.org/doi/10.1103/PhysRevB.93.104109.

[99] Neel Nadkarni, Chiara Daraio, and Dennis M. Kochmann. "Dynamics of periodic mechanical structures containing bistable elastic elements: From elastic to solitary wave propagation". In: *Physical Review E* 90.2 (Aug. 2014), p. 023204. DOI: 10.1103/PhysRevE.90.023204. URL: http://link.aps.org/doi/10.1103/PhysRevE.90.023204.

[100] J. Nagumo, S. Arimoto, and S. Yoshizawa. "An Active Pulse Transmission Line Simulating Nerve Axon". In: *Proceedings of the IRE* 50.10 (Oct. 1962), pp. 2061–2070. ISSN: 0096-8390. DOI: 10.1109/JRPROC.1962.288235.

[101] K. Nakajima, H. Hauser, T. Li, and R. Pfeifer. "Information processing via physical soft body". In: *Scientific Reports* 5 (2015), p. 10487.

[102] Koji Nakajima, Tsutomu Yamashita, and Yutaka Onodera. "Mechanical analogue of active Josephson transmission line". In: *Journal of Applied Physics* 45.7 (July 1974), pp. 3141–3145. ISSN: 0021-8979, 1089-7550. DOI: 10.1063/1.1663738. URL: http://scitation.aip.org/content/aip/journal/jap/45/7/10.1063/1.1663738.

[103] Ali Hasan Nayfeh. *Introduction to Perturbation Techniques*. Wiley Classics Edition, 1993.

[104] V. Nesterenko. *Dynamics of heterogeneous materials*. Springer, 2001.

[105] V. F. Nesterenko. "Propagation of nonlinear compression pulses in granular media". In: *Appl. Mech. Tech. Phys.* 24.24 (1984), pp. 733–743. DOI: 10.1007/BF00905892.

[106] Nathan M Newmark. "A method of computation for structural dynamics". In: *Journal of the Engineering Mechanics Division* 85.3 (1959), pp. 67–94.

[107] R. W. Ogden. *Nonlinear Elastic Deformations*. Dover, UK: Dover Publications, 1998.

[108] M. Oudich, M. Badreddine Assouar, and Z. Hou. "Propagation of acoustic waves and waveguiding in a two-dimensional locally resonant phononic crystal plate". In: *Applied Physics Letters* 97.19 (2010), p. 193503. DOI: 10.1063/1.3513218. URL: http://link.aip.org/link/?APL/97/193503/1.

[109] J. T. B. Overvelde, T. Kloek, J. J. A. Dhaen, and K. Bertoldi. “Amplifying the response of soft actuators by harnessing snap-through instabilities”. In: *PNAS* 112.35 (2015), pp. 10863–10868.

[110] A. Pandey, D. E. Moulton, D. Vella, and D. P. Holmes. “Dynamics of snapping beams and jumping poppers”. In: *EPL-Europhys. Lett.* 105.2 (2014), p. 24001.

[111] W.J. Parnell. “Effective wave propagation in a prestressed nonlinear elastic composite bar”. In: *IMA Journal of Applied Mathematics* 72.2 (2007), pp. 223–244. URL: http://eprints.ma.man.ac.uk/795/.

[112] R. Peierls. “The size of a dislocation”. en. In: *Proceedings of the Physical Society* 52.1 (1940), p. 34. ISSN: 0959-5309. DOI: 10.1088/0959-5309/52/1/305. URL: http://stacks.iop.org/0959-5309/52/i=1/a=305.

[113] M. Peyrard and A. R. Bishop. “Statistical mechanics of a nonlinear model for DNA denaturation”. In: *Phys. Rev. Lett.* 62.23 (June 1989), pp. 2755–2758. DOI: 10.1103/PhysRevLett.62.2755. URL: http://link.aps.org/doi/10.1103/PhysRevLett.62.2755.

[114] Michel Peyrard and Martin D. Kruskal. “Kink dynamics in the highly discrete sine-Gordon system”. In: *Physica D: Nonlinear Phenomena* 14.1 (Dec. 1984), pp. 88–102. ISSN: 0167-2789. DOI: 10.1016/0167-2789(84)90006-X. URL: http://www.sciencedirect.com/science/article/pii/016727898490006X.

[115] Sebastian Poliak and Elior Peles. “The local differentiation of myelinated axons at nodes of Ranvier”. en. In: *Nature Reviews Neuroscience* 4.12 (Dec. 2003), pp. 968–980. ISSN: 1471-003X. DOI: 10.1038/nrn1253. URL: http://www.nature.com/nrn/journal/v4/n12/abs/nrn1253.html.

[116] A. D. Polyanin and V. F. Zaitsev. *Handbook of Nonlinear Partial Differential Equations*. Chapman and Hall CRC, 2004.

[117] Bogdan-Ioan Popa and Steven A. Cummer. “Non-reciprocal and highly nonlinear active acoustic metamaterials”. In: *Nature Communications* 5 (Feb. 2014). ISSN: 2041-1723. DOI: 10.1038/ncomms4398. URL: http://www.nature.com/doifinder/10.1038/ncomms4398.

[118] Bogdan-Ioan Popa, Lucian Zigoneanu, and Steven A. Cummer. “Tunable active acoustic metamaterials”. In: *Phys. Rev. B* 88.2 (July 2013), p. 024303. DOI: 10.1103/PhysRevB.88.024303. URL: http://link.aps.org/doi/10.1103/PhysRevB.88.024303.

[119] Jordan R. Raney, Neel Nadkarni, Chiara Daraio, Dennis M. Kochmann, Jennifer A. Lewis, and Katia Bertoldi. “Stable propagation of mechanical signals in soft media using stored elastic energy”. en. In: *Proceedings of the National Academy of Sciences* 113.35 (Aug. 2016), pp. 9722–9727. ISSN: 0027-8424, 1091-6490. DOI: 10.1073/pnas.1604838113. URL: http://www.pnas.org/content/113/35/9722.

[120] M. Remoissenet. "Low-amplitude breather and envelope solitons in quasi-one-dimensional physical models". In: *Physical Review B* 33.4 (Feb. 1986), pp. 2386–2392. DOI: 10.1103/PhysRevB.33.2386. URL: http://link.aps.org/doi/10.1103/PhysRevB.33.2386.

[121] M. Remoissenet and M. Peyrard. "Soliton dynamics in new models with parametrized periodic double-well and asymmetric substrate potentials". In: *Physical Review B* 29.6 (Mar. 1984), pp. 3153–3166. DOI: 10.1103/PhysRevB.29.3153. URL: http://link.aps.org/doi/10.1103/PhysRevB.29.3153 (visited on 03/29/2014).

[122] Michel Remoissenet. *Waves called solitons: concepts and experiments*. Springer Verlag, 1999.

[123] D. Restrepo, N. D. Mankame, and P. D. Zavattieri. "Phase transforming cellular materials". In: *Extreme Mechanics Letters* 4 (2015), pp. 52–60.

[124] H. H. Rotermund, S. Jakubith, A. von Oertzen, and G. Ertl. "Solitons in a surface reaction". In: *Physical Review Letters* 66.23 (June 1991), pp. 3083–3086. DOI: 10.1103/PhysRevLett.66.3083. URL: http://link.aps.org/doi/10.1103/PhysRevLett.66.3083.

[125] M. Ruzzene and F. Scarpa. "Directional and band-gap behavior of periodic auxetic lattices". In: *physica status solidi (b)* 242 (2005), pp. 665–680. DOI: 10.1002/pssb.200460385. URL: http://dx.doi.org/10.1002/pssb.200460385.

[126] Massimo Ruzzene, Fabrizio Scarpa, and Francesco Soranna. "Wave beaming effects in two-dimensional cellular structures". In: *Smart Materials and Structures* 12.3 (2003), p. 363.

[127] Mario Salerno. "A mechanical analog for the double sine-Gordon equation". In: *Physica D: Nonlinear Phenomena* 17.2 (Oct. 1985), pp. 227–234. ISSN: 0167-2789. DOI: 10.1016/0167-2789(85)90007-7. URL: http://www.sciencedirect.com/science/article/pii/0167278985900077.

[128] J. Sánchez-Dehesa, D. Torrent, and L.-W. Cai. "Acoustic transparency in two-dimensional sonic crystals". In: *New Journal of Physics* 11.1 (2009), p. 013039. URL: http://stacks.iop.org/1367-2630/11/i=1/a=013039.

[129] Michael Scalora, Jonathan P. Dowling, Charles M. Bowden, and Mark J. Bloemer. "The photonic band edge optical diode". In: *Journal of Applied Physics* 76.4 (1994), pp. 2023–2026. DOI: http://dx.doi.org/10.1063/1.358512. URL: http://scitation.aip.org/content/aip/journal/jap/76/4/10.1063/1.358512.

[130] A. C. Scott. "A Nonlinear Klein-Gordon Equation". In: *American Journal of Physics* 37.1 (Jan. 1969), pp. 52–61. ISSN: 0002-9505, 1943-2909. DOI: 10.1119/1.1975404. URL: http://scitation.aip.org/content/aapt/journal/ajp/37/1/10.1119/1.1975404.

[131] Alwyn C. Scott. "The electrophysics of a nerve fiber". In: *Reviews of Modern Physics* 47.2 (Apr. 1975), pp. 487–533. DOI: 10.1103/RevModPhys.47.487. URL: http://link.aps.org/doi/10.1103/RevModPhys.47.487.

[132] James F. Scott. *Ferroelectric Memories*. Vol. 3. Springer Science & Business Media, 2013.

[133] S. Shan, S. H. Kang, J. R. Raney, P. Wang, L. Fang, F. Candido, J. A. Lewis, and K. Bertoldi. "Multistable Architected Materials for Trapping Elastic Strain Energy". In: *Adv. Mater.* 27.29 (2015), pp. 4296–4301.

[134] P. Sheng, X.X. Zhang, Z. Liu, and C.T. Chan. "Locally resonant sonic materials". In: *Physica B* 338.1-4 (2003), pp. 201–205. DOI: 10.1016/S0921-4526(03)00487-3. URL: http://www.sciencedirect.com/science/article/pii/S0921452603004873.

[135] R. F. Shepherd, F. Ilievski, W. Choi, S. A. Morin, A. A. Stokes, A. D. Mazzeo, X. Chen, M. Wang, and G. M. Whitesides. "Multigait soft robot". In: *PNAS* 108.51 (2011), pp. 20400–20403.

[136] Young-Han Shin, Ilya Grinberg, I.-Wei Chen, and Andrew M. Rappe. "Nucleation and growth mechanism of ferroelectric domain-wall motion". en. In: *Nature* 449.7164 (Oct. 2007), pp. 881–884. ISSN: 0028-0836. DOI: 10.1038/nature06165. URL: http://www.nature.com/nature/journal/v449/n7164/abs/nature06165.html.

[137] M. Sigalas and E. N. Economou. "Band structure of elastic waves in two dimensional systems". In: *Solid State Communications* 86.3 (1993), pp. 141–143. DOI: 10.1016/0038-1098(93)90888-T. URL: http://www.sciencedirect.com/science/article/pii/003810989390888T.

[138] L. I. Slepyan and L. V. Troyankina. "Fracture wave in a chain structure". en. In: *Journal of Applied Mechanics and Technical Physics* 25.6 (Nov. 1984), pp. 921–927. ISSN: 0021-8944, 1573-8620. DOI: 10.1007/BF00911671. URL: http://link.springer.com/article/10.1007/BF00911671.

[139] Leonid Slepyan, Andrej Cherkaev, and Elena Cherkaev. "Transition waves in bistable structures. II. Analytical solution: wave speed and energy dissipation". In: *Journal of the Mechanics and Physics of Solids* 53.2 (Feb. 2005), pp. 407–436. ISSN: 0022-5096. DOI: 10.1016/j.jmps.2004.08.001. URL: http://www.sciencedirect.com/science/article/pii/S0022509604001383.

[140] J. B. Sokoloff. "Ionic order and defect conductivity in the one-dimensional superionic conductor hollandite". In: *Phys. Rev. B* 17.12 (June 1978), pp. 4843–4849. DOI: 10.1103/PhysRevB.17.4843. URL: http://link.aps.org/doi/10.1103/PhysRevB.17.4843 (visited on 04/02/2015).

[141] G. Song, N. Ma, and H. -N. Li. "Applications of shape memory alloys in civil structures". In: *Engineering Structures* 28.9 (July 2006), pp. 1266–1274. ISSN: 0141-0296. DOI: 10.1016/j.engstruct.2005.12.010. URL: http://www.sciencedirect.com/science/article/pii/S0141029606000344.

[142] Alessandro Spadoni and Chiara Daraio. "Generation and control of sound bullets with a nonlinear acoustic lens." In: *Proceedings of the National Academy of Sciences of the United States of America* 107.16 (Apr. 2010), pp. 7230–7234. ISSN: 1091-6490. DOI: 10.1073/pnas.1001514107. URL: http://www.pubmedcentral.nih.gov/articlerender.fcgi?artid=2867709&tool=pmcentrez&rendertype=abstract.

[143] W. C. Stewart. "Current-Voltage Characteristics of Josephson Junctions". In: *Applied Physics Letters* 12.8 (Apr. 1968), pp. 277–280. ISSN: 0003-6951, 1077-3118. DOI: 10.1063/1.1651991. URL: http://scitation.aip.org/content/aip/journal/apl/12/8/10.1063/1.1651991 (visited on 04/08/2015).

[144] Y. Su and C. M. Landis. "Continuum thermodynamics of ferroelectric domain evolution: Theory, finite element implementation, and application to domain wall pinning". In: *Journal of the Mechanics and Physics of Solids* 55.2 (2007), pp. 280–305. ISSN: 0022-5096. DOI: http://dx.doi.org/10.1016/j.jmps.2006.07.006. URL: http://www.sciencedirect.com/science/article/pii/S0022509606001256.

[145] Yu. Suchorski, J. Beben, E. W. James, J. W. Evans, and R. Imbihl. "Fluctuation-Induced Transitions in a Bistable Surface Reaction: Catalytic CO Oxidation on a Pt Field Emitter Tip". In: *Physical Review Letters* 82.9 (Mar. 1999), pp. 1907–1910. DOI: 10.1103/PhysRevLett.82.1907. URL: http://link.aps.org/doi/10.1103/PhysRevLett.82.1907.

[146] Ramathasan Thevamaran, Fernando Fraternali, and Chiara Daraio. "Multi-scale Mass-Spring Model for High-Rate Compression of Vertically Aligned Carbon Nanotube Foams". In: *Journal of Applied Mechanics* 81.12 (Oct. 2014), pp. 121006–121006. ISSN: 0021-8936. DOI: 10.1115/1.4028785. URL: http://dx.doi.org/10.1115/1.4028785.

[147] S. P. Timoshenko. "Buckling of flat curved bars and slightly curved plates". In: *J. Appl. Mech.* 2 (1935), pp. 17–C20.

[148] Michael Tinkham. *Introduction to superconductivity*. Second. Courier Corporation, 1996.

[149] M. T. Tolley, R. F. Shepherd, B. Mosadegh, K. C. Galloway, M. Wehner, M. Karpelson, R. J. Wood, and G. M. Whitesides. "A resilient, untethered soft robot". In: *Soft Robotics* 1.3 (2014), pp. 213–223.

[150] L. Truskinovsky and A. Vainchtein. "Kinetics of Martensitic Phase Transitions: Lattice model". In: *SIAM Journal on Applied Mathematics* 66.2 (Jan. 2005), pp. 533–553. ISSN: 0036-1399. DOI: 10.1137/040616942. URL: http://epubs.siam.org/doi/abs/10.1137/040616942.

[151] T. Tybell, P. Paruch, T. Giamarchi, and J.-M. Triscone. "Domain Wall Creep in Epitaxial Ferroelectric PbZr0.2Ti0.8O3 Thin Films". In: *Physical Review Letters* 89.9 (Aug. 2002), p. 097601. DOI: 10.1103/PhysRevLett.89.097601. URL: http://link.aps.org/doi/10.1103/PhysRevLett.89.097601.

[152] A. V. Ustinov, M. Cirillo, and B. A. Malomed. "Fluxon dynamics in one-dimensional Josephson-junction arrays". In: *Physical Review B* 47.13 (Apr. 1993), pp. 8357–8360. DOI: 10.1103/PhysRevB.47.8357. URL: http://link.aps.org/doi/10.1103/PhysRevB.47.8357.

[153] Alexey V. Ustinov, Boris A. Malomed, and Shigeki Sakai. "Bunched fluxon states in one-dimensional Josephson-junction arrays". In: *Physical Review B* 57.18 (May 1998), pp. 11691–11697. DOI: 10.1103/PhysRevB.57.11691. URL: http://link.aps.org/doi/10.1103/PhysRevB.57.11691.

[154] Anna Vainchtein. "Effect of nonlinearity on the steady motion of a twinning dislocation". In: *Physica D: Nonlinear Phenomena* 239.13 (July 2010), pp. 1170–1179. ISSN: 0167-2789. DOI: 10.1016/j.physd.2010.03.007. URL: http://www.sciencedirect.com/science/article/pii/S0167278910001016 (visited on 03/27/2014).

[155] B. Voelker, P. Marton, C. Elsässer, and M. Kamlah. "Multiscale modeling for ferroelectric materials: a transition from the atomic level to phase-field modeling". en. In: *Continuum Mechanics and Thermodynamics* 23.5 (Sept. 2011), pp. 435–451. ISSN: 0935-1175, 1432-0959. DOI: 10.1007/s00161-011-0188-7. URL: http://link.springer.com/article/10.1007/s00161-011-0188-7.

[156] Marian Vopsaroiu, John Blackburn, Markys G. Cain, and Paul M. Weaver. "Thermally activated switching kinetics in second-order phase transition ferroelectrics". In: *Phys. Rev. B* 82 (2 July 2010), p. 024109. DOI: 10.1103/PhysRevB.82.024109. URL: http://link.aps.org/doi/10.1103/PhysRevB.82.024109.

[157] M. Wehner, M. T. Tolley, Y. Mengüc, Y.-L. Park, A. Mozeika, Y. Ding, C. Onal, R. F. Shepherd, G. M. Whitesides, and R. J. Wood. "Pneumatic energy sources for autonomous and wearable soft robotics". In: *Soft Robotics* 2 (2014), pp. 263–274.

[158] Michael Weiss and Franz-Josef Elmer. "Dry friction in the Frenkel-Kontorova-Tomlinson model: dynamical properties". en. In: *Zeitschrift für Physik B Condensed Matter* 104.1 (Feb. 2014), pp. 55–69. ISSN: 0722-3277, 1431-

584X. DOI: 10.1007/s002570050420. URL: http://link.springer.com/article/10.1007/s002570050420.

[159] Michael Weiss and Franz-Josef Elmer. "Dry friction in the Frenkel-Kontorova-Tomlinson model: Static properties". In: *Physical Review B* 53.11 (Mar. 1996), pp. 7539–7549. DOI: 10.1103/PhysRevB.53.7539. URL: http://link.aps.org/doi/10.1103/PhysRevB.53.7539.

[160] C. S. Wojnar and D. M. Kochmann. "A negative-stiffness phase in elastic composites can produce stable extreme effective dynamic but not static stiffness". In: *Philosophical Magazine* 94.6 (2014), pp. 532–555. DOI: 10.1080/14786435.2013.857795. URL: http://www.tandfonline.com/doi/abs/10.1080/14786435.2013.857795.

[161] Charles Stanley Wojnar. "Exploring the Kinetics of Domain Switching in Ferroelectrics for Structural Applications". PhD thesis. California Institute of Technology, 2015.

[162] Liang-Yu Wu, Tzeh-Yi Chiang, Chia-Nien Tsai, Mei-Ling Wu, and Lien-Wen Chen. "Design of an acoustic bending waveguide with acoustic metamaterials via transformation acoustics". English. In: *Applied Physics A* 109.3 (2012), pp. 523–533. ISSN: 0947-8396. DOI: 10.1007/s00339-012-7296-5. URL: http://dx.doi.org/10.1007/s00339-012-7296-5.

[163] J. Xin. "Front Propagation in Heterogeneous Media". In: *SIAM Review* 42.2 (Jan. 2000), pp. 161–230. ISSN: 0036-1445. DOI: 10.1137/S0036144599364296. URL: http://epubs.siam.org/doi/abs/10.1137/S0036144599364296.

[164] H. Xu, P. G. Kevrekidis, and A. Stefanov. "Traveling waves and their tails in locally resonant granular systems". In: *Journal of Physics A: Mathematical and Theoretical* 48.19 (2015), p. 195204. URL: http://stacks.iop.org/1751-8121/48/i=19/a=195204.

[165] D. Yang, B. Mosadegh, A. Ainla, B. Lee, F. Khashai, Z. Suo, K. Bertoldi, and G. M. Whitesides. "Buckling of elastomeric beams enables actuation of soft machines". In: *Adv. Mater.* DOI: 10.1002/adma.201503188 (2015).

[166] Z. Yang, Jun Mei, Min Yang, N. H. Chan, and Ping Sheng. "Membrane-Type Acoustic Metamaterial with Negative Dynamic Mass". In: *Phys. Rev. Lett.* 101.20 (Nov. 2008), p. 204301. DOI: 10.1103/PhysRevLett.101.204301. URL: http://link.aps.org/doi/10.1103/PhysRevLett.101.204301.

[167] D. Yu, Y. Liu, H. Zhao, G. Wang, and J. Qiu. "Flexural vibration band gaps in Euler-Bernoulli beams with locally resonant structures with two degrees of freedom". In: *Phys. Rev. B* 73.6 (2006), p. 064301. DOI: 10.1103/PhysRevB.73.064301. URL: http://link.aps.org/doi/10.1103/PhysRevB.73.064301.

[168] V. E. Zakharov. “Stability of periodic waves of finite amplitude on the surface of a deep fluid”. In: *Journal of Applied Mechanics and Technical Physics* 9 (1968), pp. 190–194.

[169] V. E. Zakharov and A.B. Shabat. “Exact theory of two-dimensional self-focusing and one-dimensional self-modulation of waves in nonlinear media”. In: *Soviet Physics JETP* 37 (1974), pp. 823–828.

[170] W. Zhang and K. Bhattacharya. “A computational model of ferroelectric domains. Part I: model formulation and domain switching”. In: *Acta Materialia* 53.1 (2005). Read 04/25/13, pp. 185–198. ISSN: 1359-6454. DOI: http://dx.doi.org/10.1016/j.actamat.2004.09.016. URL: http://www.sciencedirect.com/science/article/pii/S1359645404005580.

[171] W. Zhang and K. Bhattacharya. “A computational model of ferroelectric domains. Part II: grain boundaries and defect pinning”. In: *Acta Materialia* 53.1 (2005), pp. 199–209. ISSN: 1359-6454. DOI: http://dx.doi.org/10.1016/j.actamat.2004.09.015. URL: http://www.sciencedirect.com/science/article/pii/S1359645404005579.

[172] Yuguang Zhang, Jihong Wen, Honggang Zhao, Dianlong Yu, Li Cai, and Xisen Wen. “Sound insulation property of membrane-type acoustic metamaterials carrying different masses at adjacent cells”. In: *Journal of Applied Physics* 114.6 (2013), DOI: http://dx.doi.org/10.1063/1.4818435. URL: http://scitation.aip.org/content/aip/journal/jap/114/6/10.1063/1.4818435.

[173] Nian-Shun Zhao, Hui Zhou, Qi Guo, Wei Hu, Xiang-Bo Yang, Sheng Lan, and Xu-Sheng Lin. “Design of highly efficient optical diodes based on the dynamics of nonlinear photonic crystal molecules”. In: *JOSA B* 23.11 (2006), pp. 2434–2440.

[174] Xuefeng Zhu, Xinye Zou, Bin Liang, and Jianchun Cheng. “One-way mode transmission in one-dimensional phononic crystal plates”. In: *Journal of Applied Physics* 108.12 (2010), p. 124909.

[175] Yaroslav Zolotaryuk and Mario Salerno. “Discrete soliton ratchets driven by biharmonic fields”. In: *Physical Review E* 73.6 (June 2006), p. 066621. DOI: 10.1103/PhysRevE.73.066621. URL: http://link.aps.org/doi/10.1103/PhysRevE.73.066621 (visited on 04/01/2015).